Platinum surface instabilities and their impact in electrochemistry
Valls Mascaro, F.

Citation
Valls Mascaro, F. (2024, September 5). *Platinum surface instabilities and their impact in electrochemistry*. Retrieved from https://hdl.handle.net/1887/4054933

Platinum Surface Instabilities and their Impact in Electrochemistry

Francesc Valls Mascaró

Platinum Surface Instabilities and their Impact in Electrochemistry

Proefschrift

ter verkrijging van

de graad van doctor aan de Universiteit Leiden,

op gezag van rector magnificus prof.dr.ir. H. Bijl,

volgens besluit van het college voor promoties

te verdedigen op donderdag 5 september 2024

klokke 16:00 uur

door

Francesc Valls Mascaró

geboren te Pollensa, Spain

in 1995

Promotores:

Prof. dr. M. T. M. Koper

Dr. M. J. Rost

Promotiecommissie:

Prof. dr. M. Ubbink

Prof. dr. I. M. N. Groot

Prof. dr. J. M. van Ruitenbeek

Prof. dr. O. M. Magnussen (Kiel University, Germany)

Prof. dr. ir. H. J. W. Zandvliet (University of Twente, The Netherlands)

Science is a way of thinking

much more than it is a body of knowledge

- Carl Sagan

Table of Contents

Table of Contents

1 Introduction

1.1 Electrochemistry for the Future

The global issue of climate change presents an imminent threat to the ecological balance of our planet. The rising concentrations of greenhouse gases, such as CO_2 and N_2O, contribute to increasing temperatures and extreme weather events. In addition, the worldwide growth in population urges to meet energy requirements that increase daily, thereby reinforcing the emissions of greenhouse gases. Addressing this energy and environmental crisis necessitates to transition from fossil fuels to renewable energy sources, such as solar power and wind, that can be converted into electricity. The latter can then be either used *in-situ* or stored in alternative energy forms like chemical bonds. This can be achieved by using electrochemical devices such as batteries [1], electrolysers, and fuel cells [2, 3].

Figure 1.1 represents a scheme of the operational principle of a hydrogen fuel cell, which converts the chemical energy of hydrogen into electricity [4]. In summary, hydrogen gas is supplied at the anode, where it oxidizes resulting in protons and electrons, known as the Hydrogen Oxidation Reaction (HOR) (equation 1.1). These electrons then travel through the external circuit before reaching the other electrode, the cathode. There, they combine with protons and molecular oxygen to produce water and heat, referred to as the Oxygen Reduction Reaction (ORR) (equation 1.2). The Proton Exchange Membrane (PEM) separating the two compartments acts as a selective barrier that allows only protons to pass through, while it blocks electrons and other species in solution.

$$H_2 \rightarrow 2\,H^+ + 2\,e^- \qquad\qquad E_{anode} = 0\,V \qquad (1.1)$$

$$\tfrac{1}{2}\,O_2 + 2\,H^+ + 2\,e^- \rightarrow H_2O \qquad\qquad E_{cathode} = 1.23\,V \qquad (1.2)$$

$$H_2 + \tfrac{1}{2}\,O_2 \rightarrow H_2O \qquad\qquad E_{cell} = 1.23\,V \qquad (1.3)$$

The overall reaction 1.3 is a combination of the half-cell reactions taking place at the anode and at the cathode, and it delivers ideally a potential of 1.23 V, if one would neglect any power loss during the process. The power reduction stems from three main sources: the ohmic (IR) drop due to material and electrolyte resistances, the limitations on the supply

and transport of the reactants and, especially, the large activation barrier for the ORR [4]. This activation barrier can be reduced by using a *catalyst* as the cathode material, which provides a more optimal reaction pathway, in which the reaction intermediates bind the reaction sites neither too weakly (thereby allowing fast adsorption) nor too strongly (hence they can leave the sites promptly post-reaction) [5]. This not only boosts the reaction rate but it is also crucial to ensure that only water, and not another species such as hydrogen peroxide, is the final product [6].
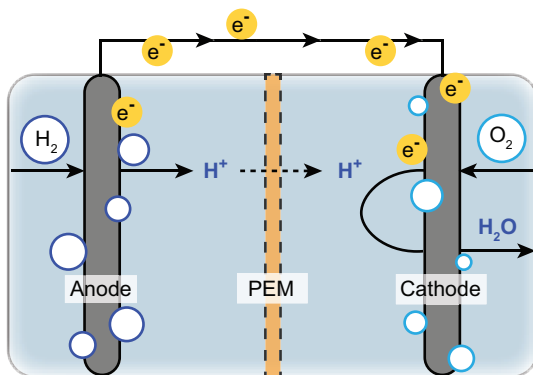
Figure 1.1: Hydrogen Fuel Cell. Scheme of a Proton Exchange Membane (PEM) Fuel Cell that reacts H_2 with O_2 to generate electricity, with water as a product. The PEM membrane allows the transport of H^+ through, which is transported from the anode to the cathode, where it reacts.

For both the ORR and the HOR, the best catalysts known are platinum-based. However, even with these catalysts the ORR at the cathode still suffers a significant energy loss. Moreover, platinum is scarce and expensive, which hinders the industrial scalability of fuel cells using this material [3, 4]. Furthermore, it is well-known that platinum degrades and dissolves in the electrolyte upon fuel cell operation, which leads to a decrease of its electrochemical activity and ultimately to the need to replace the catalyst [7]. Therefore, electrochemical research is needed in order to optimize the platinum catalyst design, to increase its activity and stability by forming alloys, or to simply find a more affordable, abundant material that satisfies the catalytic requirements.

In addition to hydrogen fuel cells and batteries, electrochemistry could also provide an answer to convert many of the most polluting chemical processes into cleaner alternatives. The steam methane reforming process, in which hot steam and natural gas react to produce hydrogen, but also the polluting carbon monoxide and carbon dioxide as side-products, could be replaced by water splitting via electrolysis. This method generates hydrogen and oxygen gases through the reverse reaction conducted in fuel cells [3, 6]. The production of ammonia, traditionally carried out in the Haber-Bosch process by reacting nitrogen and hydrogen gases at high temperature and pressure, could also be achieved by the electrocatalytic reduction of nitrate [8]. Finally, carbon dioxide can be captured from the air and electrochemically converted into valuable fuels and organic chemicals such as methane, ethylene, and formic acid [9]. However, at present the industrial scalability of

these *green* processes is severely limited by unresolved technological challenges, as well as the economical barrier of not offering a cheaper alternative. Finding optimal electrocatalysts and reaction conditions is key for their success.

1.2 Design of an Electrochemical Experiment

An electrochemical experiment can have different goals, from testing a particular electrocatalyst (or reaction condition) for the conversion into the desired product(s), to identifying each of the individual reaction steps, especially the one that hinders the overall reaction (the so-called rate-determining step) [10]. In any case, a typical experimental design aims to isolate the electrochemical process under study (e.g. the ORR on platinum in acidic media), which takes place at the working electrode. A second electrode, a counter, closes the electrical circuit by providing a current of equal magnitude but opposite sign to that at the working electrode. Therefore, an oxidation reaction at the working electrode will always occur simultaneously with a reduction reaction at the counter electrode, and vice-versa, although the process taking place at the counter electrode is generally disregarded. Finally, a reference electrode is used that reliably measures the electrochemical potential in the electrolyte, against which the electrochemical potential at the working electrode can be compared. This three-electrode configuration in an electrochemical (glass) cell filled with electrolyte is usually sufficient for conducting standard measurements.

The most common electrochemical experiment is cyclic voltammetry, in which the potential of the working electrode is swept through the potential range of interest before the direction of scan is reversed, simultaneously recording the current response. This technique provides a large amount of valuable information, as each of the peaks observed in the current versus potential curve represents a different electrochemical fingerprint. Therefore, by carefully studying the position, magnitude, and shape of the peaks it is possible to extract thermodynamic and kinetic parameters from the underlying electrochemical processes, which facilitates their identification [11].

1.3 Structure-Activity Relationships

In heterogeneous electrocatalysis, which is the focus of this thesis, the reactions occur at the electrode-electrolyte interface. Therefore, it is not surprising that the nanoscale surface structure of the electrode plays a crucial role on the catalytic activity [12]. This effect has been extensively studied for electrochemical reactions such as the ORR and the HOR on platinum, due to their importance in hydrogen fuel cells [13, 14]. The origin of the surface sensitivity relies on the dependence of the reaction rate with the binding strength of the reaction intermediates [15], which is closely related to the nature and geometry of the adsorption site. Thereby, surface sites with distinct coordination, such as terrace and step sites, present unalike catalytic activity [16]. Designing better catalysts requires therefore a deep comprehension of the relationship between the surface structure and the surface reactivity.

The best way to expand this knowledge is by studying the electrochemistry of single-crystalline samples. As the surface structure of these electrodes is *a priori* well-defined, a systematic study allows identification of the most active sites. Figure 1.2 shows examples of platinum surfaces with different structures, which are obtained by cutting (and polishing) a single-crystalline platinum sample with a certain orientation respect to its unit cell (the smallest repetitive unit). In order to classify the surfaces according to their orientation, we refer to a notation called Miller indexes, represented in between brackets [17]. Fig. 1.2a shows the (111) surface of a metal with a face-centered cubic (fcc) crystalline structure. This surface has the most densely packed atomic arrangement, consisting of an hexagonal unit cell, and displays adsorption sites with different coordination than the ones at the (110) surface (Fig. 1.2b) or at the (100) surface (Fig. 1.2c), which have rectangular and square unit cells, respectively. The (111), (100), and (110) surfaces are considered basal planes, as cutting the single crystal in any other orientation results in vicinal surfaces with atomic steps.

As illustrated in Fig. 1.2, the steps on vicinal surfaces can exhibit different microfacets. For example, on Pt(111)-vicinal surfaces the steps can form either a rectangular (110) microfacet or a square (100) microfacet with the lower step edge atoms, while the steps on (100)-vicinals can only exhibit a rectangular (110) geometry. Evidently, each of these atomic arrangements presents a unique local potential energy landscape and thus different electrochemistry.

Single crystal surfaces have been traditionally used in (vacuum) surface science to study material properties, surface processes, and adsorption of gas molecules, among others [18]. Typically, their preparation for surface studies involves several weeks of ion bombardment followed by electron-beam annealing in vacuum. However, the development of the flame-annealing procedure provided a relatively easier alternative to prepare single-crystalline surfaces, which boosted significantly their application for fundamental electrochemistry [19, 20]. This facilitated to study relationships between surface structure and electrocatalytic activity, which enabled the identification of the most active surface sites for the ORR on platinum, among many other reactions [16]. Moreover, single crystal electrodes are also used to investigate the effect of the electrolyte or electrochemical reactions on metal surfaces, which is key to understand the fundamentals of catalyst degradation [21]. *In-situ* and *operando* characterization techniques, such as Electrochemical Scanning Tunneling Microscopy, are ideal for this purpose.

1.4 Electrochemical Scanning Tunneling Microscopy

Inspired by the development of the topografiner by Young et al. [22], in 1981 Binning and Rohrer invented the Scanning Tunneling Microscope (STM), which represented a major leap forward in the atomic-level characterization of metal surfaces [23]. This instrument operates by scanning a sharp metal tip at a very close distance (i.e. typically less than 1 nm) from the (conducting) sample surface. When a bias voltage is applied between tip and sample in tunneling range, electrons flow between them, leading to a current that is then measured [24]. Subsequently, the tunneling current, I_t, is amplified by the pre-amp (see
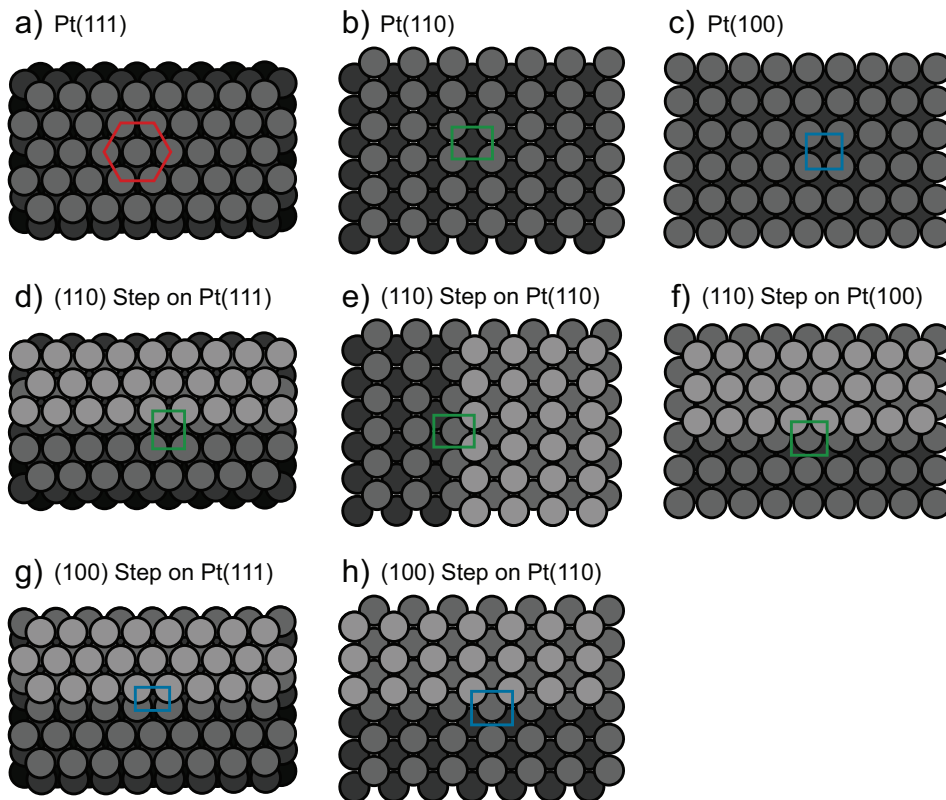
Figure 1.2: Model Single-Crystalline Platinum Electrodes. **(a-c)** Basal surface planes: Pt(111), Pt(110), and Pt(100), respectively. **(d-f)** (110) steps (also referred to as (111) steps in electrochemistry literature) on each of the basal planes, as indicated. **(g)** and **(h)** (100) steps on Pt(111) and Pt(110), respectively. The unit cells on each basal plane and the microfacets formed at the steps are indicated.

Fig. 1.3a) and turned into voltage, which exponential dependence with the tip-sample distance is linearized by a logarithmic amplifier [25]. The output signal is then compared with the set tunneling current that is applied as a target voltage. The difference between them is processed by the feedback electronics, which allows to modify the signal by applying a proportional gain (independent of the signal frequency), an integral gain (frequency dependent), and a low-pass filter, which attenuates the signals with a frequency higher than the cutoff value. Finally, the output is amplified by the high-voltage amplifiers and delivered to the Z electrode of the piezo tube, which moves the tip in height correspondingly.

A typical STM has two possible operational modes. By maintaining a constant I_t, the tip follows the surface contour, producing detailed topographic images. Alternatively, one can keep the tip height constant, and then the topographic images are generated from the fluctuating I_t. This operational mode often results in images that show atomic resolution and it

also allows for scans at higher speed, although it is severely limited to (almost) atomically-flat surfaces. Moreover, it requires a calibration in Z as well as knowing the value of the work function. In order to circumvent these issues our microscope can operate, in addition, in hybrid mode, in which the tip height is measured together with its error signal, therefore combining the benefits from both constant-current and constant-height modes [25, 26].

Only a few years after its invention, STM technology was applied also to obtain atomic-scale topographic images of surfaces submerged in liquids, giving birth to the Electrochemical Scanning Tunneling Microscope (EC-STM) [27]. The major difference between both techniques resides in the fact that, while in an STM the voltage difference is directly applied between tip and sample, in an EC-STM both tip and sample have their own voltage with respect to a reference electrode potential that is measured in the electrolyte. This was achieved by incorporating a bipotentiostat [28–30], which allowed for the direct characterization of the surface under electrochemical conditions. However this leads to experimental complications, as it requires the stability of three feedback loops working with each other: one for the tip potential, another for the sample potential, and a last one for the tunneling current I_t.

The work function (Φ) for a metal submerged in electrolyte is remarkably lower than the one in vacuum. I_t depends exponentially on both Φ as well as on the distance between the tip and the sample ($d_{tip-sample}$) [25]:

$$I_t \propto exp(-1.025\sqrt{\Phi}\,d_{tip-sample}) \tag{1.4}$$

Therefore, in electrolyte one needs to tunnel with an I_t orders of magnitude larger in order to scan the tip at the same $d_{tip-sample}$ than in vacuum. Scanning further away from the surface results in a decrease of the imaging resolution, as the geometric integral of the tunneling current coming from the surface picks up more undesired current from the sides than directly from under the tip. Moreover, in electrochemical conditions both tip and sample are exposed to any reactions that might take place, which lead to faradaic currents at the tip that directly couple to the tunneling current, thereby interfering with the imaging. In order to minimize this problem, the STM tip is usually coated with an insulator material leaving only the very apex exposed.

Figure 1.3b shows a schematic representation of the EC-STM cell together with the bipotentiostat. The sample is placed on a sample holder that allows tuning of its height with nm accuracy. A quartz cell is placed above the sample, with a viton o-ring in between that seals the connection. Clamps on the sides of the cell hold it together, preventing any leakage. The cell is filled with the working electrolyte, which flows in and out with the help of a peristatic pump. The counter electrode is a Pt wire, while the reference electrode is a Reversible Hydrogen Electrode connected to the counter and working electrodes, tip and sample, via thin tubing. The STM-tip is made from a PtIr wire and is isolated with a polymer coating. Finally, all electrodes are connected to a bipotentiostat, which sets the desired tip and sample voltages with respect to the reference electrode potential.
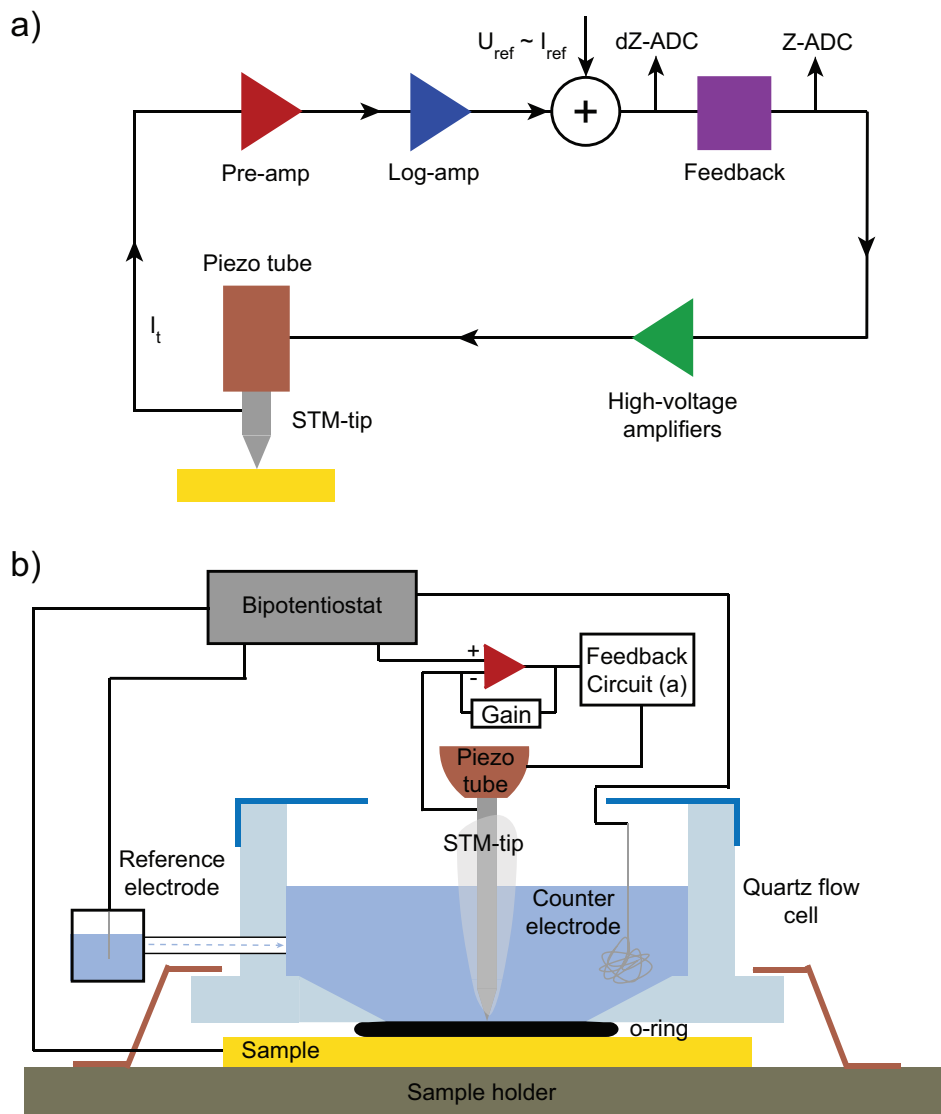
Figure 1.3: Feedback circuit of an STM and scheme of an EC-STM cell. (a) The tunneling current measured at the tip (I_t) is amplified and turned into a voltage by the pre-amp before its exponential dependence with the tip-sample distance is linearized by the log-amp. The signal is then compared with a chosen current setpoint, which is applied as a target voltage. The resulting error (dZ) is treated by the feedback and amplified by the high-voltage amplifiers, before it is delivered to the Z electrodes of the piezo tube, which move the tip in height correspondingly. The tip height (Z) is given by the output voltage of the feedback. Both the Z and dZ signals are converted into digital via their respective ADCs (Analog to Digital Converters) before being processed by the computer. **(b)** The sample and cell are clamped down onto a sample holder. The electrolyte flows in and out of the cell with the help of a peristatic pump. I_t is measured at the tip, while the electrochemical current is measured at the sample. The sample and tip voltages are measured with respect to the reference electrode potential by using a bipotentiostat.

1.5   Outline of this Thesis

This thesis presents a study on the (in)stability of single-crystalline platinum electrodes in an electrochemical environment and how the surface structure changes affect the electrochemistry. *In-situ* characterization with EC-STM allows us to establish structure-activity relationships that are crucial for the development of more efficient catalysts. In Chapter 2, we study the nucleation and growth of adatom islands on a Pt(111) surface upon oxidation-reduction cycling. With the help from Density Functional Theory, we provide both a thermodynamic and a kinetic explanation to why the islands form during the reduction of the surface oxide, although the adatoms are formed during the oxidation. Moreover, we provide EC-STM evidence that the adatom islands have a dendritic shape as well as an explanation of the growth instability that leads to the formation of the dendritic branches.

In Chapter 3 we show with EC-STM that stepped platinum surfaces with high step density undergo step bunching, which is an instability that results in terraces wider than the nominal value and steps with multiple atomic-layers height. This new insight challenges the common assumption in electrochemistry that all stepped surfaces present a regular array of monoatomic-height steps. Knowing this, we prove quantitatively that this structural effect is responsible for many anomalous step density-dependent trends reported in the literature, such as the ones linking the step density to the ORR activity and the potential of zero total charge.

In Chapter 4 we expand the existing knowledge regarding the electrochemical adsorption of hydrogen and oxygen on stepped platinum surfaces. Our quantitative results show that, on all surfaces studied, the voltammetric peak related to hydrogen desorption from the steps involves more than the simple desorption of one hydrogen atom per unit step length. On the other hand, at high electrode potentials, the adsorption of oxygen leads to the formation of PtO_2 along the steps. Finally, we link this chapter to the previous one by showing that less hydrogen and less oxygen adsorb at step bunches compared to single steps.

References

[1] B. Dunn, H. Kamath, and J. Tarascon, *Science*, **334**, 928 (2011).

[2] I. Staffell, D. Scamman, A. Velazquez Abad, P. Balcombe, P. E. Dodds, P. Ekins, N. Shah, and K. R. Ward, *Energy Environ. Sci.*, **12**, 463 (2019).

[3] Y. Wang, Y. Pang, H. Xu, A. Martinez, and K. S. Chen, *Energy Environ. Sci.*, **15**, 2288 (2022).

[4] M. K. Debe, *Nature*, **486**, 43 (2012).

[5] P. Sabatier, *La Catalyse en Chimie Organique*, 2nd ed., C. Béranger, Paris (1920).

[6] Y. Jiao, Y. Zheng, M. Jaroniec, and S. Zhang Qiao, *Chem. Soc. Rev.*, **44**, 2060 (2015).

[7] S. Cherevko, G. P. Keeley, S. Geiger, A. R. Zeradjanin, N. Hodnik, N. Kulyk, and K. J. J. Mayrhofer, *ChemElectroChem*, **2**, 1471 (2015).

[8] P. H. van Langevelde, I. Katsounaros, and M. T. M. Koper, *Joule*, **5**, 290 (2021).

[9] S. Nitopi, E. Bertheussen, S. B. Scott, X. Liu, A. K. Engstfeld, S. Horch, B. Seger, I. E. L. Stephens, K. Chan, C. Hahn, J. K. Nørskov, T. F. Jaramillo, and I. Chorkendorff, *Chem. Rev.*, **119**, 7610 (2019).

[10] D. Pletcher, *A First Course in Electrode Processes*, 2nd ed., Real Society of Chemistry, Cambridge (2009).

[11] A. J. Bard and L. R. Faulkner, *Electrochemical Methods: Fundamentals and Applications*, 2nd ed., Wiley, New York (2001).

[12] M. T. M. Koper, *Nanoscale*, **3**, 2054 (2011).

[13] P. N. Ross, *J. Electrochem. Soc.*, **126**, 78 (1979).

[14] N. M. Marković, S. T. Sarraf, H. A. Gasteiger, and P. N. Ross, *J. Chem. Soc. Faraday Trans.*, **92**, 3719 (1996).

[15] R. Parsons, *Trans. Faraday Soc.*, **54**, 1053 (1958).

[16] F. Calle-Vallejo, *Adv. Sci.*, **10**, 2207644 (2023).

[17] H. Ibach, *Physics of Surfaces and Interfaces*, Springer, Amsterdam (2006).

[18] T. Michely and J. Krug, *Islands, Mounds and Atoms*, Springer, Amsterdam (2004).

[19] J. Clavilier, R. Faure, G. Guinet, and R. Durand, *J. Electroanal. Chem.*, **107**, 205 (1980).

[20] V. Climent, J. M. Feliu, *J. Solid. State Electrochem.*, **15**, 1297 (2011).

[21] L. Jacobse, Y. F. Huang, M. T. M. Koper, and M. J. Rost, *Nat. Mater.*, **17**, 277 (2018).

[22] R. Young, J. Ward, F. Scire, *Rev. Sci. Instrum.*, **43**, 999 (1972).

[23] G. Binning, H. Rohrer, C. H. Gerber, and E. Weibel, *Phys. Rev. Lett.*, **49**, 57 (1982).

[24] C. J. Chen, *Introduction to Scanning Tunneling Microscopy*, 2nd ed., Oxford University Press, New York (2008).

[25] M. J. Rost, in *Encyclopedia of Interfacial Chemistry*, 1st ed., K. Wandelt, p.180, Elsevier, Amsterdam (2018).

[26] M. J. Rost, L. Crama, P. Schakel, E. van Tol, G. B. E. M. van Velzen-Williams, C. F. Overgauw, H. ter Horst, H. Dekker, B. Okhuijsen, M. Seynen, A. Vijftigschild, P. Han, A. J. Katan, K. Schoots, R. Schumm, and W. van Loo, *Rev. Sci. Instrum.*, **76**, 053710 (2005).

[27] R. Sonnenfeld and P. K. Hansma, *Science*, **232**, 211 (1986).

[28] D. T. Napp, D. C. Johnson, and S. Bruckenstein, *S. Anal. Chem.*, **39**, 481 (1967).

[29] P. Lustenberger, H. Rohrer, R. Christoph, and H. Siegenthaler, *J. Electroanal. Chem.*, **243**, 225 (1988).

[30] K. Itaya and E. Tomita, *Surf. Sci.*, **201**, L507 (1988).

2 Nucleation and Growth of Dendritic Islands during Platinum Oxidation-Reduction Cycling

Abstract

Platinum is the model catalyst in fuel cells because of its high activity towards oxygen reduction and hydrogen oxidation. However, its applicability is limited due to the degradation of the catalyst under operating conditions. This degradation process has been extensively studied by repeatedly oxidizing and reducing the electrode, which leads to the roughening of the surface due to the nucleation and growth of platinum nano-islands. Although the general picture of this surface roughening is well known, the atomic details concerning the nucleation and early growth of the islands are still under debate. In this work, we use Density Functional Theory (DFT) to calculate formation energies and diffusion barriers of an adatom, in both the unoxidized and the oxidized state, with the aim to provide further insight into the nucleation phenomena. Moreover, we analyze the shape of the nano-islands during the first stages of growth from images obtained experimentally with an Electrochemical Scanning Tunneling Microscope (EC-STM). Our results show not only that the islands form during the reduction of the surface, but also that they grow with a dendritic island shape, similarly to the platinum islands formed in vacuum by Molecular Beam Epitaxy (MBE).

2.1 Introduction

In heterogeneous catalysis, the surface structure of the catalyst plays a crucial role, as it determines not only the product selectivity and activity, but it also influences its stability [1–3]. This is especially the case for electrochemical reactions that are highly surface sensitive, such as the Oxygen Reduction Reaction (ORR) on platinum, which activity in acid is higher on stepped surfaces than on Pt(111) [4, 5].

Platinum is the model catalyst to be used not only in fuel cells, due to its high activity towards ORR and hydrogen oxidation [6–8], but also in electrolyzers to carry out the Hydrogen Evolution Reaction [9]. However, its economic feasibility is limited, as platinum is scarce, expensive and degrades upon fuel cell operation [10]. In order to obtain a better understanding of the reaction and the degradation mechanisms, it is crucial to observe the platinum surface structure under conditions as similar as possible to fuel cell operation. In the end, this would allow designing a better catalyst.

Cyclic oxidation-reduction of a platinum electrode is often used as a test for catalyst stability, as it simulates the switching *On* and *Off* of a fuel cell [11–13]. On Pt(111), this results in the formation of adatoms and vacancies, which leads to the nucleation and growth of platinum nano-islands (first only in 2D and later predominantly in height, thus 3D) [14–25]. The island growth involves the creation of step sites at the expense of terrace sites, which leads to a higher electrochemical signal for hydrogen adsorption/desorption [25, 26] and to a higher ORR activity, as specific sites near the step edges are more reactive towards the ORR [1]. The amount of step sites created depends not only on the number of islands present and their size, but also on their shape. The former two are correlated by the nucleation density: a larger number of nuclei requires the distribution of the adatoms among more islands that are, consequently, smaller. The nucleation density scales with F/M, where F is the flux of depositing atoms (i.e. in analogy to the deposition rate in Molecular Beam Epitxay (MBE)) and M is the adatom mobility. During growth, the 2D island shape differs from the standard equilibrium Wulff-shape [27–29]: while in thermodynamic equilibrium the 2D island shape is defined by the minimum of the total step free energy [30], the (kinetic) growth Wulff-shape depends on the anisotropic step kinetics (i.e. different orientations along the island perimeter experience different growth speeds) [31, 32]. Therefore, the 2D growth shape significantly depends on the atom diffusion along the island perimeter, and thus the steps, as well as around the according kink and corner sites [33–35]. In addition, it also depends on the rate, with which the adatoms reach the island edge [36, 37]. Enhancing the atom diffusion along the island perimeter, e.g. by raising the temperature, leads to more compact islands, while increasing the flux leads to islands with a larger number of branches, often called dendrites [30, 38, 39].

Previously, it was reported that the islands formed upon oxidation-reduction cycling of a Pt(111) electrode are hexagonal, and their steps and facets were identified and correlated with the different peaks in the hydrogen adsorption/desorption fingerprint (i.e. below 0.4 V in the Cyclic Voltammogram, see Fig. 2.1) [26]. However, it is known that Pt islands formed by MBE at low temperatures (≤ 300 K) [30, 37–39] grow dendritically. This dissimilarity is relevant, as the island shape effects the electrochemical activity: if the islands formed upon

oxidation-reduction would also grow dendritically, the earlier assignation of the peaks in the hydrogen adsorption/desorption region to the different steps and facets surely would need to be reconsidered. Moreover, it is still a puzzle when these islands exactly nucleate, as they could, until now, only be observed with a Scanning Tunneling Microscope (STM) when the surface was reduced, but not during the oxidation [24, 40], in which additional atoms are pushed out onto the surface [17, 41].

To address these issues, here we study the thermodynamics and kinetics of island nucleation by using formation and diffusion barriers calculated with Density Functional Theory (DFT). Our results show that nucleation takes place during the cathodic sweep, rather than during oxidation. Moreover, we analyze the island shape during early growth by measuring their perimeter and area, from which we finally determine the island compactness and a factor describing the additional step lengths. Contrary to what was suggested in [26], our observations provide evidence that the growth of the islands results in dendritic island shapes.

2.2 Experimental

Electrochemistry. The cyclic voltammograms were recorded in a three-electrode glass cell using a reversible hydrogen electrode (RHE) as the reference, a Pt wire (MaTeck, Germany) as a counter, and a Pt(111) crystal (with a purity of 99.999 % and polished < 0.1°, Surface Preparation Laboratory, The Netherlands) as the working electrode. Prior to the experiments, we left the glassware overnight in an acidified potassium permanganate solution and cleaned it afterwards with diluted piranha, before finally boiling it five times in ultrapure water (> 18.2 MΩ cm, Millipore Milli-Q). Similarly to sputtering and annealing in vacuum, we first etched the Pt(111) sample electrochemically (125 cycles at 50 Hz, ± 2 V versus Pt) in an acidified 2.5 M $CaCl_2$ solution, before flame annealing (3 min at around 1250 K) and cooling down in a 1:4 H_2/Ar mixture. We repeated this procedure three times before each experiment. To develop a denuded, (bulk) contamination free interface zone, we performed the last annealing step at slightly lower temperature (approximatelly 50 K less). The measurements were performed in an Ar-purged 0.1 M $HClO_4$ solution (Merck Suprapur) using a potentiostat from Bio-Logic (VSP-300).

Electrochemical Scanning Tunneling Microscopy. We recorded the STM images with a home-built Electrochemical Scanning Tunneling Microscope (EC-STM) described previously [42–45]. The reference electrode used was a RHE, the counter was a Pt coil, and the working electrode was the same Pt(111) crystal described above. The STM tips were electrochemically etched from a $Pt_{90}Ir_{10}$ wire and coated with electrophoretic paint (Clearclad HSR) as well as polyethylene to minimize the faradaic contributions in the tunneling current. The cleaning procedure of the glassware is described in Ref. [25]. To reduce the oxygen concentration in the electrolyte, we de-aerated it with N_2 before measuring for at least 3 hours. At the beginning of each experiment, we checked the surface quality and cleanliness first by cyclic voltammetry and then by scanning large surface areas with the STM.

DFT calculations. Using Density Functional Theory (DFT), we calculated the Gibbs free formation energy of a Pt-adatom and PtO_2-adatom (i.e. strictly speaking, a PtO_2-

admolecule) on Pt(111) as well as the Gibbs free adsorption energy of oxygen onto Pt step and kink sites. The DFT simulations were performed using the Vienna Ab-Initio Simulations Package [46–48]. A plane wave basis set was used with an energy cutoff of 450 eV and the ion core potentials were modelled using the projector augmented wave (PAW) approach. The PW91 exchange-correlation functional was used [49]. We modeled the surface as a four-layer slab, with the bottom two layers frozen at the experimentally measured lattice constant of Pt (3.92 Å [50]). The Pt(111) surface was modeled with 5x5 and 7x7 unit cells. We used the energy of an additional Pt atom attached directly to a kink site on Pt(632) as a reference for the formation energy determination of a PtO$_2$-adatom. The Pt(632) surface was modeled in a 1x1 unit cell. Monkhorst-Pack mesh k-space sampling grids were used [51]. A 3x3x1 mesh grid was used for both the 5x5 and 7x7 Pt(111) unit cells, and a 7x7x1 grid was used for the 1x1 Pt(632) surface. We optimized the geometry until the forces on each atom were less than 0.02 eV Å^{-1}, and included dipole correction in the surface normal direction [52].

To calculate the potential-dependent Gibbs free formation energy of a PtO$_2$-adatom on Pt(111), we modeled the reaction equations 2.3-2.5 in the Results section. We calculated the Gibbs free energy change for each reaction from $\Delta G = \sum G_{products} - \sum G_{reactants}$, where G stands for the Gibbs free energy of each species calculated at 300 K and 1 bar. For the adsorbed species we accounted only for vibrational energy and entropy terms, whereas for the gas phase species (hydrogen and water) we included all contributions to the free energy consisting of vibrational, rotational, and translational energy. The Gibbs free energies of adsorption and formation were calculated relative to aqueous water and protons using the computational hydrogen electrode method [7] and procedures described previously [53]. The Gibbs free energy of the gas phase water was evaluated at its experimentally measured vapor pressure at 300 K; under conditions where it is in equilibrium with liquid (aqueous) water.

We calculated the oxygen adsorption at step as well as kink sites on Pt(632) as a function of oxygen coverage: the structures evaluated were based on those found to be most stable by Fantauzzi et al [54].

We calculated the diffusion barrier for a Pt-adatom on Pt(111) using the climbing-image nudged elastic band method [55]. The transition state was identified when, for the highest energy image, the forces on each of the atoms and the tangent force were below 0.02 eV Å^{-1} and the tangent forces on the preceding images were opposite in sign to the those on the images following the transition state image. The transition state vibrational modes were also examined, and showed one imaginary frequency along the reaction path. Diffusion was examined from the most stable, fcc, adsorption site to the second most stable, hcp, site.

2.3   Electrochemical Measurements

Figure 2.1 shows in red the Cyclic Voltammogram (CV) of the pristine Pt(111) surface in a 0.1 M HClO$_4$ solution measured between 0.06 and 0.85 V, and in orange the first Oxidation-Reduction Cycle (ORC) measured up to 1.35 V. The region below 0.4 V, attributed to hy-

drogen adsorption/desorption, changes during the next 200 ORCs due to the creation of (111) and (100) steps (which more precisely should be formulated as <110>/{111} and <110>/{100}, that is, steps along a direction equivalent to [110], with either {111} or {100} microfacets) [26, 56–60]. The increase in the number of step sites with increasing cycle number also becomes evident from the potential window between 0.8 and 1.0 V, where step oxidation takes place, leading also there to an increase of the electrochemical current [61, 62].
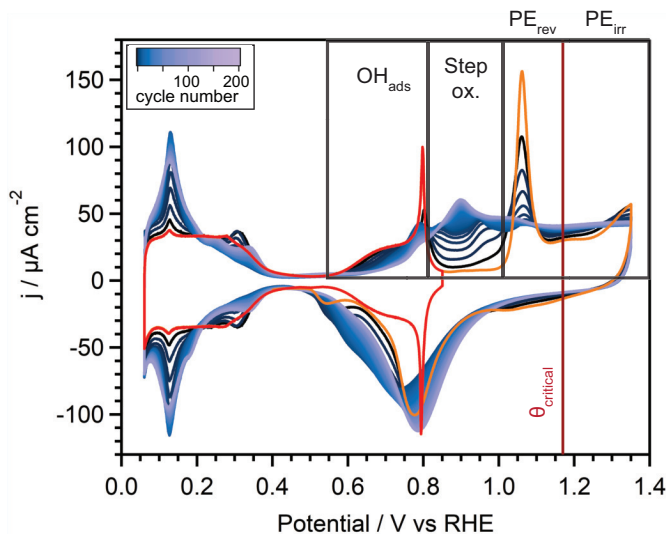
Figure 2.1: Oxidation-Reduction Cycles on Pt(111). The CV to only 0.85 V and the first ORC are shown in red and in orange, respectively, while the remaining ORCs are indicated according to the color scale. The OH adsorption, step oxidation, PE_{rev}, and PE_{irr} regions are indicated, as well as the voltage at the critical coverage. The scan rate is 50 mV s^{-1}.

Focusing now on the terraces, the first step towards (but still prior to) terrace oxidation is the adsorption of OH that takes place between 0.5 and 0.8 V [63, 64]. At higher potentials, the OH_{ad} is converted into O_{ad}, which subsequently interchanges position with the platinum surface atoms in the so-called reversible Place Exchange (PE_{rev}) [65]: concretely, at least 1, but most likely 2 oxygen atoms go subsurface underneath a Pt atom, which they lift vertically up to nearly one atomic distance in height [41, 66–72]. This process results in the pronounced peak at around 1.06 V [73, 74]. Its position shifts to higher potentials with faster scan rates, indicating that either the conversion of OH_{ad} to O_{ad}, or the place-exchange, or both are kinetically limited [41, 75–77].

The coverage of lifted PE_{rev} atoms rises with increasing electrode potential, leading to an increase of the surface stress [65]. If the upper (vertex) potential during the ORCs is held below 1.17 V [41] (or below 1.25 V, according to You et al. [78]), no structural changes take place upon reduction: all hovering PE_{rev} atoms fall back into their vacancies, and the original, flat Pt(111) surface is fully restored [41, 72, 77–79]. This changes completely if the

upper potential is increased beyond the critical value, which implies also that a critical coverage of PE_{rev} atoms is surpassed [65]. At this moment the surface stress becomes so large that, instead of creating new PE_{rev} atoms, the next atoms created by the PE mechanism are no longer hovering above their vacancies; instead they are displaced on top of the terrace, thus becoming real adatoms, which we call PE_{irr} atoms or PtO_2-adatoms as they do get oxidized [17, 41, 65]. Upon reduction, the surface is no longer restored during the cathodic sweep, as the adatoms formed during the PE_{irr} nucleate into islands before finding their way back to their original sites, i.e. before annihilating with their vacancies [80]. This is also favored by the Ehrlich-Schwoebel barrier [81, 82], which makes it more difficult for the adatoms to hop-down the descending step and fall into the vacancy, although it is known that the Ehrlich-Schwoebel barrier breaks down for small terraces [83] and for downhill transport mediated by kinks [84, 85]. This irreversible regime is responsible for the roughening, the island formation, and thus the changes in the CV during the ORCs.

It was concluded that the PE_{rev} takes place randomly similar to a 2D adatom gas. However, the formation of a semi-ordered oxide structure, like local 1D chains, can not be fully excluded [41,71]. The latter would match with the fact that rows of PtO_2 units have been observed on Pt(111) with STM in "vacuum" under 1 bar of oxygen pressure and at 529 K [86]. In addition, the stability of rows at electrochemical potentials, similar to the ones for oxygen adsorption, was supported by DFT [87]. The formation of the rows during the PE_{rev} would also explain the existence of a critical coverage and potential, see above. It would result in an increase of the surface stress (i.e. as a consequence of the lattice mismatch between Pt(111) and PtO_2), which becomes larger as the rows grow in length. Once the critical stress is surpassed, the PE_{irr} starts, and one PE_{irr} atom per row is pushed out onto the terrace, thereby decreasing the local surface stress [65].

Van Spronsen et al. [86] observed that these oxide rows, or "spokes", arrange in "spoke-wheel" structures with hexagonal symmetry: triangles of spokes delimiting triangular terraces. Figure 2.2a shows an ideal, fully ordered spoke-wheel structure, in which each of the spokes consists of 8 elevated PtO_2 units (PE_{rev} atoms), at the expense of 9 Pt surface atoms. The length of a row consisting of 8 PtO_2 coincides almost exactly with the length of a row of 9 Pt surface atoms, and thus the surface stress is minimum in this configuration. The "missing" Pt atom per spoke is pushed out onto the triangular terraces during the PE_{irr}, creating a PtO_2-adatom. On average, this results in 1.5 PtO_2-adatoms formed in each triangle (i.e. two PtO_2-adatoms in every second triangle, while only one adatom in the other triangles) and hence a total of 9 adatoms formed per spoke-wheel. However, in reality, the spokes might not arrange into perfect spoke-wheels: some degree of disorder is present that is either caused by entropy or by a kinetic limitation during their formation (see Fig. 2.2b) [86].
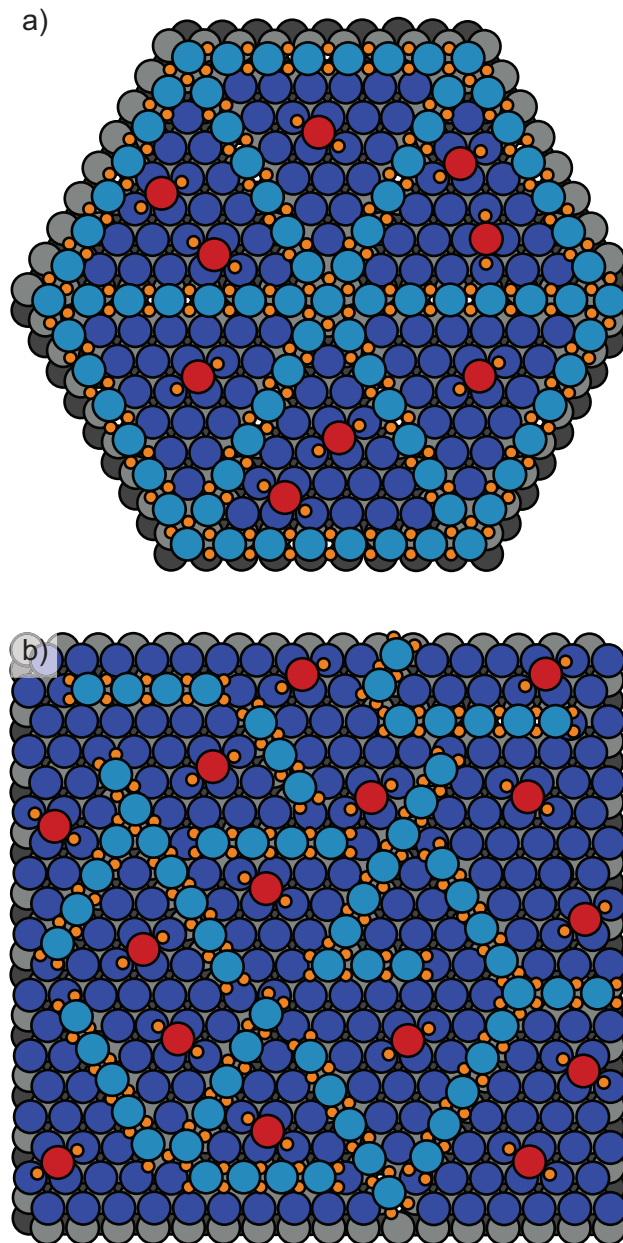
Figure 2.2: The Irreversible Place-Exchange Regime. The Pt atoms of the original, flat terrace are colored in dark blue, the lifted PE_{rev} atoms in light blue, forming spokes or rows, the oxygen atoms in orange, and the PE_{irr} atoms that are pushed onto the terrace, thus becoming PtO_2-adatoms, in dark red. The PtO_2-adatoms lead eventually to the growth of the nano-islands. **(a)** shows one fully ordered spoke-wheel structure without any disorder present. However, from [41,71,86] we know that, probably due to entropy, a certain degree of disorder is present. Therefore, **(b)** shows an impression of a disordered spoke-wheel phase: elements of the original triangles are still visible, in which the PtO_2-adatoms, the PE_{irr} atoms, are *trapped*.

17

2.4   Formation of Adatoms and Adatom Islands

As the PtO_2-adatoms are formed during the PE_{irr}, one naturally would assume that the formation of the adatom islands takes place also during this regime. However, two independent STM studies stated that the islands can not be observed during the oxidation up to 1.3 V, but become visible only when the surface is subsequently reduced [24, 40]. There are two possible explanations for this. The first one is that the PtO_2 islands are actually present already at 1.3 V, but can not be easily identified with an STM. This is because the Local Density of States (LDOS) of PtO_2 is significantly lower than the LDOS of bare platinum, leading to a major decrease in the tunneling current, and hence a lower apparent height than the 1 ML height expected (if tunneling *filled states*). Moreover, it might be almost impossible to distinguish between PtO_2-adatom islands and the PE_{rev} atoms, as the latter are also lifted nearly 1 ML from the surface, and also do have a different LDOS than the bare platinum. Wakisaka et al. reported that the Pt(111) surface becomes bumpy during the anodic sweep where tiny dots appear that are lifted around half a monolayer in height. It could be that these dots are the PE_{rev} atoms, but it might also very well be that they are irreversible, pushed out PtO_2-adatoms, or even small PtO_2-adatom islands that will become larger upon further growth. The second possible explanation, to why the islands could not be observed with an STM during the oxidation, is that indeed the islands are not formed until the surface is reduced. Even if the PtO_2-adatoms are formed during the PE_{irr} regime, whether these PtO_2-adatoms nucleate into islands depends both on their concentration and their mobility, such that thermodynamic as well as kinetic considerations have to be taken into account.

In order to provide further insight into the precise formation of the islands, we applied DFT to extract thermodynamic formation energies and kinetic diffusion barriers, all of which are important in the nucleation of Pt- as well as PtO_2-adatoms into islands, on both an oxidized as well as reduced Pt(111) surface.

2.4.1   Thermodynamic Requirements for Nucleation

In order to study the nucleation of adatom islands, we need first to introduce the chemical potential of adatoms, which is described as follows [88]:

$$\mu_{ad} = \mu_0 + k_B\,T\,\ln(\tfrac{\theta_{ad}}{1-\theta_{ad}}) + W(\theta_{ad}) \approx \mu_0 + k_B\,T\,\ln(\theta_{ad}) \qquad (2.1)$$

where μ_0 is the ground state energy of an adatom (and thus the adatom formation energy), k_B is the Boltzmann constant, T is the temperature, θ_{ad} is the adatom concentration on the surface, and $W(\theta_{ad})$ describes the interaction energy between adatoms. The entropy term $k_B\,\ln(\tfrac{\theta_{ad}}{1-\theta_{ad}})$ accounts for the number of free sites where an adatom can be placed (i.e. similarly to the entropy term in a Langmuir isotherm) and can usually be approximated to $k_B\,\ln(\theta_{ad})$, as in most cases the adatom concentration is very low. Moreover, the adatom interaction term $W(\theta_{ad})$ is small in comparison to the other terms such that it can typically be neglected, especially for low coverages.

Thermodynamic equilibrium requires the equilibration of all chemical potentials such

that the surface will maintain the equilibrium adatom concentration ($\theta_{eq,ad}$) by a balanced mass transport of adatoms from step- and, in particular, kink-sites to the terraces and back.

At constant temperature, changes in the actual adatom concentration (θ_{ad}) are only possible during surface growth (or etching), which originates from the increased (decreased) chemical potential created by the additional flux of adatoms (or vacancies) during, e.g. an MBE (or sputtering) experiment.

When surface growth (or etching) stops, the surface will pursue to reestablish the thermodynamic equilibrium. If θ_{ad} is lower than $\theta_{eq,ad}$, the equilibrium is restored by the formation of additional adatoms that detach from kinks and diffuse onto the terrace. If on the other hand, θ_{ad} is higher than $\theta_{eq,ad}$, adatoms on the terrace quickly diffuse towards the steps, where they finally get incorporated at kinks. At too high deposition flux, where the surface no longer will revert back to its lowest free energy configuration, adatoms find each other before encountering the steps during their random walk (which depends on the flux, the mobility, and their distance to the step), and nucleate into adatom islands to locally lower the enhanced chemical potential. Neglecting for the moment any kinetic arguments we can therefore conclude that nucleation is only possible if $\theta_{ad} >> \theta_{eq,ad}$.

Realizing the importance of the equilibrium Pt-adatom background pressure, $\theta_{eq,Pt,ad}$, on the thermodynamics of nucleation, one can calculate $\theta_{eq,Pt,ad}$ by using the Boltzmann equation:

$$\theta_{eq,Pt,ad} = exp\left(-\frac{E_{Pt,ad}}{k_B T}\right) \tag{2.2}$$

in which $E_{Pt,ad}$ is the formation energy of a Pt-adatom, defined as the energy required to take an atom from a kink site and place it onto the terrace, and T is room temperature, $T = 298$ K.

As estimated from our DFT calculations, $E_{Pt,ad}$ is 1.2 eV independently of the electrode potential (see the orange line in Fig. 2.3a). This gives rise to a potential-independent equilibrium adatom density of only $\theta_{eq,Pt,ad} = 5 \cdot 10^{-21}$, shown with the orange line in Fig. 2.3b. Therefore, the use of the Boltzmann equation, which includes the approximation in the entropy term explained before and neglects the adatom-adatom interaction, is well justified (see Appendix A for further details). As usual, the numbers obtained from DFT should be taken with some care, due to the inherent error margin of this methodology. However, the order of magnitude is typically captured correctly. In this work, the effect of near-surface solvation on the formation of a Pt- or PtO$_2$-adatom has not been considered, and while we expect it to have small influence on the energy difference between a Pt- and a PtO$_2$-adatom on Pt(111) (as the magnitude of the surface-normal dipole moments are small), this should be evaluated in future work. In our case, however, the error associated does not change significantly the atomic picture, and hence the message is still the same. With a typical error of 0.2 eV, $E_{Pt,ad}$ would be 1.0 eV instead of 1.2 eV, resulting in $\theta_{eq,Pt,ad} = 10^{-17}$, which is still very low.

From Fig. 2.1 we know that first the steps, and then the terraces oxidize. This is expected, as lower coordinated sites (i.e. the steps) bind an oxygen atom more strongly [1]. Similarly, considering the oxidation of Pt-adatoms, which to our knowledge has not been
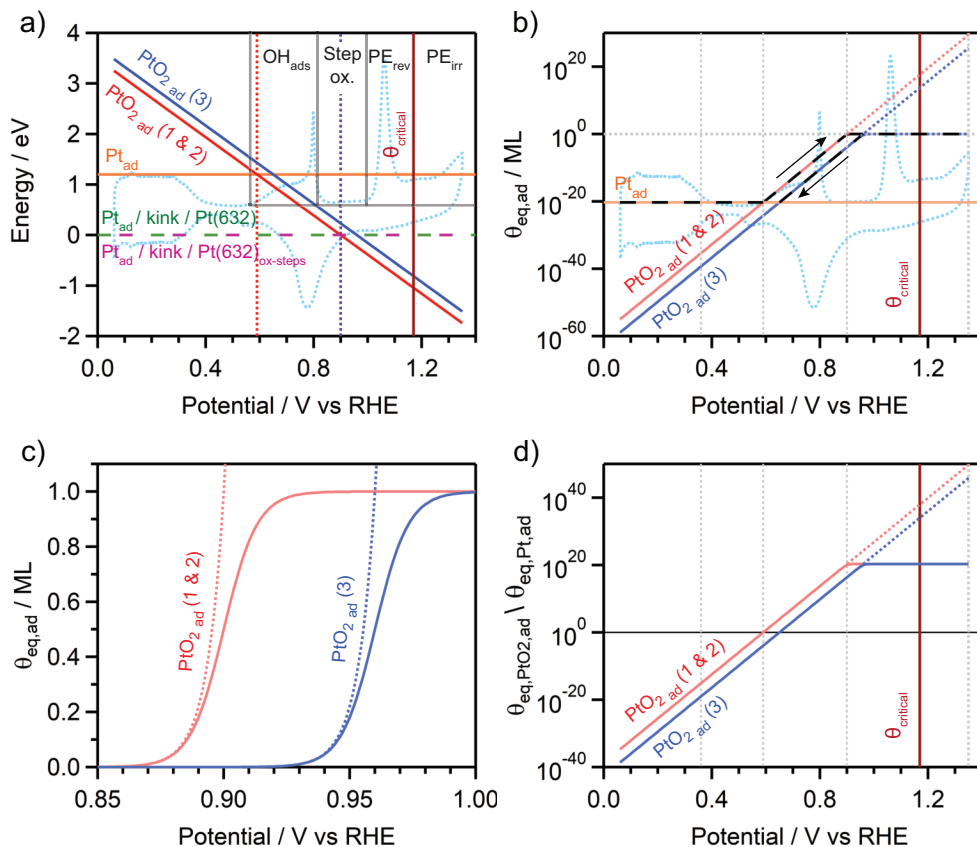
Figure 2.3: Formation Energies and Concentrations of Adatoms. **(a)** The formation energies of a Pt-adatom and a PtO$_2$-adatom on Pt(111), and a PtO$_2$-adatom on a Pt(111) with 4/25 ML O$_{ads}$, are shown in orange, red, and blue, respectively. They are referenced with respect to the binding energy of an additional Pt atom attached to a kink site on Pt(632), which can be unoxidized (green dashed line) or oxidized (pink dashed line). The numbers in brackets indicate the reactions considered, as explained in the main text. The vertical dotted red and purple lines indicate the Pt-adatom oxidation potential and the potential at which $E_{PtO_2,ad}$ (1&2) becomes zero, respectively. The first ORC is shown in dotted light blue and the different regions are indicated. **(b)** Equilibrium Pt- and PtO$_2$-adatom concentrations calculated from **(a)**. The dotted red and blue lines result from the Boltzmann equation which match, respectively, the solid red and blue lines (considering the entropy term without approximation) at potentials < 0.85 V. The dashed black line and the arrows indicate the path followed upon one ORC, while the vertical lines indicate the potentials used in Table 2.1. **(c)** Zoomed-in graph of the region between 0.85 V and 1.00 V in **(b)**. **(d)** Concentration ratios between PtO$_2$- and Pt-adatoms.

studied before, one would expect them to oxidize before 0.8 V, during the anodic sweep. Consequently we have calculated, using DFT, the energy required to form a PtO$_2$-adatom

from a kink site. In general, we have to distinguish three different reaction pathways. In the first one (see eq. 2.3 below), a pure Pt adatom (see Fig. 2.4b) is created from a kink-atom at an unoxidized step ($Pt_{ad}/kink/Pt(632)$ in Fig. 2.4a), and oxidizes immediately when diffusing onto the terrace, leading to a PtO_2-adatom (Fig. 2.4c). In the second one (eq. 2.4), a PtO_2-adatom is created from a Pt atom at a kink on an oxidized step ($Pt_{ad}/kink/Pt(632)_{ox-steps}$ in Fig. 2.4d), while taking with it two oxygen atoms such that the remaining "empty" kink site has to be reoxidized. Finally, in the third reaction pathway (eq. 2.5) both the steps and the terraces are oxidized, and the PtO_2-adatom is created from a kink ($Pt_{ad}/kink/Pt(632)_{ox-steps}$) by placing such a unit onto the terrace (see Fig. 2.4e).

$$Pt_{ad}/kink/Pt(632) - Pt(632) + Pt(111) + 2\,H_2O \rightarrow PtO_{2\,ad}/Pt(111) + 4\,H^+ + 4\,e^- \quad (2.3)$$

$$Pt_{ad}/kink/Pt(632)_{ox\text{-}steps} - Pt(632)_{ox\text{-}steps} + Pt(111) + 2\,H_2O \rightarrow PtO_{2\,ad}/Pt(111) + 4\,H^+ + 4\,e^- \quad (2.4)$$

$$Pt_{ad}/kink/Pt(632)_{ox\text{-}steps} - Pt(632)_{ox\text{-}steps} + Pt(111)_{ox} + 2\,H_2O \rightarrow PtO_{2\,ad}/Pt(111)_{ox} + 4\,H^+ + 4\,e^- \quad (2.5)$$
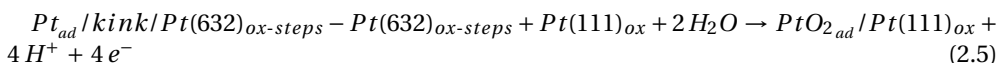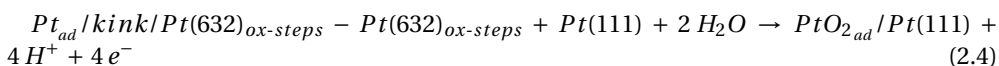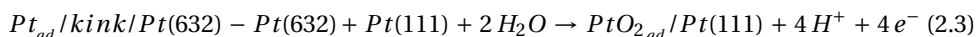
where the slash stands for "at", e.g. $Pt_{ad}/kink/Pt(632)$ stands for a Pt-adatom at a kink site at a Pt(632) surface, and "ox" stands for "oxidized".
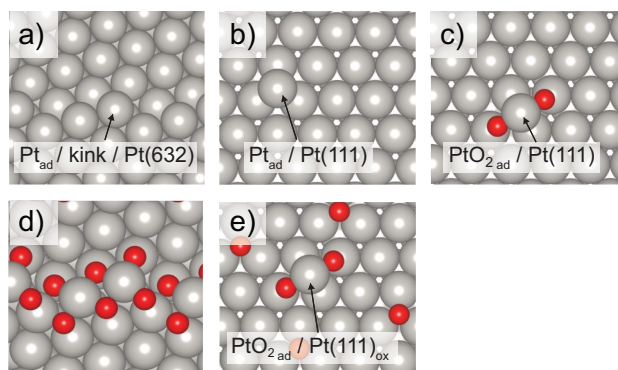
Figure 2.4: Ball Models of Step and Adatom Configurations. (a) Bare platinum step on a Pt(632) surface, which was used to calibrate the total energy scale via the Pt-adatom at the kink site. **(b)** Pt-adatom on an fcc site on a Pt(111) terrace. **(c)** PtO_2-adatom on a bridge site on a Pt(111) terrace. **(d)** A fully oxidized step forming PtO_2 oxide chains similar to the spokes on the terraces [89, 90]. **(e)** PtO_2-adatom on a bridge site on a Pt(111) terrace that is covered with a perfectly ordered 4/25 ML O_{ads} superstructure.

Figure 2.3a shows in red the potential-dependent formation energy of a PtO_2-adatom on Pt(111). As this energy is the same for both reaction pathways, creation from an unoxidized step (eq. 2.3) and from a fully oxidized step (eq. 2.4), we consider both cases together and name the corresponding formation energy $E_{PtO_2,ad}$ (1&2). We used the energy of an additional Pt atom attached directly to a kink site on Pt(632) as a reference for the formation energy of a PtO_2-adatom. As we find that the formation energy of an adatom is nearly the same whether we reference an oxidized or a non-oxidized kink site on Pt(632), we have de-

cided to independently consider adatom formation and Pt(632) step/kink oxidation. Moreover, as we calculate the adatom formation energy with a constant oxygen coverage in our reference state, both oxidized and non-oxidized kink reference states have the same energy, see Fig. 2.3a. We have separately plotted the thermodynamics of the oxidation of step/kink sites on Pt(632) as a function of oxygen coverage along the step in Fig. A.2, in Appendix A. A 3-dimensional plot would be required to simultaneously consider varying the adatom coverage and the oxygen coverage. We leave this for future work, but do not expect it to affect our conclusions, again given that the adatom formation energy from an oxidized kink at constant oxygen coverage is not significantly different to that from a bare kink.

As the formation energies $E_{PtO_2,ad}$ (1&2) cross $E_{Pt,ad}$ at 0.59 V, this defines the equilibrium potential at which the Pt-adatoms oxidize to PtO_2-adatoms, according to:

$$Pt_{ad} + 2\,H_2O \leftrightarrow PtO_{2\,ad} + 4\,H^+ + 4\,e^- \tag{2.6}$$

Equipped with the potential dependent formation energy, $E_{PtO_2,ad}$ (1&2), we calculate the equilibrium concentration of PtO_2-adatoms, $\theta_{eq,PtO_2,ad}$(1&2), again by using the Boltzmann equation. As $E_{PtO_2,ad}$ (1&2) decreases with potential, $\theta_{eq,PtO_2,ad}$ (1&2) increases, see the red line in Fig. 2.3b. Consequently, above 0.59 V the ratio $\frac{\theta_{eq,PtO_2,ad}\,(1\&2)}{\theta_{eq,Pt,ad}}$, which gives an indication for the driving force to oxidize a Pt-adatom, becomes larger the higher the potential is: while at 0.59 V it is equal to 1 (equal concentration of Pt-adatoms and PtO_2-adatoms), it is already a factor 8000 higher at 0.65 V, see the red line in Fig. 2.3d. As the potential increases further, $E_{PtO_2,ad}$ (1&2) becomes larger, up to the point that the Boltzmann equation results in $\theta_{eq,PtO_2,ad}$ (1&2) = 1 at 0.90 V, and even adatom concentrations larger than 1 ML at potentials above (see the dotted red line in Fig. 2.3b). The Boltzmann equation does not hold at these high adatom coverages. However, in first instance this can be solved by using the full entropy term in the adatom chemical potential equation, $k_B \ln(\frac{\theta_{eq,ad}}{1-\theta_{eq,ad}})$, instead of the approximation to $k_B \ln(\theta_{eq,ad})$ (see Appendix A). The equilibrium adatom concentration is then given by:

$$\theta_{eq,Pt,ad} = \frac{exp(\frac{-E_{ad}}{k_B T})}{1 + exp(\frac{-E_{ad}}{k_B T})} \tag{2.7}$$

In Appendix A, we evaluate the error one makes when using the Boltzman approximation and show that it is as low as $6 \cdot 10^{-4}$ for $\theta_{eq,PtO_2,ad}$ (1&2) up to 0.85 V.

By using the equation with the full entropy term, we now see in Fig. 2.3b that the equilibrium adatom concentration asymptotically approaches 1 ML with increasing potential. However, one has to realize that at these high coverages the definition of the adatom gas is no longer valid. Single, individual adatoms do only exist up to a coverage of 0.25 ML, as at higher coverages one connects at least 3 into a cluster. As the relative error between the Boltzmann approximation and the full solution is only 25 % at 0.25 ML, which is 0.25 ± 0.06 ML, the equilibrium adatom density is (for most applications) sufficiently well described already by the Boltzmann approximation.

Nevertheless, it is conceptually still interesting to consider the meaning of reaching a coverage of 1 ML. This situation is probably most comparable to the roughness transition

on surfaces, where at high enough temperatures the step free energy crosses zero and the surface can create as many steps as desired [91–95]. Derived from the chemical potential with a kink site as reference, 1 ML of coverage at 0.94 V implies the formation of a complete oxide layer. It is striking that the PE_{rev} starts around this potential, which describes the first part of the terrace oxidation [78].

We know from Fig. 2.1 and Refs. [61, 62] that the steps begin to oxidize at 0.8 V, and that full oxidation happens as late as 1.05 V, probably leading to oxide chains as observed in vacuum [89, 90]. Therefore, we also consider the situation in which a PtO_2-adatom is formed from a fully oxidized step (kink). As the formation energy, as explained before, is the same independently of whether the step is unoxidized or fully oxidized, it is still described by the red line in Fig. 2.3a. However, even if the thermodynamics of PtO_2-adatom formation do not change, the kinetics surely do. As a fully oxidized step forms a 1D-PtO_2 row, we expect that detaching a PtO_2-kink atom from such a step involves overcoming a significant barrier, and is thus kinetically limited (i.e. the PtO_2-kink atom has to "diffuse" out of the step). Consequently, $\theta_{eq,PtO_2,ad}$ (1&2) will not be reached (although, strictly speaking, it always would when given enough time) and, as then $\theta_{PtO_2,ad}$ (1&2) $< \theta_{eq,PtO_2,ad}$ (1&2), nucleation will not occurr. Furthermore, even if this kinetic barrier is small, to reach 1 ML PtO_2-adatoms the steps would need to retract with the same width. This would involve a large mass transport and thus require a very long time, i.e. $1.5 \cdot 10^5$ PtO_2-kink atoms need to be detached from the step to create 1 ML PtO_2-adatoms on a 100 x 100 nm^2 terrace.

At 1.17 V the PE_{irr} starts, leading to the formation of PE_{irr} atoms. As the terrace is then oxidized, we calculated also the formation energy of a PtO_2-adatom on a terrace covered with 4/25 ML O_{ads}, which we named $E_{PtO_2,ad}$ (3), see eq. 2.5 and the blue line in Fig. 2.3a. By comparing $E_{PtO_2,ad}$ (3) with $E_{PtO_2,ad}$ (1&2), it is evident that, once the terraces oxidize, it becomes energetically more expensive to form PtO_2-adatoms. Consequently, the equilibrium PtO_2-adatom concentration $\theta_{eq,PtO_2,ad}$ (3) is lower than $E_{PtO_2,ad}$ (1&2) at every given potential. Based on this result, we expect that the potential dependent formation energy of the PtO_2-adatoms shifts to even higher potentials the more the terrace is oxidized.

As there is a large driving force towards adatom oxidation, with $\frac{\theta_{eq,PtO_2,ad} (3)}{\theta_{eq,Pt,ad}} = 2 \cdot 10^{20}$ at 1.17 V), the PE_{irr} atoms are surely oxidized, thus PtO_2-adatoms. Mechanistically, there are two possible pathways for the formation of PtO_2-adatoms from the PE_{irr}: either the newly lifted PE_{rev} atoms are pushed out directly onto the terrace, where they immediately oxidize, or the PE_{rev} atom first tries extending an oxide row but then it is pushed onto the surface together with 2 oxygen atoms, due to the too high stress in the row. At 1.17 V, as well as at 1.35 V (the upper vertex potential during our ORCs) $\theta_{eq,PtO_2,ad}$ (3) is practically 1 ML. However, the actual concentration of PtO_2-adatoms formed during the PE_{irr} is only 0.0245 ML, obtained from a fit of the roughening evolution during 170 ORCs up to 1.35 V [80]. As 0.0245 ML is much lower than the 1 ML of critical coverage, even at 1.35 V the PtO_2-adatoms created will not nucleate into islands.

The situation changes completely during the backward (cathodic) sweep. Following the dashed black line in Fig. 2.3b from right to left, $\theta_{eq,PtO_2,ad}$ (3) decreases with decreasing potential. At 0.94 V, $\theta_{eq,PtO_3,ad}$ (3) becomes equal to $\theta_{PtO_2,ad}$, thus 0.0245 ML. Therefore,

upon decreasing the potential further, $\theta_{PtO_2,ad}$ needs to diminish in order to adapt to the decreasing equilibrium concentration $\theta_{eq,PtO_2,ad}$ (3), and hence the nucleation of PtO_2-adatoms into PtO_2-islands is now thermodynamically favorable. However, this still does not ensure that nucleation takes place, as one should also consider the kinetics, thus the mobility, of the PtO_2-adatoms. If the PtO_2-adatom diffusion is very slow, it will take a significant amount of time for the nucleation to occur. As the potential decreases even further, the equilibrium PtO_2-adatom concentration ($\theta_{eq,PtO_2,ad}$ (3), or $\theta_{eq,PtO_2,ad}$ (1&2) once the terraces are reduced) drops lower, thus rising the driving force for nucleation. This situation holds until 0.59 V, when the PtO_2-adatoms reduce back to Pt-adatoms and the equilibrium adatom concentration becomes constant. Anyhow, although $\theta_{eq,Pt,ad}$ is much lower (= $5 \cdot 10^{-21}$) than the coverage of PtO_2-adatom created during the PE_{irr} (= 0.0245 ML), the nucleation will still depend on kinetics, now on the mobility of the Pt-adatoms. Therefore, in order to solve the complete riddle, we also need to study the diffusion rates of both Pt- and PtO_2-adatom species. We discuss this in more depth in the next section.

	0.36 V (E_{pzc})	0.59 V	0.90 V	1.17 V	1.35 V
$\theta_{eq,Pt,ad}$	$5 \cdot 10^{-21}$	$5 \cdot 10^{-21}$	–	–	–
$\theta_{eq,PtO_2,ad}$ (1&2)	$4 \cdot 10^{-36}$	$5 \cdot 10^{-21}$	0.5	–	–
$\dfrac{\theta_{eq,PtO_2,ad}\ (1\&2)}{\theta_{eq,Pt,ad}}$	$9 \cdot 10^{-17}$	1	$1 \cdot 10^{20}$	–	–
$\theta_{eq,PtO_2,ad}$ (3)	–	–	–	1	1
$\dfrac{\theta_{eq,PtO_2,ad}\ (3)}{\theta_{eq,Pt,ad}}$	–	–	–	$2 \cdot 10^{20}$	$2 \cdot 10^{20}$

Table 2.1: Pt- and PtO$_2$-adatom Equilibrium Concentrations and their Ratios. We only provide relevant values at each of the potentials: if the terraces are not oxidized, we consider $\theta_{eq,PtO_2,ad}$ (1&2), while we consider $\theta_{eq,PtO_2,ad}$ (3) if the terraces are oxidized. E_{pzc} stands for potential of zero charge of Pt(111) [96, 97].

2.4.2   Kinetic Requirements for Nucleation

As the probability for nucleation does not only depend on the supersaturation (i.e. how much the adatom concentration exceeds the equilibrium adatom concentration), we will in the following consider also the effects of (limited) adatom mobility. For nucleation to occur during the oxidation sweep, the PtO_2-adatoms must diffuse over the terrace, find each other, and overcome the critical nucleus size, as only clusters larger than the critical nucleus size do not decay [37]. If the diffusion of the PtO_2-adatoms is slow, then it will take longer times for the adatoms to find each other and therefore the nucleation will be delayed. In the extreme limit when diffusion is completely kinetically hindered, nucleation does never take place.

Using DFT, we calculated the diffusion barrier of a Pt-adatom on Pt(111), $E_{Pt,ad,Diff}$, to be 0.28 eV. This value is close to the 0.26 eV obtained in two different studies, one which combines STM with MC simulations [98] and the other one based on Field Ion Microscopy measurements [99], and not significantly far from the 0.16 eV calculated by an early Effective Medium Theory study [100]. Using this value, we can calculate an approximation of the Pt-adatom jump rate by using an Arrhenius-type equation:

$$\nu_{ad} = \nu_0 \, exp \left(-\frac{E_{Pt,ad,Diff}}{k_B \, T} \right) \qquad (2.8)$$

in which ν_{ad} is the jump rate and ν_0 is the attempt frequency, given by the vibrational frequency (10^{13} Hz) for single metal atoms. As a result, we obtain a Pt-adatom jump rate of 10^8 jumps/s.

We have also calculated the relative energy of a PtO_2-adatom on a Pt(111) surface at different adsorption sites: bridge1, bridge2, atop, fcc and hcp (see Fig. 2.5). The most stable configuration is bridge1, which was used as reference to compare with the energetics of the others. Within the configurations calculated, a PtO_2-adatom in bridge1 has an energy that is at least 0.78 eV lower than all other configuration considered. While these are just thermodynamic arguments, and further DFT calculations on the kinetics of PtO_2-adatom diffusion would be beneficial (but are left for future work), the change in energy when moving from one site to another gives an estimate on the diffusion barrier, within the error margins that are characteristic from DFT. We expect the diffusion barrier of a PtO_2-adatom to be at least as high as 0.78 eV, and obtain a PtO_2-adatom jump rate of only 0.28 jumps/s, which is approximately 10^9 times less than the jump rate of a Pt-adatom. To demonstrate how slow this PtO_2-adatom diffusion is, we estimate how many jumps one PtO_2-adatom can perform during the cathodic sweep. Decreasing the potential from 1.35 V to 0.59 V (where PtO_2-adatoms reduce to Pt-adatoms) with 50 mV/s leads to a reduction time of 15.2 s. In this time, a PtO_2-adatom can only do 4 jumps. This is not enough to encounter other PtO_2-adatoms, and therefore nucleation will not occur.

a)	b)	c)	d)	e)
E = 0 eV	1.13 eV	0.78 eV	0.82 eV	1.35 eV
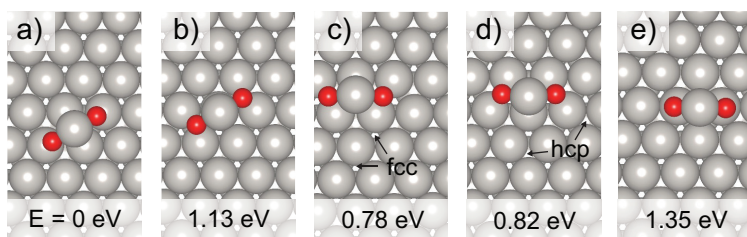
Figure 2.5: Potential Energy Landscape of a PtO_2-adatom (PE_{irr}-adatom) on Pt(111): (a) bridge1, **(b)** atop, **(c)** fcc, **(d)** hcp, **(e)** bridge2. The lowest energy state, the energy of a PtO_2-adatom at bridge1, is used as reference. The diffusion barrier of a PtO_2-adatom must be at least 0.78 eV.

In addition to this extremely low jump rate, as the PE_{rev} involves the formation of spoke-wheels, the PtO_2-adatoms formed during the PE_{irr} will be "trapped" within the triangular areas. The reason for this is that the spokes delimiting the triangles are lifted nearly one monolayer high above the terrace, preventing the PtO_2-adatoms from diffusing across [65].

Even if the spoke-wheels are distorted, like in Fig. 2.2b, a PtO_2-adatom can only "escape" from a triangle if it finds the open pathway between the spokes. This requires a significant amount of time, as the PtO_2-adatom needs several attempts during its random walk to find this open path. Even if nucleation is thermodynamically favourable, it will take quite a long time to occur. This limited diffusion also extremely hinders mass transport between the terrace sites and the kinks, thus preventing a quick equilibration of the chemical potentials and the required adatom concentration.

If we now consider that the critical nucleation *cluster* would be a single adatom, meaning that the smallest stable cluster would be a dimer, and that diffusion between triangles is fully prohibited, nucleation would only occur in those triangles that have received two PtO_2-adatoms: thus in 50% of the triangles, as there is, on average, the formation of 1.5 PtO_2-adatoms per triangle. In the case that a dimer would be the critical nucleus size, one additional PtO_2-adatom would be needed for all the dimers to form a stable nuclei. As this only can come from neighboring triangular areas, a single PtO_2-adatom has to "escape" its own triangular area, finding its way through the open paths between the spokes. Statistically, this would lead to every second triangle with a stable trimer, while the others would not have any adatom.

Once the spokes reduce during the broad cathodic peak at around 0.8 V (see Fig. 2.1), the PtO_2-adatoms can freely diffuse over the Pt(111) terrace, although, as commented before, only with 0.28 jumps/s (compare to the Pt-adatoms with 10^8 jumps/s). Therefore, even though below 0.94 V $\theta_{eq,PtO_2,ad}$ (3) has decreased such that now $\theta_{PtO_2,ad}$ is larger (i.e. $\theta_{PtO_2,ad} = 0.0245$, as this is the flux of PtO_2-adatoms created during the PE$_{irr}$ [80]), nucleation will not occurr within the time needed to reach 0.59 V during the cathodic scan. At 0.59 V, the PtO_2-adatoms reduce to Pt-adatoms, which probably explains the cathodic peak starting at around this potential. As the Pt-adatoms diffuse with 10^8 hops per second, instant nucleation occurs. Interestingly, Wakisaka et al. reported that they could not observe the islands until the potential was reduced to 0.49 V [24], which would point out that Pt-adatoms, and not PtO_2-adatoms, are the species involved during nucleation.

Due to the non-random character of both the PE$_{rev}$ and the PE$_{irr}$ processes, the islands resulting from the nucleation are distributed within a certain distance to each other, as observed in Ref. [65]. More concretely, there are two possible reasons for this. The first one is that the PtO_2-adatoms are formed within a certain distance between each other, therefore leading also (statistically) to nuclei with a homogeneous distance distribution. The second one is that the PtO_2-adatoms are retained so long within their triangular areas of origin that, once the spokes are reduced, the statistical distance between the PtO_2-adatoms is equal and thus, on average, all PtO_2-adatoms need the same number of local random walks on the surface before a nucleation event occurs. Once the islands are formed, processes such as Ostwald ripening (i.e. atom diffusion from the smaller to the larger islands) and/or Smoluchowski ripening (i.e. smaller islands diffusing as a whole unit and getting incorporated into the larger, less mobile islands nearby) become important [101–103], and result in a larger averaged island size at the expense of a lower island density.

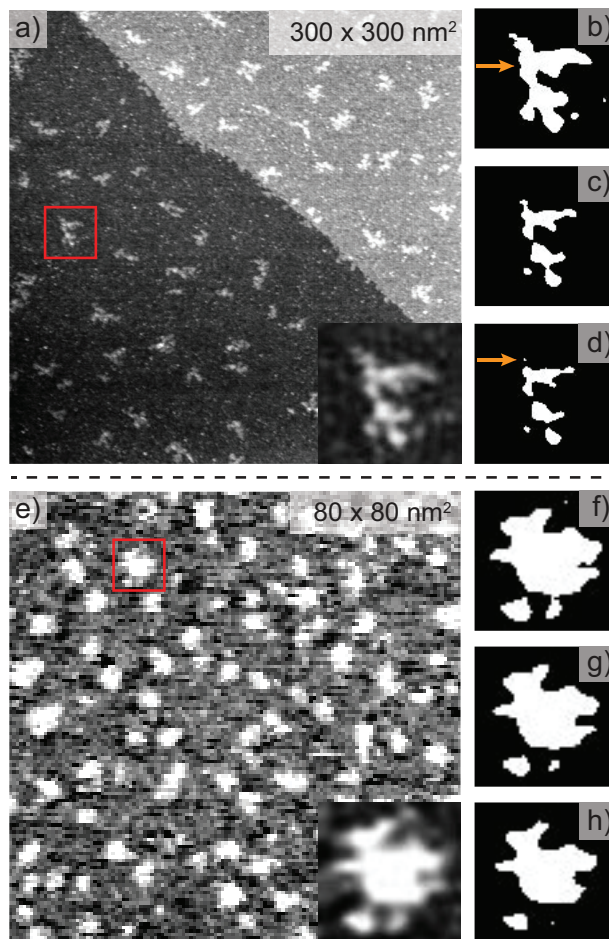## 2.5 Dendritic Islands and their Step Length

Figure 2.6: Dendritic Islands on Pt(111). (a) Vacuum-STM image of dendritic islands formed after a potential step from 1.0 to 1.3 V, holding 1.3 V for 10 s, and stepping back to 1.0 V before finally sweeping to 0.05 V at 50 mV/s. The image is reproduced with permission from T. Maagaard [40]. **(b)**, **(c)** and **(d)** are the upper, the best, and the lower estimate, respectively, of the area of the island marked with a red square in **(a)**. **(e)** Dendritic islands observed with our EC-STM after holding the potential at 1.35 V for 200 s, and then reducing to 0.3 V with 25 mV/s. This image was recorded by L. Jacobse, with $U_s = 300$ mV, $U_t = 310$ mV, and $I_t \approx 300$ pA. **(f)**, **(g)** and **(h)** are the respective upper, best, and lower estimate of the area of the island marked in red in **(e)**.

Figure 2.6a shows an STM image (reproduced with permission from [40]) of islands created by stepping the potential from 1.0 V to 1.3 V and holding it there for 10 seconds, before stepping back to 1.0 V, and finally sweeping with 50 mV/s to 0.05 V to completely reduce the oxide. Subsequently, the Pt(111) sample was taken out of the electrolyte, dried, and

mounted inside a vacuum-STM chamber to perform the imaging. Interestingly, the islands created in this way are dendritic, and not hexagonal as reported in the EC-STM study in Ref. [26].

Figure 2.6e shows an EC-STM image (taken in the electrolyte) of the islands formed by sweeping the potential from 0.3 to 1.35 V at 25 mV/s and holding it there during 200 s before sweeping back to 0.3 V at 25 mV/s to reduce the oxide. Upon closer inspection, one can see that also these islands are dendritic in shape, although more compact than the ones measured in vacuum (compare with Fig. 2.6a).

The origin of the dendritic islands requires a growth instability that is caused by the Kink Ehrlich-Schwoebel Effect (KESE). The reason for this energetic barrier is manifested in the lower coordination of an atom diffusing around a kink when it is at the transition state. Its similarity with the one dimensional higher (3D instead of 2D) Ehrlich-Schwoebel barrier [81, 82] was realized for the first time by Pierre-Louis [104, 105]. Figure 2.7 sketches the general mechanism for the formation of dendritic islands. The arrival of adatoms to an island edge, given by a step, leads to the nucleation of a 1D island step-row (in full similarity to island nucleation on a terrace). In analogy to mound formation in 3D [80, 106], these 1D islands grow in the perpendicular direction to the step, because of the limited diffusion around the kinks introduced by the KESE. The faster the arrival of the adatoms (i.e. the higher the flux) towards the island edge, the higher the growth speed becomes in the perpendicular direction to the step. As the diffusion barriers are flux independent, this implies that there is less time for the arriving atoms to try hopping around the corner and thus overcoming the KESE. In other words, the remaining growing triangles do become shorter at their base, and it might be even possible to nucleate two 1D rows, thus two triangles, at one step edge. Therefore, a sudden large flux of adatoms that are released during the reduction of the PtO$_2$-adatoms significantly favors the formation of even smaller branches that are characteristic for the dendritic shape. Once these branches are formed, they ramify by the incorporation of new adatoms to the edges of the branches, thus once again forming 1D islands that grow.

The island shape, especially the ratio of the perimeter to area and thus also the ratio of step sites to terrace sites, crucially effects the ORR activity as well as the catalyst degradation [107, 108]. Calle-Vallejo et al. [1] reported that the ORR activity measured at 0.9 V increased more than three times after roughening a Pt(111) electrode by performing 10 ORCs up to 1.72 V, which is likely below the 2D to 3D transition growth state of the islands [25].

In order to measure the perimeter and the area of the dendritic islands, we first need to delimit the island boundaries. This is far from trivial, as STM images suffer inherently from tip convolution, which is more severe the smaller the feature sizes and the larger the tip radius. Realizing the dendritic island shape with its tiny branches, we obviously need a careful approach for the proper determination of the perimeter. The approach chosen for the analysis and the effect of tip convolution could be the reason why in Ref. [26] it was suggested that the islands were hexagonal.

Starting with the more branched islands measured in vacuum, we decided to define an upper, best, and lowest estimate of the island area, as shown for the particular example dis-
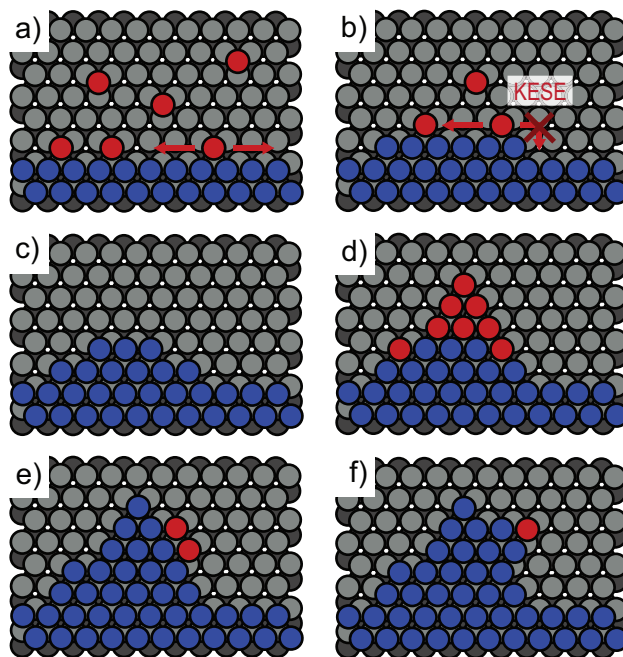
Figure 2.7: Scheme of the Growth Instability (KESE) resulting in Dendritic Islands: (a) Step-adatom (1D) diffusion resulting in the nucleation of 1D-island rows. **(b)** The KESE makes it more difficult for the atom to diffuse around the kink, leading to the nucleation and growth of a second row **(c)**. **(d)** The arrival of more adatoms leads eventually to the growth of triangles (branches) perpendicular to the step. **(e)** Nucleation of a new row on the side of a triangle, which finally results in the bifurcation of the branch **(f)**.

played in Fig. 2.6(b-d). In order to determine the different estimates, we first changed the color scale to gray scale, which delivers higher contrast. Then, using a threshold routine that displays everything above the threshold in white and below in black, we generated the images. The upper estimate was generated by decreasing the threshold until the shallow trenches within the island were almost filled (note the trench indicated with the orange arrow in Fig. 2.6b as an example). For the lower estimate, we increased the threshold until one of the parts clearly forming the island almost disappeared (see the part marked with the orange arrow in Fig. 2.6d). This lower estimate ensures that we account also for tip deconvolution. In the best estimate, which is the one used in the further analysis, we adjusted the island area as accurate as possible to the upper part of the island (step) height. The upper, the best, and the lowest estimates of the area of the islands measured in electrolyte were obtained in the same way (see Fig. 2.6(f-h) as an example).

To quantify the degree of the dendritic shape, we defined a roughness factor of the island edge (ϵ_r) as follows:

$$\epsilon_r = \frac{L_{dendritic}}{L_{circular}} \tag{2.9}$$

where $L_{dendritic}$ is the perimeter (step length) of the dendritic island in the best estimate and $L_{circular}$ is the perimeter of a circular island of exactly the same area, calculated as:

$$L_{circular} = 2\sqrt{\pi A} \tag{2.10}$$

where A is the area of the dendritic island in the best estimate.

Figure 2.8 shows the statistical distributions of ϵ_r obtained from analyzing 200 islands imaged in vacuum (a) and 250 islands imaged in the electrolyte (b). The maximum in the fit of the ϵ_r distribution for the vacuum measurement has a higher value, $\epsilon_r = 1.96$, than the maximum in the fit of the ϵ_r distribution for the measurement in electrolyte, $\epsilon_r = 1.63$. One possible explanation for this is that the STM resolution at the island edges is lower in electrolyte than in vacuum, as the work function is approximately three times larger in the latter case [44]. One could try to compensate this effect by increasing the tunneling current, hence decreasing the distance between tip and sample, but this would also lead to a worse signal-to-noise and more instabilities in the feedback loop of the STM, as the same mechanical noise would be also exponentially increased. Next to this purely technical reason, the precise experimental details for the island creation also determines the degree of the dendritic shape and thus the measured ϵ_r, as we explain in the following.

The size of the islands is dictated by the ratio F/M that was described in the Introduction. A higher flux leads to smaller islands, while a higher mobility leads to larger islands [17, 25, 80]. While both the higher upper potential and the longer oxidation time, for the EC-STM measurements, result in a larger effective flux, the slower scan rate during the cathodic sweep results in a higher mobility (i.e. the adatoms have more time to diffuse before nucleating into islands). As becomes clear from the above, these two effects point towards opposite directions: a decrease and an increase, respectively, of the island area. However, by comparing the islands in Fig. 2.6a with the ones in Fig. 2.6e, one can see that the latter are significantly smaller (note the different image sizes), and therefore, the increase of the upper potential and the oxidation time must outweigh the higher mobility introduced by slower sweeping. Smaller islands are more difficult to analyze accurately than larger ones, recall the above explained tip convolution. This leads to a lower measured ϵ_r, as the small scale roughness at the island edges can not easily be captured. As explained before, the faster the arrival of adatoms towards the island edge, the more pronounced the dendritic growth becomes. Therefore, a faster scan rate during the cathodic sweep, and thus faster reduction of the PtO_2-adatoms to Pt-adatoms (which have a higher diffusion rate) results in a larger ϵ_r.

As delimiting the island edges is subject to error, we used the three estimates measured for each island to calculate the lower and upper errors of ϵ_r. This was done by dividing, respectively, the smallest perimeter with the largest area, and the largest perimeter with the smallest area, before averaging over all the islands. This resulted in a lower and an upper error of 23 % and 25 %, respectively, for the islands measured in vacuum. For the islands measured in electrolyte, we found an upper and lower error of 21 % and 30 %, respectively. Realizing both upper and lower errors, one could argue that there is no difference in the ϵ_r between both measurements, as the difference in the two peak maximum values falls within this error margin. This is clearly observed in Fig. 2.8, where both upper and lower
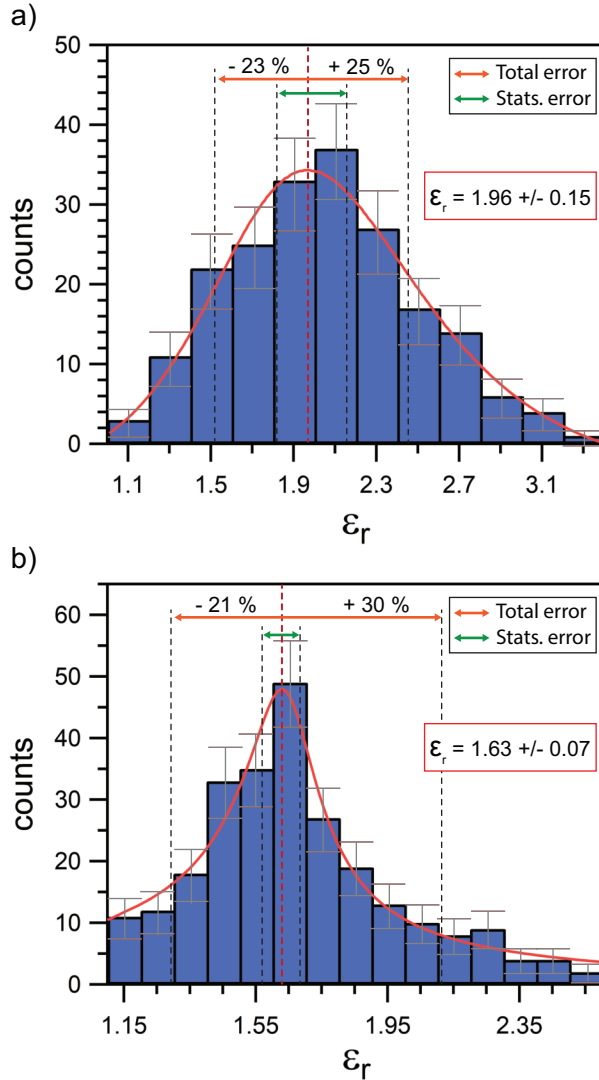
Figure 2.8: Statistical Distribution of ϵ_r for the Best Estimate of the Island Shapes: (a) measured in vacuum (analyzed from Fig. 2.6a and Fig. A.3 in the Appendix A) and **(b)** in electrolyte (analyzed from Fig. 2.6e and Fig. A.5 in Appendix A). The peak maximum of the statistical distributions, obtained by fitting with a Pearson IV function, are indicated with red dashed lines. The lower and upper bound are indicated with the orange arrow, while the statistical error, derived via the possible shift within the statistical error bars, is indicated with the green arrow.

boundaries are shown. However, the upper and lower bounds are larger than the natural statistical error that is given by the shifts of the distribution of ϵ_r to the left and to the right,

taking into account the error of $\sqrt{N}$, where N is the number of counts for each bin. This is not surprising, as the upper and lower bounds describe the maximum total errors. The statistical errors, however, intrinsically project the real randomness of the island shape. Considering this last error for both measurements, we conclude that, although there is a difference between the two peak maximum values of ϵ_r, the difference is very small: while the peak of ϵ_r from the measurement in vacuum (a) could be shifted down to 1.81, it could be shifted up to 1.7 in the measurement in the electrolyte (b), thus only 0.11 difference between them.

In order to study further not only the effect of the experimental oxidation-reduction conditions chosen, but also the evolution of the island shape during growth, we created islands by performing ORCs between 0.06 V and 1.35 V and at 50 mV/s (see Fig. 2.9). We then obtained the distributions of ϵ_r of the adatom islands after 1, 6 and 7 ORCs (see Fig. 2.10), which we compared with the distribution of ϵ_r for the EC-STM measurement presented above in Fig. 2.6e, in which the potential was held at 1.35 V for 200 s.

The first we note is that all islands in Fig. 2.9(a-d) are dendritic, independently of the electrochemical treatment. The statistical distribution resulting from the potential hold experiment shows a larger ϵ_r value of 1.63 in comparison to the the $\epsilon_r = 1.57$ on ORC #1. The reason for this is that, at longer waiting times, more PE_{irr} atoms are created [65, 71]. However, even if we handle the same "waiting" time, the distributions show that the islands become more compact with increasing ORC number: note the shift between ORC #1 and ORC #6, but also the slight shift to smaller values from ORC #6 to ORC #7. Although these shifts fall within the statistical errors of the distributions, and hence they should be treated with caution, this trend is what we would expect according to our understanding on the atomic details underlying island growth, as we explain in the following.

We have concluded earlier that above 0.8 V the steps oxidize, and that there is a large driving force to form PtO_2-adatoms from the kinks. We have evidence that, in analogy to the PE_{irr} on the terrace, the oxide chains at the steps also push PtO_2 units up onto the upper terrace, thus becoming PtO_2-adatoms. It was observed in Ref. [25] that the transition from 2D to 3D island growth (ocurring between the 20th and the 30th ORC) results in a significant decrease in the growth exponent. This can only be explained by a pronounced decrease of the flux, which can only be due to a change in the roughening (growth) mechanism [109]. The flux has two contributions, the PE_{irr} atoms created on the terraces, and the PtO_2-adatoms formed by oxidizing the steps. The mechanism in which the latter takes place could be similar to the PE_{rev} and the PE_{irr} on a terrace: it starts with lifting PtO_2 units (PE_{rev} atoms) along the step and, once a critical stress along the step-row is reached, one unit per certain row length is pushed onto the upper terrace. While the terrace width decreases considerably as the growth transitions from 2D to 3D, becoming as small as 2 platinum distances [26], the step density increases to its maximum. Therefore, the decrease in the flux must be due to the change of these two contributions. However, as the roughening (growth) continues to at least up to 170 cycles and the terraces in the 3D mounts can not accommodate the oxide spokes, the dominating flux of PtO_2-adatoms during the late stages of growth must come from the steps. Furthermore, as the growth of the mounts occurrs predominantly in height, the PtO_2-adatom flux from the steps must go uphill.
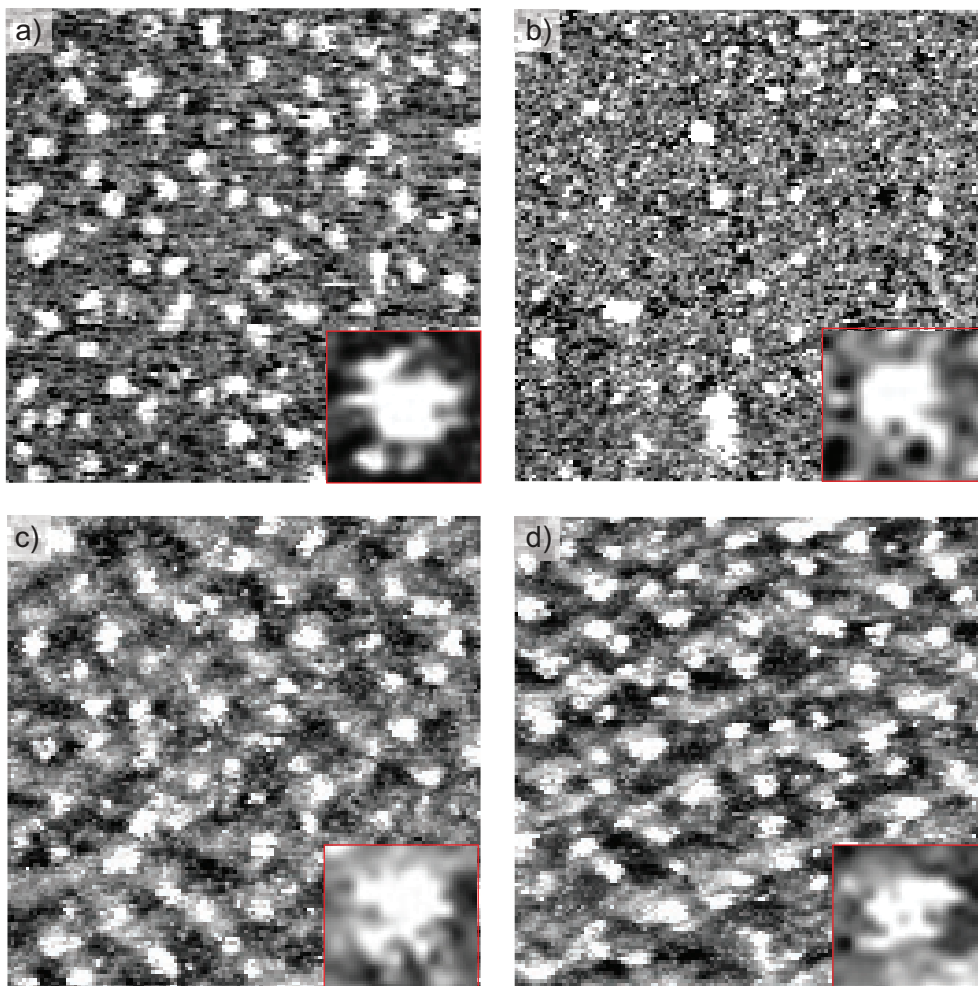
Figure 2.9: Degree of Dendritic Island Shape as Function of ORC-number. (a) As a reference, after holding the potential at 1.35 V for 200 s before reducing to 0.3 V with 25 mV/s. **(b)** After the first ORC between 0.06 V and 1.35 V. **(c)** After 6 ORCs. **(d)** After 7 ORCs. All ORCs are performed with a scan rate of 50 mV/s. All images are 80 x 80 nm^2. Larger scale images are provided in Appendix A.

Coming back to the explanation for the decrease of ϵ_r upon cycling, the uphill flux from the steps results in PtO$_2$-adatoms on the island. These PtO$_2$-adatoms (or Pt-adatoms, upon reduction), instead of nucleating, hop down the step and get incorporated to the island edge. This is because the Ehrlich-Schwoebel barrier vanishes for small terrace widths [83–85], like on the branches. Consequently, the "fjords" between the branches get filled, leading to more compact shapes. This "annealing" is repeated during each ORC and competes with the dendritic growth in the perpendicular direction of the step. If the filling of the fjords is faster than the dendritic growth, ϵ_r will decrease after each cycle, meaning that

the islands become more compact.

Finally, another cause for the decrease of ϵ_r upon cycling originates from the increase of the island perimeter upon growth. As this leads to longer steps with less kinks, the KESE becomes less relevant for the step-adatom diffusion along the island edge: the step-adatoms have more distance to diffuse along the step before finding a kink. This leads to an increase of the width of the branches at their base (see Fig. 2.7), and hence less dense branching, which results in a lower ϵ_r.
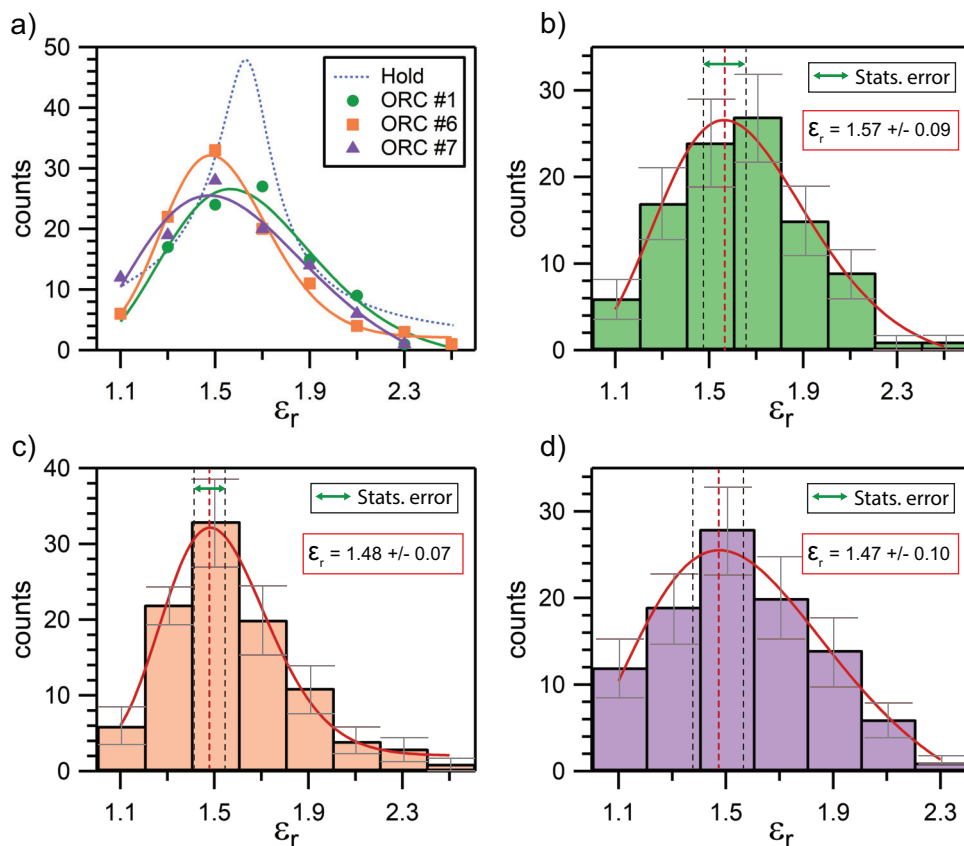
Figure 2.10: Evolution of the Statistical Distributions of ϵ_r upon Oxidation-Reduction Cycling.
(a) Comparison of the statistical distributions obtained from the measurement described before, in which the potential was held at 1.35 V for 200 s (blue dotted line), with the distributions obtained after 1, 6, and 7 ORCs, in green, orange and purple, respectively. The latter three distributions are also shown in **(b)**, **(c)**, and **(d)**, respectively, where we also provide a curve fit to highlight the peak maximum, error bars based on the statistical error at each bin, and a green arrow representing the shift of the peak maximum due to the statistical error.

2.6 Conclusions

In this work, we have studied with DFT both the stability and the mobility of two different adatom species, Pt-adatom and PtO_2-adatom, on Pt(111) by calculating their formation energies and diffusion rates at different electrode potentials, with the aim to get a better understanding on the nucleation of adatom islands upon oxidation-reduction cycling. Our results show that, although during the forward (anodic) scan the irreversible place-exchange that starts at 1.17 V leads to the creation of PtO_2-adatoms, nucleation into PtO_2-islands does not occurr. The reason for this is that the equilibrium concentration of PtO_2-adatoms reaches practically 1 ML at 0.94 V, and thus at these high potentials the complete surface prefers to be oxidized. Nucleation into PtO_2-adatom islands does not occur with ORCs even up to 1.35 V, as there are only 0.0245 ML PtO_2-adatoms created during the irreversible place-exchange, which is significantly lower than 1 ML. During the subsequent cathodic scan, the equilibrium concentration of PtO_2-adatoms decreases exponentially with the potential and, below 0.94 V, it becomes lower than the actual PtO_2-adatom concentration of 0.0245 ML. Therefore, nucleation becomes thermodynamically favorable. However, the PtO_2-adatoms are "trapped" in between the oxide rows that are created during the reversible part of the oxidation. As these rows are lifted almost 1 ML high from the surface, nucleation is hindered by too low mobility. In addition, PtO_2-adatoms diffuse very slow, 0.28 jumps/s, and hence they do not have enough time to find each other before they reduce to Pt-adatoms. Pt-adatoms diffuse much faster (10^8 jumps/s) and therefore, once they form at 0.59 V, they rapidly find each other and nucleate into adatom islands, as also their actual concentration is much higher than their equilibrium concentration. These results match the observations from Wakisaka et al. [24], who reported that the adatom islands do not form until the potential is decreased to 0.49 V.

As not only the electrocatalytic activity of platinum, but also its degradation is highly dependent on the concentration of the different surface sites, we also analyzed the shape of the islands formed from vacuum STM and EC-STM images. We quantified the island perimeter and the area to finally determine the island compactness and a factor that describes the additional step length with respect to a circular island. Contrary to what was suggested in the literature, the islands formed upon oxidation-reduction are dendritic, and not hexagonal, which matches the observations from MBE experiments in vacuum. Finally, we studied the shape evolution during the island growth upon oxidation-reduction cycling. Although within the statistical error bars of the distributions, we have indications that the dendritic islands change towards more compact shapes with increasing cycle number. This trend matches our insight into the atomic picture during growth and can be explained by: (1) the uphill flux originating from the island edges, and the downhill interlayer diffusion of adatoms that end up filling the "fjords" between the island branches; and (2) the longer step length for larger islands on which a step-adatom can diffuse without encountering a kink, leading to less branching and thus less dendritic growth.

References

[1] F. Calle-Vallejo, J. Tymoczko, V. Colic, Q. Huy Vu, M. D. Pohl, K. Morgenstern, D. Loffreda, P. Sautet, W. Schuhmann, and A. S. Bandarenka, *Science*, **350**, 185 (2015).

[2] T. Zambelli, J. Wintterlin, J. Trost and G. Ertl, *Science*, **273**, 1688 (1996).

[3] K. J. P. Schouten, E. Pérez Gallent and M. T. M. Koper, *ACS Catal.*, **3**, 1292 (2013).

[4] A. Kuzume, E. Herrero, and J. M. Feliu, *J. Electroanal. Chem.*, **599**, 333 (2007).

[5] M.D. Maciá, J.M. Campiña, E. Herrero, and J.M. Feliu, *J. Electroanal. Chem.*, **564**, 141 (2004).

[6] F. Xiao, Y. Wang, Z. Wu, G. Chen, F. Yang, S. Zhu, K. Siddharth, Z. Kong, A. Lu, J. Li, C. Zhong, Z. Zhou, and M. Shao, *Adv. Mater.*, **33**, 2006292 (2021).

[7] J. K. Nørskov, J. Rossmeisl, A. Logadottir, L. Lindqvist, J. R. Kitchin, T. Bligaard, and H. Jónsson, *J. Phys. Chem. B*, **108**, 17886 (2004).

[8] X. Tian, P. Zhao, and W. Sheng, *Adv. Mater.*, **31**, 1808066 (2019).

[9] S. Wang, A. Lu, and C. Zhong, *Nano Convergence*, **8**, 4 (2021).

[10] R. L. Borup, A. Kusoglu, K. C. Neyerlin, R. Mukundan, R. K. Ahluwalia, D. A. Cullen, K. L. More, A. Z. Weber, and D. J. Myers, *Curr. Opin. Electrochem.*, **21**, 192 (2020).

[11] A. A. Topalov, S. Cherevko, A. R. Zeradjanin, J. C. Meier, I. Katsounaros, and K. J. J. Mayrhofer, *Chem. Sci.*, **5**, 631 (2014).

[12] D. J. S. Sandbeck, O. Brummel, K. J. J. Mayrhofer, J. Libuda, I. Katsounaros, and S. Cherevko, *Chem. Phys. Chem.*, **20**, 2997 (2019).

[13] D. J. S. Sandbeck, M. Inaba, J. Quinson, J. Bucher, A. Zana, M. Arenz, and S. Cherevko, *ACS Appl. Mater. Interfaces*, **12**, 25718 (2020).

[14] F. T. Wagner and P. N. Ross, *Surf. Sci*, **160**, 305 (1985).

[15] H. You and Z. Nagy, *Physica B: Condens. Matter*, **198**, 187 (1994).

[16] Z. Nagy and H. You, *Electrochim. Acta*, **47**, 3037 (2002).

[17] M. Ruge, J. Drnec, B. Rahn, F. Reikowski, D. A. Harrington, F. Carlà, R. Felici, J. Stettner, and O. M. Magnussen, *J. Am. Chem. Soc.*, **139**, 4532 (2017).

[18] N. Breuer, A. M. Funtikov, U. Stimming, and R. Vogel, *Surf. Sci.*, **335**, 145 (1995).

[19] N. Furuya and M. Shibata, *J. Electroanal. Chem.*, **467**, 85 (1999).

[20] S. Sugawara and K. Itaya, *J. Chem. Soc.*, **85**, 1351 (1989).

[21] K. Itaya, S. Sugawara, K. Sashikata, and N. Furuya, *J. Vac. Sci. Technol. A*, **8**, 515 (1990).

[22] K. Sashikata, N. Furuya, and K. Itaya, *J. Vac. Sci. Technol. B: Microelectron. Process. Phenom.*, **9**, 457 (1991).

[23] Y. Sugawara, M. Sasaki, I. Muto, and N. Hara, *ECS Trans.*, **64**, 81 (2014).

[24] M. Wakisaka, S. Asizawa, H. Uchida, and M. Watanabe, *Phys. Chem. Chem. Phys.*, **12**, 4184 (2010).

[25] L. Jacobse, Y. F. Huang, M. T. M. Koper, and M. J. Rost, *Nat. Mater.*, **17**, 277 (2018).

[26] L. Jacobse, M. J. Rost, and M. T. M. Koper, *ACS Cent. Sci.*, **5**, 1920 (2019).

[27] G. Wulff, *Z. Krystallogr.*, **34**, 449 (1901).

[28] C. Herring, *Phys. Rev.*, **82**, 87 (1951).

[29] J. Ikonomov, K. Starbova, H. Ibach, and M. Giesen, *Phys. Rev. B*, **75**, 245411 (2007).

[30] T. Michely, M. Hohage, M. Bott, and G. Comsa, *Phys. Rev. Lett.*, **70**, 3943 (1993).

[31] R. F. Sekerka, *Cryst. Res. Technol.*, **740**, 291 (2005).

[32] W. W. Mullins and R. F. Sekerka, *J. Appl. Phys.*, **34**, 323 (1963).

[33] S. Ogura, K. Fukutani, M. Matsumoto, T. Okano, M. Okada, and T. Kawamura, *Phys. Rev. B*, **73**, 125442 (2006).

[34] R. Q. Hwang, J. Schröder, C. Günther, and R. J. Behm, *Phys. Rev. Lett.*, **67**, 3279 (1991).

[35] Z. Zhang and M. Lagally, *Science*, **276**, 377 (1997).

[36] Z. Zhang, X. Chen, and M. Lagally, *Phys. Rev. Lett.*, **73**, 1829 (1994).

[37] T. Michely and J. Krug, *Islands, Mounds and Atoms*, Springer, Amsterdam (2004).

[38] M. Bott, T. Michely, and G. Comsa, *Surf. Sci.*, **272**, 161 (1992).

[39] M. Hohage, M. Bott, M. Morgenstern, Z. Zhang, T. Michely, and G. Comsa, *Phys. Rev. Lett.*, **76**, 2366 (1996).

[40] T. Maagaard, PhD thesis (2018), Department of Physics, Danmarks Tekniske Universitet (DTU), Denmark, <https://orbit.dtu.dk/en/publications/combining-uhv-stm-and-electrochemistry-for-surface-studies-of-mod>.

[41] J. Drnec, M. Ruge, F. Reikowski, B. Rahn, F. Carlà, R. Felici, J. Stettner, O. M. Magnussen, and D. A. Harrington, *Electrochim. Acta*, **224**, 220 (2017).

[42] M. J. Rost, L. Crama, P. Schakel, E. van Tol, G. B. E. M. van Velzen-Williams, C. F. Overgauw, H. ter Horst, H. Dekker, B. Okhuijsen, M. Seynen, A. Vijftigschild, P. Han, A. J. Katan, K. Schoots, R. Schumm, and W. van Loo, *Rev. Sci. Instrum.*, **76**, 053710 (2005).

[43] Y. I. Yanson, F. Schenkel, and M. J. Rost, *Rev. Sci. Instrum.*, **84**, 023702 (2013).

[44] M. J. Rost, in *Encyclopedia of Interfacial Chemistry*, 1st ed., K. Wandelt, p.180, Elsevier, Amsterdam (2018).

[45] M. J. Rost, G. J. C. van Baarle, A. J. Katan, W. M. van Spengen, P. Schakel, W. A. van Loo, T. H. Oosterkamp, and J. W. M. Frenken, *Asian J. Control*, **11**, 110 (2009).

[46] G. Kresse and J. Furthmüller, *Phys. Rev. B.*, **54**, 169 (1996).

[47] G. Kresse and J. Furthmüller, *Comput. Mater. Sci.*, **6**, 15 (1996).

[48] G. Kresse and J. Hafner, *Phys. Rev. B.*, **47**, 558, (1993).

[49] J. P. Perdew, J. A. Chevary, S. H. Vosko, K. A. Jackson, M. R. Pederson, D. J. Singh, and C. Fiolhais, *Phys. Rev. B.*, **46**, 6671 (1992).

[50] Kittel, C., *Introduction to Solid State Physics*, 7th edn., Wiley, New York (2008).

[51] H. J. Monkhorst and J. D. Pack, *Phys. Rev. B.*, **13**, 5188 (1976).

[52] L. Bengtsson, *Phys. Rev. B.*, **59**, 12302 (1999).

[53] I. T. McCrum, M. A. Hickner, and M. J. Janik, *Langmuir*, **33**, 7043 (2017).

[54] D. Fantauzzi, J. Bandlow, L. Sabo, J. E. Mueller, A. C. T. van Duin, and T. Jacob, *Phys. Chem. Chem. Phys.*, **16**, 23118 (2014).

[55] G. Henkelman, B. P. Uberuaga, and H. Jónsson, *J. Chem. Phys.*, **113**, 9901 (2000).

[56] J. Clavilier, K. El Achi, and A. Rodes, *J. Electroanal. Chem.*, **272**, 253 (1989).

[57] A. Rodes, K. El Achi, M. A. Zamakhchari, and J. Clavilier, *J. Electroanal. Chem.*, **284**, 245 (1990).

[58] X. Chen, I. T. McCrum, K. A. Schwarz, M. J. Janik, and M. T. M. Koper, *Angew. Chem. Int. Ed.*, **56**, 15025 (2017).

[59] M. J. T. C. van der Niet, N. Garcia-Araez, J. Hernández, J. M. Feliu, and M. T. M. Koper, *Catal. Today*, **202**, 105 (2013).

[60] R. Rizo, J. Fernández-Vidal, L. J. Hardwick, G. A. Attard, F. J. Vidal-Iglesias, V. Climent, E. Herrero, and J. M. Feliu, *Nat. Commun.*, **13**, 2550 (2022).

[61] A. Björling, E. Ahlberg, and J. M. Feliu, *Electrochem. Commun.*, **12**, 359 (2010).

[62] A. Björling, E. Herrero, and J. M. Feliu, *J. Phys. Chem.*, **115**, 15509 (2011).

[63] F. T. Wagner and P. N. Ross, *J. Electroanal. Chem.*, **250**, 301 (1998).

[64] H. Tanaka, S. Sugawara, K. Shinohara, T. Ueno, S. Suzuki, N. Hoshi, and M. Nakamura, *Electrocatalysis*, **6**, 295 (2015).

[65] M. J. Rost, L. Jacobse, and M. T. M. Koper, *Angew. Chem. Int. Ed.*, **62**, e202216376 (2023).

[66] M. A. H. Lanyon and B. M. W. Trapnell, *Proc. R. Soc. A.*, **227**, 387 (1955).

[67] A. K. N. Reddy, M. A. Genshaw, and J. O. Bockris, *J. Chem. Phys.*, **48**, 671 (1968).

[68] K. J. Vetter and J. W. Schultze, *J. Electroanal. Chem.*, **34**, 141 (1972).

[69] B. V. Tilak, B. E. Conway, and H. Angerstein-Kozlowska, *J. Electroanal. Chem.*, **48**, 1 (1973).

[70] G. Jerkiewicz, G. Vatankhah, J. Lessard, M. P. Soriaga, and Y. Park, *Electrochim. Acta*, **49**, 1451 (2004).

[71] L. Jacobse, V. Vonk, I. T. McCrum, C. Seitz, M. T. M. Koper, M. J. Rost, and A. Stierle, *Electrochim. Acta*, **407**, 139881 (2022).

[72] M. Ruge, J. Drnec, B. Rahn, F. Reikowski, D. A. Harrington, F. Carlà, R. Felici, J. Stettner, and O. M. Magnussen, *J. Electrochem. Soc.*, **164**, H608 (2017).

[73] A. Björling and J. M. Feliu, *J. Electroanal. Chem.*, **662**, 17 (2011).

[74] A. M. Gómez-Marín and J. M. Feliu, *Electrochem. Acta.*, **82**, 558 (2012).

[75] A. M. Gómez-Marín and J. M. Feliu, *Electrochim. Acta.*, **104**, 367 (2013).

[76] A. M. Gómez-Marín, J. Clavilier, and J. M. Feliu, *J. Electroanal. Chem.*, **688**, 360 (2013).

[77] J. Drnec, M. Ruge, F. Reikowski, B. Rahn, F. Carlà, R. Felici, J. Stettner, O. M. Magnussen, and D. A. Harrington, *Electrochem. Commun.*, **84**, 50 (2017).

[78] H. You, D. J. Zurawski, Z. Nagy, and R. M. Yonco, *J. Chem. Phys.*, **100**, 4699 (1994).

[79] Y. Liu, A. Barbour, V. Komanicky, and H. You, *J. Phys. Chem. C*, **120**, 16174 (2016).

[80] M. J. Rost, L. Jacobse, and M. T. M. Koper, *Nat. Commun.*, **10**, 5233 (2019).

[81] G. Ehrlich and F. G. Hudda, *J. Chem. Phys.*, **44**, 1039 (1966).

[82] R. L. Schwoebel and E. J. Shipsey, *J. Appl. Phys.*, **37**, 3682 (1966).

[83] M. Giesen, G. S. Icking-Konert, and H. Ibach, *Phys. Rev. Lett.*, **82**, 3101 (1999).

[84] M. Giesen and H. Ibach, *Surf. Sci. Lett.*, **464**, L697 (2000).

[85] K. Morgenstern, G. Rosenfeld, G. Comsa, M. R. Sørensen, B. Hammer, E. Lægsgaard, and F. Besenbacher, *Phys. Rev. B*, **63**, 045412 (2001).

[86] M. A. van Spronsen, J. W. M. Frenken, and I. M. N. Groot, *Nat. Commun.*, **8**, 429 (2017).

[87] S. Hanselman, I. T. McCrum, M. J. Rost, and M. T. M. Koper, *Phys. Chem. Chem. Phys.*, **22**, 10634 (2020).

[88] H. Ibach, *Physics of Surfaces and Interfaces*, Springer, Amsterdam (2006).

[89] J. G. Wang, W. X. Li, M. Borg, J. Gustafson, A. Mikkelsen, T. M. Pedersen, E. Lundgren, J. Weissenrieder, J. Klikovits, M. Schmid, B. Hammer, and J. N. Andersen, *Phys. Rev. Let*, **95**, 256102 (2005).

[90] J. Bandlow, P. Kaghazchi, and T. Jacob, *Phys. Rev. B*, **83**, 174107 (2011).

[91] J. Lapujoulade, *Surf. Sci. Rep.*, **20**, 191 (1994).

[92] M. J. Rost, S. B. van Albada, and J. W. M. Frenken, *Surf. Sci.*, **518**, 21 (2002).

[93] M. J. Rost, S. B. van Albada, and J. W. M. Frenken, *Europhys. Lett*, **59**, 559 (2002).

[94] M. J. Rost, S. B. van Albada, and J. W. M. Frenken, *Surf. Sci.*, **515**, 344 (2002).

[95] M. J. Rost, S. B. van Albada, and J. W. M. Frenken, *Surf. Sci.*, **547**, 71 (2003).

[96] V. Climent, G. A. Attard, and J. M. Feliu, *J. Electroanal. Chem.*, **532**, 67 (2002).

[97] K. Ojha, N. Arulmozhi, D. Aranzales, and M. T. M. Koper, *Angew. Chem.*, **130**, 721 (2020).

[98] M. Bott, M. Hohage, M. Morgenstern, T. Michely, and G. Comsa, *Phys. Rev. Lett.*, **76**, 1304 (1996).

[99] K. Kyuno and G. Ehrlich, *Surf. Sci.*, **437**, 29 (1999).

[100] P. Stoltze, *J. Phys.: Condens. Matter.*, **6**, 9495 (1994).

[101] K. Morgenstern, G. Rosenfeld, E. Lægsgaard, F. Besenbacher, and G. Comsa, *Phys. Rev. Lett.*, **80**, 556 (1998).

[102] K. Morgenstern, G. Rosenfeld, and G. Comsa, *Phys. Rev. Lett.*, **76**, 2113 (1996).

[103] G. Rosenfeld, K. Morgenstern, M. Esser, and G. Comsa, *Appl. Phys. A*, **69**, 489 (1999).

[104] O. Pierre-Louis, M. R. D'Orsogna, and T. L. Einstein, *Phys. Rev. Lett.*, **82**, 3661 (1999).

[105] C. Misbah, O. Pierre-Louis, and Y. Saito, *Rev. Mod. Phys.*, **82**, 981 (2010).

[106] M. J. Rost, *Phys. Rev. Lett.*, **99**, 266101 (2007).

[107] B. Lim, M. Jiang, P. H. C. Camargo, E. C. Cho, J. Tao, X. Lu, Y. Zhu, and Y. Xia, *Science*, **324**, 1302 (2009).

[108] G. Zhang, S. Sun, M. Cai, Y. Zhang, R. Li, and X. Sun, *Sci. Rep.*, **3**, 1526 (2013).

[109] P. Meakin, *Fractals, Scaling and Growth Far from Equilibrium*, Cambridge University Press, Cambridge (1998).

3 Step Bunching Instability and its Effects in Electrochemistry: Pt(111) and its Vicinal Surfaces

Abstract

The atomic-scale surface structure plays a major role in the electrochemical behavior of a catalyst. The electrocatalytic activity towards many relevant reactions, such as the Oxygen Reduction Reaction on platinum, exhibits a linear dependency with the number of steps until this linear scaling breaks down at high step densities. Here we show, using Pt(111)-vicinal surfaces and *in-situ* Electrochemical Scanning Tunneling Microscopy (EC-STM), that this anomalous behavior at high step densities has a structural origin, and is attributed to the bunching of closely spaced steps. While Pt(554) presents parallel single steps and terrace widths that correspond to its nominal, expected value, most steps on Pt(553) are bunched. Our findings challenge the common assumption in electrochemistry that all stepped surfaces are composed by homogeneously spaced steps of mono-atomic height and can successfully explain the anomalous trends documented in the literature linking step density to both activity and potential of zero total charge.

3.1   Introduction

Stepped platinum single crystals are widely used in electrochemistry to study the unique reactivity of step sites. Low-Energy Electron Diffraction, He-beam diffraction, and STM studies in ultra-high vacuum (UHV) confirmed that Pt(111)-vicinal surfaces such as Pt(997) prepared by sputtering and annealing are stable at moderate temperatures as long as oxygen is not present whilst the sample is hot [1–4]. Unfortunately, there is scarce work on the atomic-scale characterization of stepped surfaces when prepared by flame-annealing (in air) and cooled down in a reducing atmosphere, which is the typical methodology followed in electrochemistry [5]. Herrero et al. showed that Pt(10 10 9) and Pt(11 10 10) (both with steps along a direction equivalent to [110], but with the former having {111}, and the later having {100} microfacets) present their nominal structures if an Ar + H_2 mixture is used while cooling down the samples [6]. As a result, it is often assumed in single-crystal electrochemistry studies that all stepped surfaces are composed of parallel running monoatomic-height steps.

   This assumption, however, is inconsistent with many experimental observations that show a dissimilar relation to the density of step (or step-related) sites among different Pt(111)-vicinal surfaces. For example, the potential at which the total charge is zero (E_{pztc}) decreases linearly with the step density, as expected, but only until a certain critical value, from on which it deviates significantly [7]. Similarly, the linear scaling between the Oxygen Reduction Reaction (ORR) activity and the step density breaks down for stepped surfaces with very small terraces [8, 9]. This phenomenon suggests a structural difference of the steps depending on the terrace width, despite the lack of supporting evidence in the literature.

   In this article we offer an explanation for this anomalous behavior. Using EC-STM we show that Pt(554) exhibits exclusively single, monoatomic-height steps, while a stepped surface with theoretically narrow terraces, such as Pt(553), shows mainly double-height (bunched) steps and terraces with twice the nominal width. Based on this observation, we quantitatively show, on the example of the E_{pztc} and the ORR activity, that step bunching can successfully explain the anomalous behavior of surfaces with high step density.

3.2   Experimental

Electrochemistry. We recorded the cyclic voltammograms in a glass cell that we cleaned first with an acidic potassium permanganate solution and then with diluted piranha, before finally boiling it five times in ultrapure water (> 18.2 MΩ cm, Millipore Milli-Q). For the measurements, we used a reversible hydrogen electrode (RHE) as the reference and a Pt wire (MaTeck, Germany) as the counter electrode. Our working electrode was a high quality (99.999 % purity and polished < 0.1°) platinum single crystal, either a Pt(111) (Surface Preparation Laboratory, The Netherlands) or a (111)-vicinal surface with (111) steps (MaTeck, Germany). The latter can be described with the notation Pt(s)[n(111) x (111)], where n is the number of atomic rows on a single terrace. Before the measurements, we etched the platinum sample electrochemically (125 cycles at 50 Hz, ± 2 V versus Pt) in an

acidified 2.5 M CaCl$_2$ solution. Subsequently, we flame annealed it (3 min at $\approx$ 1250 K) and cooled it down in a 1:4 H$_2$/Ar mixture. We repeated this treatment three times, with the last annealing step at a slightly lower temperature ($\approx$ 50 K lower) in order to deplete the surface from contamination coming from the bulk. We performed all the cyclic voltammograms in an Ar-purged 0.1 M HClO$_4$ solution (Merck Suprapur), using a potentiostat from Bio-Logic (VSP-300).

Electrochemical Scanning Tunneling Microscopy. We recorded the STM images with a home-build EC-STM [10, 11]. We used an RHE and a Pt coil as reference and counter electrodes, respectively, while the working electrode was either Pt(554) or Pt(553) with which we also recorded the cyclic voltammograms. We made the STM tips by electrochemically etching of a Pt$_{90}$Ir$_{10}$ wire (Goodfellow), and we coated them with electrophoretic paint (Clearclad HSR) and polyethylene to minimize the faradaic contributions in the tunneling current. Before every measurement, we cleaned all the glassware and pipes following the procedure described in Ref. [12] and we de-aerated the electrolyte (0.1 M HClO$_4$) with N$_2$ for at least 3 hours.

3.3   Thermodynamics of Stepped Surfaces

At thermodynamic equilibrium, the surface morphology always conforms to the one with the lowest free energy. For a high Miller-index surface, the surface free energy at a temperature T is given by [13]:

$$f_{total}(T) = f_{terr}(T) + f_{step}(T)\frac{1}{L} + B_{step}(T)\frac{1}{aL^3} \tag{3.1}$$

where f_{terr} corresponds to the free energy of the terraces and f_{step} is the free energy of the steps, which is divided by the terrace width (L) in order to account for the step density. The third term describes the interactions between steps, where B_{step} is an interaction coefficient and a the unit step length: a = 2.78 Å.

The temperature dependence is specially important for f_{step}, as all steps are rough at any $T > 0$ K: thermally-activated kinks form and enable the steps to meander, thereby increasing their entropy and lowering their free energy f_{step} according to [14]:

$$f_{step}(T) = f_{step}^0 - \frac{2k_BT}{a}exp(\frac{-f_{kink}^0}{k_BT}) \tag{3.2}$$

where f_{step}^0 and f_{kink}^0 are the formation energies of a unit step length and a kink site, respectively, while k_B is the Boltzmann's constant. Note that at a high enough T the exponential term in equation 3.2 becomes practically equal to 1, which can lead to $f_{step} < 0$, i.e. the surface can form steps spontaneously, describing the 3D roughening transition [15].

Step meandering is, however, hindered by the step-step interaction, which has three different components. The first one is an entropic repulsion originating from the geometric confinement of a step in between its two neighbors [16, 17]. The second one is an electrostatic interaction between electric dipoles that form at step edges due to the Smoluchowski effect [18, 19], which goes hand-in-hand with an elastic interaction [20–23]. Unlike the

entropic repulsion, the electrostatic and elastic interactions are always repulsive for neighboring steps of the same type (ascending or descending), while they can be either repulsive or attractive for opposite type of steps, depending on the strength of the dipole moment parallel to the surface [14]. In any case, all three contributions to the step-step interaction usually decay with L^{-2} [19, 24]. Scaling this factor to units of energy/area, we obtain the L^{-3} dependency that is reflected in the third term of equation 3.1.

In the next section we first present our results on the characterization of Pt(554) and Pt(553), before we discuss the origin of the step bunching instability based on the thermodynamic description given above.

3.4   Surface Characterization

Figure 3.1 (**a** and **b**) shows 3D rendered EC-STM images of a Pt(554) surface and a Pt(553) surface recorded at constant sample and tip potentials, $U_s = 0.1$ V and $U_t = 0.15$ V, respectively, which we processed on the terrace planes to bring out the natural tilt of each sample (see Appendix B for details). When comparing both images, one realizes that the average separation between the steps, the brighter parallel lines, is similar on both surfaces, which is supported by the corresponding height lines shown in Fig. 3.1 (**c** and **d**): the terraces selected on Pt(554) and Pt(553) measure 23.1 Å and 23.9 Å in width, respectively. This is surprising, as Pt(553) naturally has double the step density of Pt(554). In fact, the nominal terrace widths are 22.4 Å and 10.4 Å, respectively, as given by the ball model equation:

$$L = \frac{\sqrt{3}}{2} d (n-1) + \frac{\sqrt{3}}{3} d \tag{3.3}$$

where d is the distance between two close-packed platinum atoms and n is the number of atom rows in a single terrace (n = 10 for Pt(554) and n = 5 for Pt(553)). As the steps can not simply vanish, because the natural surface orientation must be always preserved, the only possible explanation for the doubling of the terrace width on Pt(553) is that the steps bunch together in pairs, as shown in Fig. 3.2. Evidence for this is the step height of 4.48 Å measured in Fig. 3.1d, which is twice the theoretical (111) step height of 2.27 Å.

To quantify our observation statistically, we traced over 50 randomly-chosen height lines from which we measured the step heights and terrace widths for both Pt(554) and Pt(553), analyzing several STM images that were recorded in different experiments (see Appendix B). Figure 3.3a shows the resulting terrace width distribution for Pt(554). Its Gaussian shape indicates the existence of a repulsive interaction between the closely spaced steps, as opposed to an asymmetric peak that would be characteristic for freely fluctuating steps [13, 16]. The width of the distribution, often defined as its standard deviation (σ), depends on the interplay between f_{step} and B_{step}: a lower B_{step}, lower f_{kink}^0, or a higher T results in a broader peak, as it costs less energy for the steps to wander further away from the midway position between their neighbors. From the Gaussian fit in red, we obtain $\sigma = 4.2$ Å, which is higher than the $\sigma = 2.9$ Å reported for Pt(997) in vacuum [4]. This is what we would expect, as the terraces on Pt(554) are one atom row wider than on Pt(997), resulting in a lower step-step repulsive interaction. However, (part of) this difference might be also attributed to the screening of the dipole by the electrolyte. The center of the Gaussian distribution is
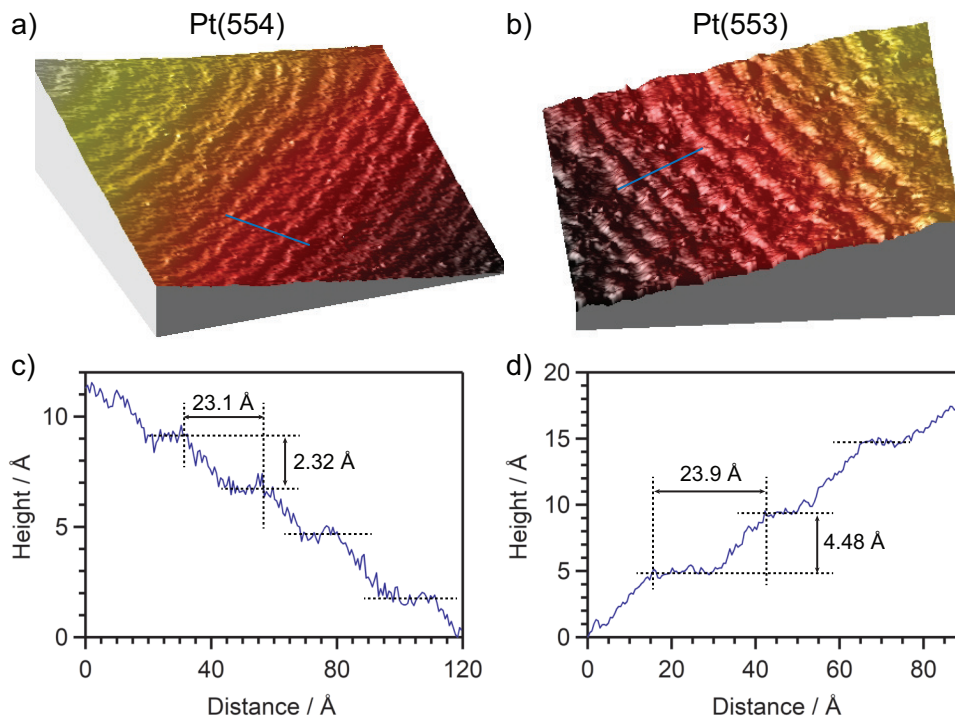
Figure 3.1: EC-STM Measurements of Pt(111)-Vicinal Surfaces. 3D rendered EC-STM images of **(a)** Pt(554) and **(b)** Pt(553), recorded in 0.1 M HClO$_4$ with U_s = 0.1 V and U_t = 0.15 V. Both images are 48 x 48 nm^2. The blue lines crossing the steps on Pt(554) and Pt(553) indicate the positions of the corresponding height lines shown in **(c)** and **(d)**. Note that the step height on Pt(553) is twice the one on Pt(554) and that both surfaces show an almost equal terrace width, although it should be theoretically 46 % smaller on Pt(553).
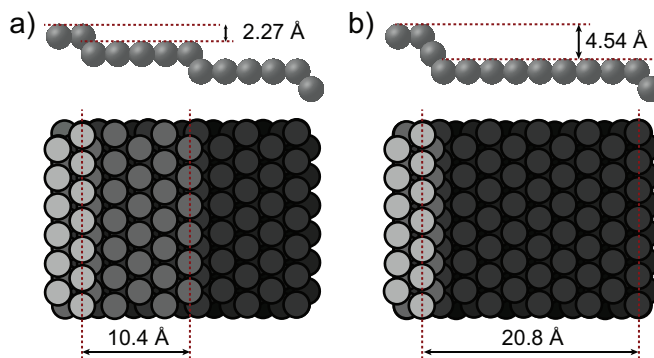

Figure 3.2: Ball Model of a Pt(553) Surface: (a) with single steps, **(b)** with double, bunched steps.

located at 21.9±0.9 Å, which agrees with the theoretical terrace width of 22.4 Å. Moreover, Fig. 3.3b exhibits only one peak in the distribution indicating that the steps on Pt(554) have mono-atomic height.

In contrast, the terrace width distribution on Pt(553), shown in Fig. 3.3c, reveals not only one but three peaks, centered at 11.3±0.5 Å, 20.6±0.5 Å, and 30±1 Å. These peaks correspond to terraces with nominal, double, and triple terrace widths, respectively, thus pointing to the presence of double and triple steps. This again is supported by the step height distribution in Fig. 3.3d, which shows also three different peaks, centered at around 2.25 Å (monoatomic step-height), 4.50 Å (double step-height), and 6.75 Å (triple step-height).
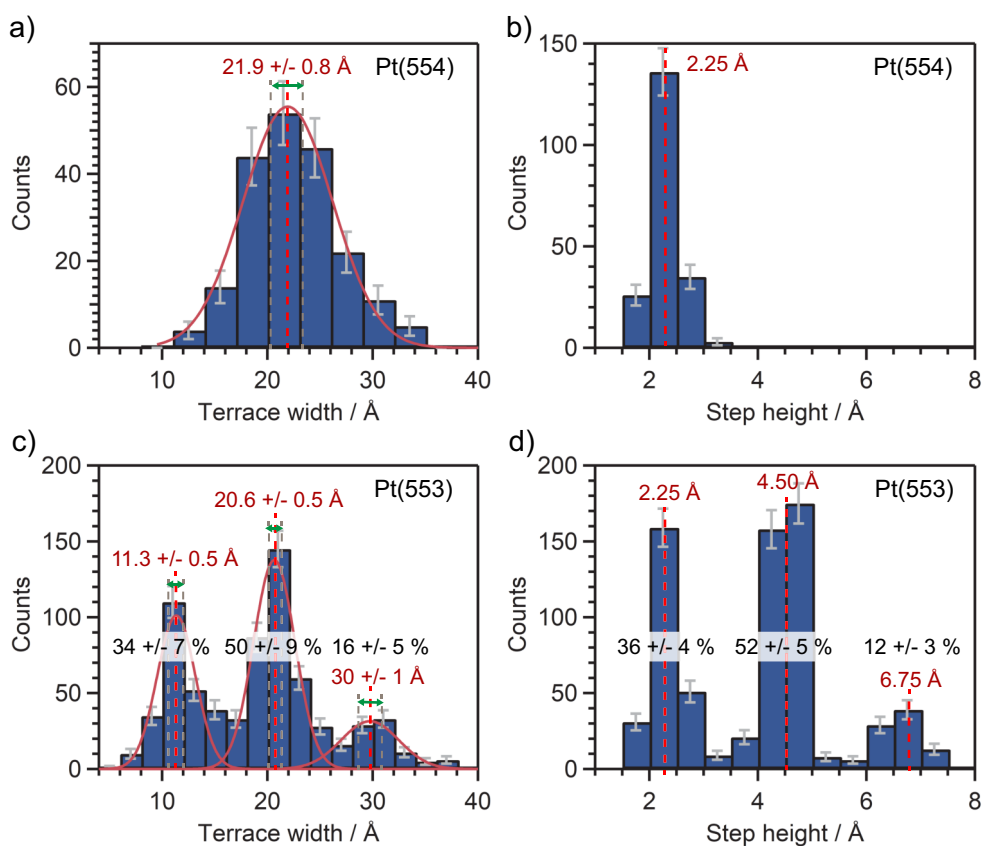

Figure 3.3: Statistical Analysis of the Surface Structure. **(a)** and **(b)** show the terrace width and step-height distributions of Pt(554), while **(c)** and **(d)** show the ones of Pt(553). The values in red and the red dashed lines indicate the center of each peak. For **(a)** and **(c)**, we obtained these values from Gaussian fits, with which we deconvoluted the peaks in the case of Pt(553). The statistical errors shown with gray error bars on each bin lead to uncertainties on the center values (green arrows) as well as on the percentages of single, double, and triple steps, which are reported in black on top of the corresponding peak.

From the percentages indicated on each peak in Fig. 3.3c and Fig. 3.3d, we extracted the corresponding averaged percentages of single (35±4 %), double (51±5 %), and triple (14±3 %) steps on Pt(553). We conclude that, while Pt(554) shows exclusively single steps and a terrace width around its nominal value, more than 65% of the steps on Pt(553) are bunched.

3.5   Origin of the Step Bunching Instability

Whether a vicinal surface undergoes step bunching depends on the delicate balance between f_{step} and B_{step}, which may result in a lower total free energy f_{total} for the bunched configuration. Figure 3.4a shows f_{total} with and without the repulsive step-step interaction, calculated with equations 3.1 and 3.2 and plotted versus the terrace width. One can observe that the dependence of f_{total} on the terrace width is mainly given by f_{step}/L up to narrow terraces (n = 8), below which the step-step interaction starts to play an increasingly significant role.

The surface configuration with double steps does not only have terraces with twice of the nominal terrace width, but also a different f_{step} and B_{step} compared to single steps, resulting in a different f_{total}. Figure 3.4b shows the energy ratio between a surface with double steps and one with single steps calculated at $T = 1300$ K, which is around 100 K below the maximum temperature reached during our flame-annealing. As surface diffusion drops exponentially with temperature, we estimate that upon further temperature decrease during the cooling down the step configuration becomes *frozen*. As an approximation, we also assumed for this calculation that the formation and kink energies of a double step ($f^0_{double step}$ and $f^0_{double kink}$, respectively) are exactly two times f^0_{step} and f^0_{kink} [27]. Moreover, we derived that the step-step interaction of double steps ($B_{double step}$) is 1.34 times larger than the one of single steps, see Appendix B, where we also show the temperature dependency of the energy ratio.

Figure 3.4b shows that, for our case, stepped surfaces with a terrace width larger than 8 atomic rows are expected to be stable, while those with equal or narrower terraces decrease the total free energy by the formation of step bunches. This is due to the lowering of the step-step repulsion when doubling the terrace width, as not only the step-step interaction term scales with L^{-3} (while the second term in equation 3.1 goes with L^{-1}) but also because $B_{double steps} < 2 B_{step}$ [13, 28]. Although this result is only indicative, as we used some assumptions and values from vacuum studies, it explains why Pt(554) has single steps while Pt(553) mainly has double steps. Moreover, step bunching could also elucidate why, according to Surface X-Ray Diffraction studies, flame-annealed Pt(311) and Pt(331) surfaces do not present their expected, nominal structure [29, 30].
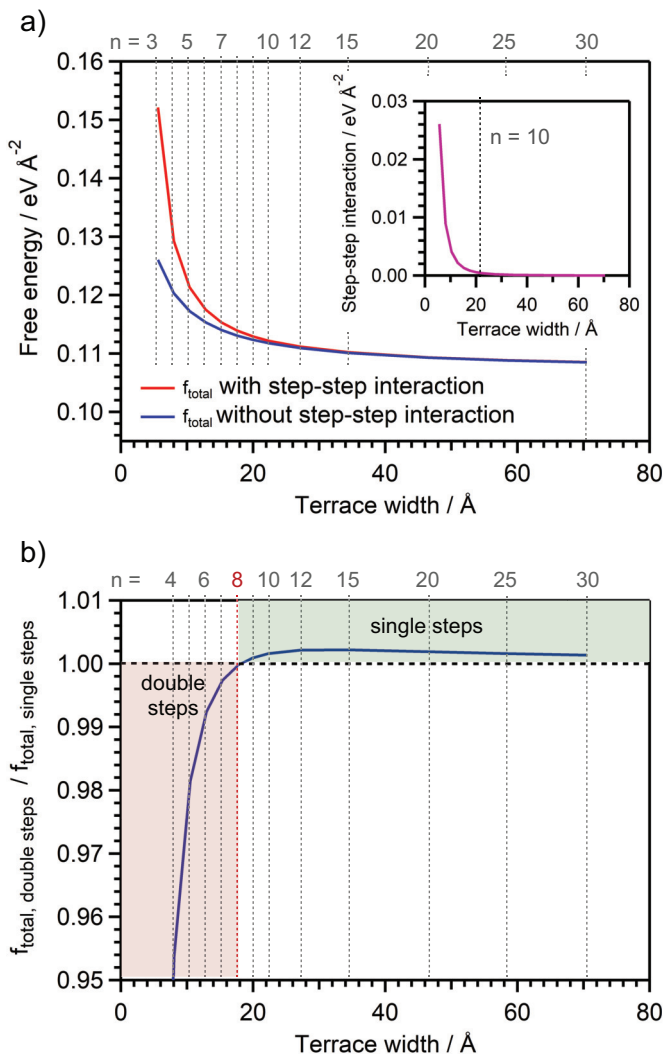
Figure 3.4: Thermodynamics of Step Bunching. (a) f_{total} with step-step interaction (red), f_{total} without step-step interaction (blue), and step-step interaction (inset, in purple) versus the terrace width for $T = 1300$ K. For the calculations, we used equations 3.1 and 3.2, with $f_{terr} = 1.07$ eV Å^{-2} from Ref. [25] and the values of $f_{step}^0 = 0.120$ eV Å^{-1} and $f_{kink}^0 = 0.206$ eV from Ref. [26]. We extracted the step interaction parameter $B_{step} = 12.76$ eV Å^2 from the one reported in Ref. [25], which we extrapolated to match with our temperature (see Appendix B). **(b)** Surface free energy ratio between configurations with double and single steps. To calculate the surface free energy for the double steps we reasonably approximated $f_{double\,step}^0 = 2 \times f_{step}^0 = 0.240$ eV Å^{-1} and $f_{double\,kink}^0 = 2 \times f_{kink}^0 = 0.412$ eV. We extracted $B_{double\,step} = 17.11$ eV Å^2 by scaling B_{step} with the ratio of the dipole moments of double steps and single steps, as explained in the Appendix B.

However, as we performed the flame-annealing in air and immediately transferred the sample for cooling down into a glass cylinder with an Ar + H$_2$ mixture, we can not discard the presence of small amounts of oxygen that could have lowered $f_{double\,step}$, thereby inducing the step bunching instability [1–4, 6]. This would explain why Lang and Blakely observed with LEED that even platinum stepped surfaces with a terrace width of only 3 atomic rows were stable if prepared in UHV [1, 2], although it has also been shown that Pt(997) with a terrace width of 9 atomic rows is prone to faceting, and not step bunching, in the absence of oxygen [4]. Future work is needed to check whether a different preparation method such as induction-annealing, which avoids exposure to air, would result in the nominal Pt(553) surface.

Finally, we can discard that the surface morphology on Pt(553) changes significantly with time while in the EC-STM, which reinforces our statement that the step bunches are formed during sample preparation with enhanced step mobility. Moreover, we observed the same step bunched structure on Pt(553) at least at two applied potentials: 0.1 V, where H covers the surface, and 0.4 V in the double layer region, where nothing is specifically adsorbed on the surface (see Appendix B). This indicates either that both the hydrogen adsorbed and the clean surface preserve the energetics of the most (thermodynamically) stable structure or that the surface is kinetically *frozen* at room temperature and thus visible changes do not occur within the time-span of our measurements. Our results differ from the ones reported in Refs. [31, 32] with a flame-annealed Ag(19 19 17) submerged in a CuSO$_4$ solution. These showed not only that the density of step bunches on this surface increases with time, but also that this increase occurs faster the higher the applied potential [33]. This indicates that the Ag(19 19 17) surface, as measured, did not reach thermodynamic equilibrium, and that surface diffusion at room temperature is still high enough for step rearrangement. Alternatively, the chemisorption of sulfate or copper deposition as well as alloy formation could have also had an important role [34].

3.6   Effects of Step Bunching in Electrocatalysis

Figure 3.5a shows the hydrogen desorption region from Cyclic Voltammograms (CVs) of Pt(111) and Pt(111)-vicinal surfaces with (111) steps in 0.1 M HClO$_4$. All stepped surfaces present a broad feature below 0.4 V and a sharp peak at around 0.13 V, which relate to terrace and step sites, respectively [35]. Pt(553) and Pt(221) show, in addition, an extra peak at around 0.185 V that was previously attributed to hydrogen desorption from narrow terraces [36]. However, we know now that it is related to hydrogen desorption and its (partial) replacement with hydroxide at step bunches, as discussed in detail in Chapter 4. A similar peak is also observed on Pt(110)-vicinals with (111) steps [37], which supports further our new insights. Pt(775) does not show this feature, but the potential shift of the single step peak (see Appendix B) suggests that also this surface exhibits (some) step bunching.

Step bunching also affects E_{pztc}. As E_{pztc} is closely related to the work function, one expects a linear decrease of E_{pztc} with the step density according to [14, 32, 38–40]:

$$\Delta E_{pztc}(\tfrac{1}{L}) = E_{pztc,\,stepped\,surface} - E_{pztc,\,(111)} = -\frac{p_z}{\epsilon_0\,a\,L} \tag{3.4}$$

where ϵ_0 is the vacuum dielectric constant and p_z the dipole moment at the steps. However, the red curve in Fig. 3.5b (data extracted from Refs. [7,41]) shows that the initial linear dependency of E_{pztc} with step density starts to deviate for n ≤ 7. This phenomenon was previously attributed to the decay of p_z due to the interference of the stress and electrical fields between close-spaced steps [42]. Evidently, as we now know that close spaced steps bunch, resulting in wider terraces, the real explanation must be different. Mainly, step bunching results in a decrease of the ratio p_z/L, as L is doubled but $p_{z,double\,step}$ << $2\,p_{z,single\,step}$ [28]. This leads to a higher E_{pztc} than expected.

Figure 3.5b shows in blue the local E_{pztc} at steps (data extracted from Ref. [43]), which is constant at low step densities but starts increasing at n = 7. As step bunches have a different p_z than single steps, this again suggests that the onset of step bunching starts with Pt(775).

Subsequently, we used both curves in Fig. 3.5b, our measured percentage of bunched steps on Pt(553), and equation 3.4 to calculate $p_{z,double\,step}$. Knowing that $p_{z,single\,step}$ = 0.14 D (in 0.1 M HClO$_4$) [7] and assuming that $p_{z,triple\,step} \approx p_{z,double\,step}$, we obtain $p_{z,double\,step}$ = 0.168 D and $p_{z,double\,step}$ = 0.172 D from the two curves, respectively. This means that the dipole moment of the double step is only ≈ 21 % larger than the one of the corresponding single step. To further confirm this, we use the average value of $p_{z,double\,step}$ = 0.170 D together with the measured percentage of bunched steps and estimate E_{pztc} for Pt(553) (drawn with the purple diamond), which is close to the value measured. The even greater deviation for Pt(221) and Pt(331) is most likely due to a larger fraction of triple (and maybe even higher order) steps formed to minimize the higher step-step repulsion.

On another topic, it is well known that the ORR in acidic media is most active at the concave sites situated at the lower step edge, where the OH$_{ad}$ intermediate binds weaker than on the (111) terraces [44, 45]. Consequently, one would expect the ORR activity to increase (almost) linearly with the number of these concave sites, and thus with step density (the effects of the Smouluchowski relaxation have a higher order dependency with the step separation, and thus are less significant [18–22]). However, Fig. 3.5c shows in red (data extracted from Refs. [8, 9]) that the ORR half-wave potential ($E_{1/2}$), an activity descriptor, increases linearly with step density only until n < 7.

As we know now that Pt(775), Pt(221), and Pt(331) undergo step bunching, this reduces the amount of lower step edge sites in approximation by a factor 1/2 if all steps would simply bunch into pairs (see Fig. 3.2). As these are the most active sites for the ORR, we expect an equivalent decrease of the activity. To check this, we horizontally shifted the data points of Pt(775), Pt(221), and Pt(331) (in Fig. 3.5c) to accommodate for the number of most active sites if all steps would be doubled. It is striking that the resulting data points (purple diamonds) fall now very close to the linear trend line, confirming again the importance of step bunching.

Finally, step bunching also impacts other structure-sensitive electrochemical reactions that are most active at step-related sites. Step bunches on Pt(111)-vicinals with n ≤ 5 show a reduced activity towards both the Hydrogen Oxidation Reaction [46] and the CO Oxidation Reaction [47]. By contrast, Nitrate Reduction shows a significant increase for n ≤ 5 [36], which suggests a more optimal binding of the reaction intermediates at the bunched steps.

Vacuum studies show that Pt(533), exhibiting (100) steps, undergoes step bunching during Ammonia Oxidation, resulting in a change in selectivity from producing N_2 to producing NO [48]. Moreover, in Chapter 4 we show that step bunching leads to a decrease of the hydrogen adsorption as well as platinum oxidation at step sites. To provide a graphical representation of our insights, we built up a stereographic triangle in which we indicate the surfaces that are unstable towards step bunching (see Fig. 3.5d and Appendix B). This is derived on the basis of the information in the literature regarding the electrochemical behavior of flame-annealed stepped platinum surfaces, together with this work and other characterization studies [24, 29, 30, 49, 50].

3.7 Conclusions

In this chapter we demonstrate that flame-annealed Pt(111)-vicinal electrodes with high step density undergo step bunching, which has a significant impact on the electrochemical behavior of the surface. Our statistical analysis of the terrace width and the step height distribution shows that, while Pt(554) presents a regular array of single steps separated by the nominal distance, 51 ± 5 % and 14 ± 3 % of the steps on Pt(553), which has higher step density, are bunched into pairs and triplets, respectively. This instability originates from the highly repulsive step-step interaction between closely distanced steps, which is lowered by forming step bunches with larger spacing in combination with a dipole moment that is increased only by $\approx$ 21 % to 0.17 D for double steps, in comparison to the 0.14 D of single steps. The bunching occurs during surface preparation at high temperature, when the surface mobility is enhanced. Pt(111)-vicinal electrodes with bunched steps exhibit an extra peak at around 0.185 V in the hydrogen desorption fingerprint, as well as an unexpected, non-linear trend of their E_{pztc} and ORR activity with their step density. Our new insight challenges the common assumption in electrochemistry that all vicinal surfaces present a regular array of monoatomic-height steps and can successfully explain the anomalous step density-dependent trends reported in literature.

Figure 3.5: Effects of Step Bunching on Platinum Electrochemistry. **(a)** Hydrogen desorption fingerprint of Pt(111) and (111)-vicinal surfaces with (111) steps recorded in 0.1 M $HClO_4$ at a scan rate of 50 mV s^{-1}. The peaks related to terraces, single (111) steps, and step bunches, the latter only present on Pt(553) and Pt(221), are indicated. **(b)** E_{pztc} (in red) and (local) E_{pztc} at step sites (in blue) versus the step density, extracted from Refs. [7, 41, 43]. The stepped surfaces that undergo step bunching (n ≤ 7) do not follow the linear decrease of E_{pztc} with step density shown in red. The purple diamond represents our estimation of E_{pztc} for Pt(553), calculated from a fit of the dipole moment for double steps. **(c)** ORR activity, represented by the half-wave potential, versus step density, extracted from Refs. [8, 9]. The ORR activity increases linearly with the step density for n ≥ 9. The purple diamonds represent the adjusted values for Pt(775), Pt(221), and Pt(331) assuming that they only have double steps. **(d)** Stereographic triangle showing the stable surfaces in green and the unstable ones in red. Pt(110) forms a (1x2) missing-row reconstruction [24, 49], while Pt(100) is unreconstructed in electrolyte [50].

References

[1] B. Lang, R. W. Joyner, and G. A. Somorjai, *Surf. Sci.*, **30**, 454 (1972).

[2] D. W. Blakely and G. A. Somorjai, *Surf. Sci.*, **65**, 419 (1977).

[3] G. Comsa, G. Mechtersheimer, and B. Poelsema, *Surf. Sci.*, **119**, 159 (1982).

[4] E. Hahn, H. Schief, V. Marsico, A. Fricke, and K. Kern, *Phys. Rev. Lett.*, **72**, 3378 (1994).

[5] J. Clavilier, R. Faure, G. Guinet, and R. Durand, *J. Electroanal. Chem.*, **107**, 205 (1980).

[6] E. Herrero, J. M. Orts, A. Aldaz, and J. M. Feliu, *Surf. Sci.*, **440**, 259 (1999).

[7] V. Climent, R. Gómez, and J. M. Feliu, *Electrochim. Acta*, **45**, 629 (1999).

[8] A. Kuzume, E. Herrero, and J. M. Feliu, *J. Electroanal. Chem.*, **599**, 333 (2007).

[9] A. M. Gómez-Marín and J. M. Feliu, *Catal. Today*, **244**, 172 (2015).

[10] Y. I. Yanson, F. Schenkel, and M. J. Rost, *Rev. Sci. Instrum.*, **84**, 023702 (2013).

[11] M. J. Rost, in *Encyclopedia of Interfacial Chemistry*, 1st ed., K. Wandelt, p.180, Elsevier, Amsterdam (2018).

[12] L. Jacobse, Y. F. Huang, M. T. M. Koper, and M. J. Rost, *Nat. Mater.*, **17**, 277 (2018).

[13] E. D. Williams and N. C. Bartelt, *Science*, **251**, 393 (1991).

[14] H. Ibach, *Physics of Surfaces and Interfaces*, Springer, Amsterdam (2006).

[15] J. Lapujoulade, *Surf. Sci. Rep.*, **20**, 191 (1994).

[16] N. C. Bartelt, T. L. Einstein, and E. D. Williams, *Surf. Sci. Lett.*, **240**, L591 (1990).

[17] E. E. Gruber and W. W. Mullins, *J. Phys. Chem. Solids*, **28**, 875 (1967).

[18] R. Smoluchowski, *Phys. Rev.*, **60**, 661 (1941).

[19] C. Jayaprakash, C. Rottman, and W. F. Saam, *Phys. Rev. B*, **30**, 6549 (1984).

[20] K. H. Lau and W. Kohn, *Surf. Sci.*, **65**, 607 (1977).

[21] V. I. Marchenko and A. Ya. Parshin, *Sov. Phys. JETP*, **52**, 129 (1980).

[22] L. E. Shilkrot and D. J. Srolovitz, *Phys. Rev. B*, **53**, 122 (1996).

[23] G. Prévot, P. Steadman, and S. Ferrer *Phys. Rev. B*, **67**, 245409 (2003).

[24] K. Swamy, E. Bertel, and I. Vilfan, *Surf. Sci. Lett.*, **425**, L369 (1999).

[25] H. Jeong, E. D. Williams, *Surf. Sci. Rep.*, **34**, 171 (1999).

[26] J. Ikonomov, K. Starbova, H. Ibach, and M. Giesen, *Phys. Rev. Lett.*, **75**, 245411 (2007).

[27] R. C. Nelson, T. L. Einstein, and S. V. Khare, *Surf. Sci.*, **295**, 462 (1993).

[28] H. Ishida, A. Liebsch, *Phys. Rev. B*, **46**, 7153 (1992).

[29] A. Nakahara, M. Nakamura, K. Sumitani, O. Sakata, and N. Hoshi, *Langmuir*, **23**, 10879 (2007).

[30] N. Hoshi, M. Nakamura, O. Sakata, A. Nakahara, K. Naito, and H. Ogata, *Langmuir*, **27**, 4236 (2011).

[31] S. Baier, H. Ibach, and M. Giesen, *Surf. Sci.*, **573**, 17 (2004).

[32] H. Ibach and W. Schmickler, *Surf. Sci.*, **573**, 24 (2004).

[33] M. Giesen, G. Beltramo, S. Dieluweit, J. Müller, H. Ibach, and W. Schmickler, *Surf. Sci.*, **595**, 127 (2005).

[34] O. M. Magnussen, *Chem. Rev.*, **102**, 679 (2002).

[35] J. Clavilier, K. El Achi, and A. Rodes, *J. Electroanal. Chem.*, **272**, 253 (1989).

[36] S. Taguchi and J. M. Feliu, *Electrochim. Acta*, **52**, 6023 (2007).

[37] J. Souza-Garcia, V. Climent, and J. M. Feliu, *Electrochem. Commun.*, **11**, 1515 (2009).

[38] K. Besocke, B. Krahl-Urban, and H. Wagner, *Surf. Sci.*, **68**, 39 (1977).

[39] S. Trasatti, *J. Electroanal. Chem. Interf. Electrochem.*, **39**, 163 (1972).

[40] R. Gómez, V. Climent, J. M. Feliu, and M. J. Weaver, *J. Phys. Chem. B*, **104**, 597 (2000).

[41] R. Rizo, J. Fernández-Vidal, L. J. Hardwick, G. A. Attard, F. J. Vidal-Iglesias, V. Climent, E. Herrero, and J. M. Feliu, *Nat. Commun.*, **13**, 2550 (2022).

[42] P. N. Ross, *J. Chim. Phys.*, **88**, 1353 (1991).

[43] V. Climent, G. A. Attard, and J. M. Feliu, *J. Electroanal. Chem.*, **532**, 67 (2002).

[44] F. Calle-Vallejo, J. Tymoczko, V. Colic, Q. Huy Vu, M. D. Pohl, K. Morgenstern, D. Loffreda, P. Sautet, W. Schuhmann, and A. S. Bandarenka, *Science*, **350**, 185 (2015).

[45] F. Calle-Vallejo, M. D. Pohl, D. Reinisch, D. Loffreda, P. Sautet, and A. S. Bandarenka, *Chem. Sci.*, **8**, 2283 (2017).

[46] R. Kajiwara, Y. Asaumi, M. Nakamura, and N. Hoshi, *J. Elecroanal. Chem.*, **657**, 61 (2011).

[47] N. P. Lebedeva, M. T. M. Koper, J. M. Feliu, and R. A. van Santen, *J. Phys. Chem. B*, **106**, 12938 (2002).

[48] A. Scheibe, S. Günther, and R. Imbihl, *Catal. Letters*, **86**, 33 (2003).

[49] N. M. Marković, B. N. Grgur, C. A. Lucas, and P. N. Ross, *Surf. Sci.*, **384**, L805 (1997).

[50] L. A. Kibler, A. Cuesta, M. Kleinert, and D. M. Kolb, *J. Electroanal. Chem*, **484**, 73 (2000).

4 Quantitative Study of Electrochemical Adsorption and Oxidation on Pt(111) and its Vicinal Surfaces

Hydrogen and oxygen are key intermediates in many relevant electrochemical reactions such as the hydrogen oxidation and the oxygen reduction on platinum, which are the main processes in hydrogen fuel cells. Achieving improved catalyst design requires thus a deep understanding of their adsorption behavior. However, the interaction of hydrogen and oxygen with platinum step sites remains relatively limited, despite extensive fundamental research on their adsorption on platinum terraces. Our results show that the voltammetric peak related to hydrogen desorption from steps involves more than the simple desorption of one hydrogen atom per unit step length, which could point out towards an exchange mechanism between hydrogen and hydroxide, as stated in recent literature. At higher potentials, a one-dimensional surface oxide consisting of PtO_2 chains forms along the steps, giving rise to three voltammetric peaks that we relate to specific surface sites. Finally, we show that the adsorption of both hydrogen and oxygen is less pronounced at step bunches than at single steps, which we attribute to structural differences.

4.1 Introduction

The platinum-electrolyte interface is probably the most fundamentally studied system in electrocatalysis due to its relevance in electrochemical applications such as electrolyzers and fuel cells. Of special interest is the adsorption/desorption of hydrogen and oxygen on the platinum surface. The former has a crucial role in the hydrogen evolution and the hydrogen oxidation reaction [1–3], while the latter is a key intermediate in the oxygen reduction reaction (ORR) [4] as well as in oxidation reactions catalyzed by platinum [5].

The electrosorption of hydrogen on platinum starts at a potential more positive than the equilibrium potential for water reduction (or protons in acidic media) and thus it is often referred to as the *underpotential deposition* (upd) of hydrogen [1,6], H_{upd}, in analogy to the well-known upd of metals in electrodeposition [7,8]. The development of flame-annealing for single crystal preparation [9] allowed to probe the H_{upd} on well-defined crystallographic planes. These studies concluded that the hydrogen adsorption on platinum is surface specific (i.e. the adsorption energy depends on the coordination of the adsorption site) [10,11], which explained the differences observed in the respective Cyclic Voltammograms (CVs) of the low Miller-index planes: (111), (100), and (110) [12,13]. Not surprisingly, stepped platinum surfaces (vicinal to the low Miller-index planes) exhibit specific peaks in the H_{upd} *fingerprint*, allowing not only the differentiation between terrace and step contributions but also between different types of steps [14–16]. Nevertheless, recent studies support that these step peaks do not involve simple hydrogen adsorption/desorption, as it is the case on the terraces, but a replacement mechanism in which also hydroxide participates [17,18]. The details of this exchange process are still not fully understood.

Similarly to the above, the precise oxide structure at steps during platinum oxidation remains also unclear. The reason here is the complexity of this process: it involves multiple reaction steps [19], different surface oxidation states [20], and the so-called *place-exchange*, where platinum atoms are lifted up to a complete monolayer (ML) by oxygen atoms that go subsurface [21–27]. The first studies ignored the geometry effect of the adsorption sites and attributed the different oxidation peaks in the CV to different surface oxides, such as PtOH and PtO [28]. This picture was improved by Björling et al., who concluded that the multiple peaks in the oxidation region are likely due to the oxidation of different surface sites, such as terrace and step sites, with unique atomic arrangements [29,30]. Unraveling the oxide structure at the steps is of crucial importance, as the coverage of oxygenated species such as OH_{ad} and O_{ad} determines the ORR activity as well as the oxidation of organic molecules [4,5,31–34]. Moreover, it is known that surface oxidation is responsible for electrode degradation [35,36].

Furthermore, we recently proved with Electrochemical Scanning Tunneling Microscopy (EC-STM) that flame-annealed (111)-vicinal surfaces with terraces equal or narrower than Pt(775) are not stable and undergo step bunching, a well-known phenomenon in surface science (see Chapter 3) [37,38]. Additionally, we showed that these structural changes alter the reactivity of steps towards relevant surface-sensitive reactions such as the ORR. Therefore, also the hydrogen and oxygen adsorption on these unstable surfaces needs to be revisited.

To address these issues, here we deconvolute the terrace and step contributions in both the H$_{upd}$ and the oxidation region. We quantify our analysis by extracting the corresponding step charge densities. Our results show that the H$_{upd}$ step contribution involves more charge than the one corresponding to the desorption of one hydrogen atom per unit step length. This could point out towards a replacement mechanism between H$_{ad}$ and OH$_{ad}$ at the step sites, as stated in previous studies [17, 18]. Regarding the oxide, we present evidence from the coverage that the steps form PtO$_2$ rows, which agrees with previous work [39–42]. Finally, we demonstrate a decrease of the hydrogen and oxygen adsorption on bunched stepped surfaces, which we ascribe to the loss of step sites due to bunching.

4.2 Experimental

The CVs were recorded in a three-electrode glass cell that underwent sequential cleaning: first with an acidic potassium permanganate solution, then with diluted piranha, and finally by boiling it five times in ultrapure water (> 18.2 MΩ cm, Millipore, Milli-Q). We used a reversible hydrogen electrode (RHE) as reference electrode and a Pt wire (MaTeck, Germany) as counter. For the measurements we used a Pt(111) single crystal (Surface Preparation Laboratory, The Netherlands) and different (111)-vicinal surfaces with <110>/{111} steps (MaTeck, Germany): steps along a direction equivalent to [110] with {111} microfacets. In particular we used Pt(15 15 14), Pt(554), Pt(775), Pt(553), and Pt(221), which have nominal terrace widths of n = 30, 10, 7, 5, and 4 atomic rows, respectively. Prior to each experiment, the corresponding sample was etched electrochemically (125 cycles at 50 Hz and ± 2 V versus Pt) in an acidified 2.5 M CaCl$_2$ solution, flame annealed (3 min at ≈1250 K), and then cooled down in a 1:4 H$_2$/Ar mixture. We repeated this treatment at least three times before an experiment, performing the last annealing step to a slightly lower temperature (≈ 50 K lower) in order to create a denuded zone near the surface with less contamination. All the CVs were recorded in a dearated 0.1 M HClO$_4$ solution (Merck Suprapur) at a scan rate of 50 mV/s, using a potentiostat from Bio-Logic (VSP-300).

To correct for the surface miscut angle, we calculated all current and charge densities by using the electrochemical area (A_{ec}), which for stepped surfaces differs from the geometrical area (A_{geom}) according to:

$$A_{ec} = \frac{A_{geom}}{cos(\alpha)} \tag{4.1}$$

in which α is the angle of misorientation of the surface with respect to the (111) plane.

4.3 Cyclic Voltammetry of (111)-Vicinal Surfaces with (111) Steps

Figure 4.1 shows the CVs of Pt(111) and selected (111)-vicinal surfaces with (111) steps, recorded in 0.1 M HClO$_4$ between 0.06 and 1.35 V at a scan rate of 50 mV/s. The general trends of local changes in the CVs due to an increase of step density are indicated with black arrows. The broad feature below 0.4 V, attributed to hydrogen adsorption/desorption

at terrace sites [3, 14], becomes narrower with increasing step density, indicating a decrease in entropy of the adsorbed hydrogen atoms [8, 43]. Moreover, there is a sharp peak related to the (111) step sites at around 0.128 V [44–46]. In addition, Pt(553) and Pt(221) exhibit an extra hydrogen peak at around 0.18 V that is only observed on platinum stepped surfaces with narrow terraces [47]. In Chapter 3 we presented evidence from EC-STM measurements that this is attributed to hydrogen adsorption/desorption (and its partial exchange with hydroxide) at step bunches, which are only present on (unstable) surfaces with high step density.

The presence of steps also alters the adsorption of hydroxide in the so-called butterfly peak, the onset of which shifts from 0.55 V for Pt(111), to 0.62 V for Pt(221). In addition, the sharp OH peak decreases in height and becomes broader, indicating a suppression of the phase transition that results in an ordering of the OH adlayer [48]. Without the presence of steps, the region between 0.85 V and 1.0 V shows a flat plateau that is a consequence of a kinetic barrier for the formation of surface oxide on flat terraces [19, 49–51]. On (111)-vicinal surfaces, however, this region is characteristic for step oxidation, explaining the presence of the voltammetric peaks observed [30, 51]. The fact that step sites oxidize at lower potentials than terrace sites agrees well with theoretical calculations [40–42, 52], which show that the oxygen atoms bind stronger at steps.

The peak at around 1.1 V is attributed to the conversion of OH_{ad} to O_{ad} on the terraces [19, 49, 53] and the Reversible Place-Exchange (PE_{rev}) between O_{ad} and platinum surface atoms [26, 27, 51, 54–57]. This process results in platinum atoms being lifted out of the surface by almost one atomic layer due to the subsurface migration of oxygen atoms (i.e. two oxygen atoms go subsurface beneath one platinum atom involved) [26, 56, 57]. As the PE_{rev} is a precursor to the terrace oxidation [51], its voltammetric peak decreases in intensity when diminishing the number of terrace sites. Moreover, the PE_{rev} peak becomes broader and shifts its position with increasing step density (narrower terraces), which must be due to Smoluchowski relaxations changing the inter-atomic distances in the terrace [58–61]. Increasing the electrode potential above ≈ 1.17 V leads to the Irreversible Place-Exchange (PE_{irr}) [26, 27, 54, 56, 62], which ultimately results in the roughening of the surface due to the formation of nanoislands [27, 51, 57, 63–65].

4.4 Adsorption of Hydrogen and Hydroxide at Step Sites

Clavilier and co-workers have previously found that the charge under the peak at around 0.128 V scales linearly with the step density, with 1 electron per unit step length, and thus they attributed it to the adsorption/desorption of one hydrogen atom per step site [44, 45]. However, discrepancies arose from later observations. Firstly, the interaction energy between hydrogen atoms adsorbed on the terrace is repulsive, while there is an apparent attractive interaction between the adsorbed species that give rise to the H_{upd}-step peak [66–68]. Secondly, this peak shifts with 10 mV per pH unit in RHE scale, which can not be explained with simple hydrogen adsorption/desorption [69]. Thirdly, laser-pulsed experiments revealed a change of the dipole moment from (part of) the adsorbed species at potentials around the H_{upd}-step peak [70].
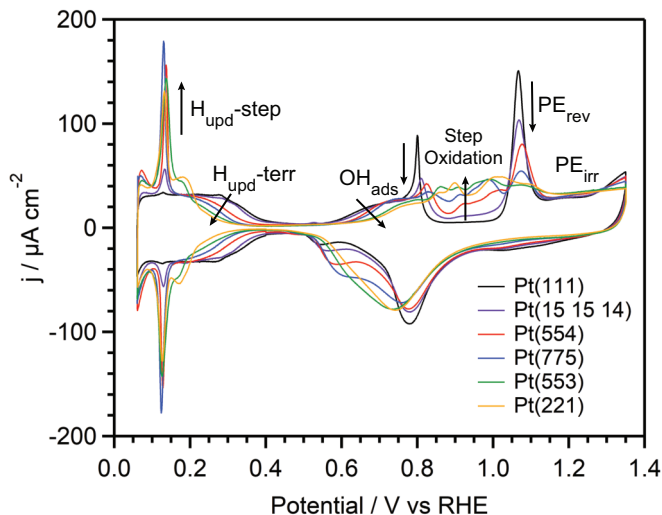
Figure 4.1: Cyclic Voltammograms of Pt(111) and its Vicinal Surfaces with (111) Steps. CVs recorded in 0.1 M HClO$_4$ from 0.06 to 1.35 V using a scan rate of 50 mV s^{-1}. The most relevant regions are indicated with the corresponding text and the general trend when increasing the step density with arrows.

To solve the above conflicts, a model was proposed in which hydroxide replaces hydrogen at the steps [67, 69]. This was supported by DFT calculations, which affirmed the stability of an OH/water structure at the steps and explained the anomalous pH dependence of the H$_{upd}$-step peak potential [17, 71, 72]. Moreover, Rizo et al. confirmed the presence of OH$_{ad}$ on Pt(311) at potentials within the H$_{upd}$ region via CO displacement and *in-situ* Raman experiments [18]. However, as shown in Chapter 3 this surface has a significant fraction of step bunches, which could lead to a preferential adsorption of OH. Therefore, the definitive confirmation if OH replaces H$_{ad}$ at single steps would require repeating these experiments with a stable stepped surface such as Pt(554).

Independently of the above, there is not yet a consensus regarding the total charge involved in the H$_{upd}$-step peak [44, 45, 69, 73]. The discrepancies are partially due to the different strategies used to deconvolute the step and the terrace contributions, together with the earlier belief that the maximum H$_{upd}$-step charge could not exceed one electron, i.e. one hydrogen per platinum step site. In this work, we numerically fit the H$_{upd}$-terrace peak with a Frumkin isotherm, knowing that it describes well the hydrogen adsorption/desorption [43, 74–77]:

$$ln\left(\frac{\Theta_{H_{upd},terr}}{1-\Theta_{H_{upd},terr}}\right) = -\frac{e\,(E-E_{RHE})}{k_B\,T} - \frac{\Delta G^0_{H_{upd},terr}}{k_B\,T} - \frac{w\,\Theta_{H_{upd},terr}}{k_B\,T} \tag{4.2}$$

in which $\Theta_{H_{upd},terr}$ is the hydrogen coverage at the terrace, E is the electrode potential, E_{RHE} is the reference (RHE) potential, $\Delta G^0_{H_{upd},terr}$ is the free energy of hydrogen adsorp-

tion on the terrace, and w is the interaction energy, which is positive for repulsive interactions and negative for attractive interactions between the adsorbates. k_B, T, and e have their usual meanings: the Boltzmann constant, temperature ($T = 298$ K), and the elemental electron charge, respectively.

At potentials where hydrogen desorption occurs only on the terraces, $\Theta_{H_{upd},terr}$ is directly given by:

$$\Theta_{H_{upd},terr} = \frac{1}{Q_{H_{upd},(1e^-/terr\,site)}} \int_{E_{DL}}^{E} \frac{j_{H_{upd}}(E) - j_{DL}}{v} \, dE \tag{4.3}$$

where $j_{H_{upd}}(E)$ is the voltammetric current density, j_{DL} ($\approx 3\ \mu A\,cm^{-2}$) is the current density contribution from the double layer charging, and v is the scan rate ($v = 50$ mV/s). $Q_{H_{upd},(1e^-/terr\,site)}$ is the charge density corresponding to one electron interchanged per terrace site, and is given by [44, 45]:

$$Q_{H_{upd},(1e^-/terr\,site)} = \frac{2\,(n-2)\,e}{\sqrt{3}\,d^2\left(n-\frac{2}{3}\right)} \tag{4.4}$$

where n is the number of atomic rows on a single terrace and d is the distance between two Pt atoms in the close packed (111) terrace.

Figure 4.2 shows the resulting fits of the H_{upd}-terrace peak for each of the stepped surfaces used. From 0.2 V (0.23 V for Pt(221)) there is good match between the fitted curve $j_{H_{upd},terr}$, in blue, and the experimental $j_{H_{upd}}$ curve in black, which demonstrates the validity of our fit. This is also evident from Fig. C.1 (in Appendix C), where we show the respective hydrogen coverages versus the electrode potential.

Table 1 shows $\Delta G^0_{H_{upd},terr}$ and w that we obtained in this study, together with the values reported in Ref. [43]. Both parameters decrease in absolute values with increasing step density, which is an effect of the Smoluchowski relaxation on the terraces, i.e. the terrace atoms are more compressed together, resulting in a higher driving force necessary to bind the hydrogen at the three-fold hollow sites [59–61].

	n	$\Delta G^0_{H_{upd},terr}$ / eV	w / eV
$Pt(111)$*	–	−0.289	0.286
$Pt(15\,15\,14)$	30	−0.279	0.293
$Pt(15\,15\,14)$*	30	−0.285	0.287
$Pt(554)$	10	−0.232	0.228
$Pt(775)$	7	−0.214	0.198
$Pt(553)$	5	−0.197	0.176
$Pt(553)$*	5	−0.203	0.165
$Pt(221)$	4	−0.185	0.182

Table 4.1: Thermodynamic Data for the Hydrogen Adsorption on Terraces. Free energy of hydrogen adsorption on the terrace ($\Delta G^0_{H_{upd},terr}$) and the corresponding interaction energy (w). *Reported values from Ref. [43].
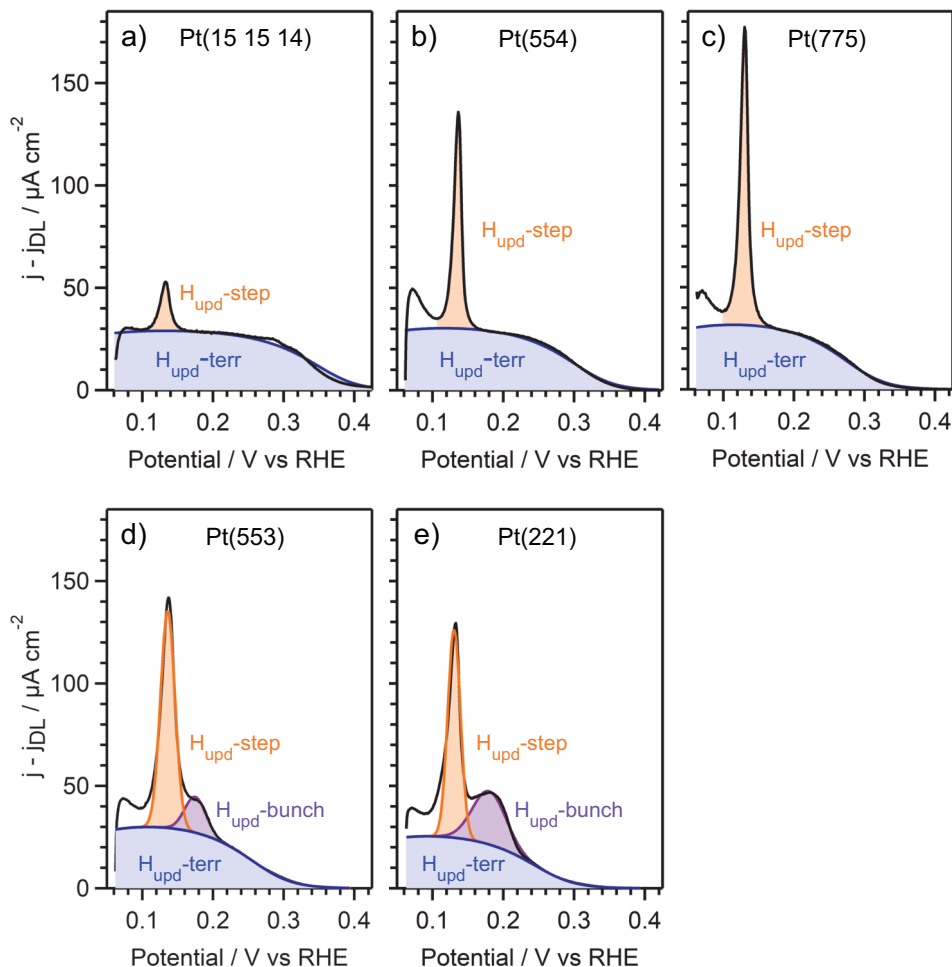
Figure 4.2: H_{upd} Deconvolution into Step and Terrace Contributions. The black line represents the total, measured H_{upd} current density after correction for the current density contribution from the double layer charging, while the blue line is the fit of the the H_{upd}-terrace current density with a Frumkin isotherm. The corresponding terrace, single step, and step bunch contributions to the H_{upd} charge density are colored in blue, orange, and purple, respectively.

Figure 4.3a shows the experimentally determined H_{upd}-terrace charge, $Q_{H_{upd}, terr}$, versus the theoretical charge of one electron per terrace atom given by eq. 4.4. All the data points except for Pt(221) lie on a straight line that corresponds to a maximum hydrogen coverage of 0.67 ML. This value agrees very well with the earlier reported values for Pt(111) [74, 76], as well as for (111)-vicinal surfaces [44, 45].

Subsequently, for Pt(15 15 14), Pt(554), and Pt(775), we determined the step charge by

integrating the H_{upd}-step peak current, $j_{H_{upd},step}$, that remains after subtracting $j_{H_{upd},terr}$. We set the lower integration limit to 0.10 V to exclude the peak at 0.07 V, which is due to the oxidation of H_2 gas formed during the preceding cathodic scan (i.e. see the steep rise at 0.06 V in Fig. 4.1). For Pt(553) and Pt(221), we deconvoluted the single-step and the step-bunch peaks with Gaussians. Figure 4.3b shows the resulting H_{upd}-step (in orange), H_{upd}-bunch (in purple), and total step (in red) charges plotted versus the theoretical charge assuming one electron interchanged per unit step length, which is given by [44, 45]:

$$Q_{Hupd,(1e^-/unit\,step\,length)} = \frac{2e}{\sqrt{3}\,d^2\left(n-\frac{2}{3}\right)} \tag{4.5}$$

For Pt(15 15 14), Pt(554), and Pt(775), we obtained 1.30 electrons per unit step length from the slope of the linear regression. This result is close to the 1.2 electrons per unit step length reported in Ref. [73], but significantly larger than the 1.0 electrons per unit step length found by Clavilier et al. [44, 45]. The differences are probably due to the different methodology used to deconvolve the H_{upd} terrace and step contribution. Our results show that the H_{upd}-step peak does not involve the simple desorption of one hydrogen per platinum step atom, as this would result in exactly 1.0 electrons per unit step length. Although it is not a proof, the charge obtained of 1.30 electrons per unit step length could be explained by the exchange mechanism proposed in the literature [17, 18, 67, 69–72], in which hydrogen is (partially) replaced by hydroxide. Following this argument, 1.0 electrons would be attributed to hydrogen desorption and 0.3 electrons to hydroxide adsorption, resulting in 0.3 ML OH adsorbed at the steps at potentials more positive than the H_{upd}-step peak. This would agree with DFT calculations, which show that low $OH_{ad,\,step}$ coverages, e.g. 1/3 ML, are the most favorable thermodynamically, as the co-adsorption of water is necessary to stabilize the adsorbed structure [17, 71, 72].

For Pt(553) and Pt(221) the normalized total H_{upd}-step charge is lower: 1.21 and 1.06 electrons per unit step length, respectively (see Fig. 4.3b). This is because these surfaces present not only single steps, but an even larger fraction of step bunches. Concretely, in Chapter 3 we quantified with EC-STM that Pt(553) has 35±4 % of single steps, 51±5 % of double steps, and 14±3 % of triple steps. As illustrated in Fig. 4.4, (111)-step bunches consist of an upper and a lower step edge as well as a {111} facet. As the latter is not present on single steps, it must be the reason for the (extra) H_{upd}-bunch peak on Pt(553) and Pt(221), shown in Fig. 4.2. On Pt(553), the H_{upd}-bunch peak involves a charge of 0.23 electrons per unit step length. Knowing that this charge must originate from the {111} facets at double and triple steps, from which we know their percentages, we calculated that only 0.67±0.04 electrons are interchanged per facet site. This is only half of the 1.30 electrons transferred per unit step length at single steps, and thereby it explains the decrease of the (normalized) total H_{upd}-step charge due to step bunching.

Similarly, as the upper and lower step edges from single steps are geometrically equal to the ones from bunched steps, we can calculate the charge expected for the H_{upd}-step peak of Pt(553). Knowing that 1.30 electrons are interchanged per unit step length at single step sites, as well as the percentage of single, double, and triple steps, we obtained 0.85±0.03 electrons per unit step length. This value is not too far from the one measured of 0.98 electrons per unit step length, shown in orange in Fig. 4.3b.
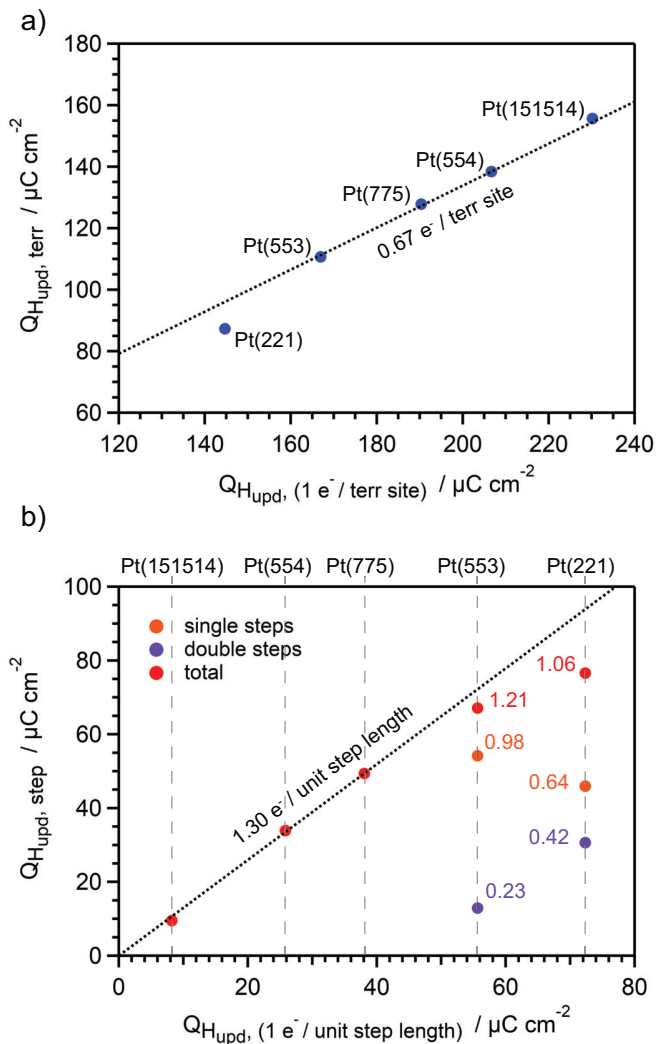
Figure 4.3: Correlation between the Measured and the Theoretical H_{upd} Charge Densities on Terraces and Steps. (a) H_{upd} charge densities on terraces, as given by a Frumkin isotherm fit, versus the theoretical charge densities assuming one electron is transferred per terrace site. **(b)** H_{upd} charge densities from single steps (orange), step bunches (purple), and the sum of them (red), versus the theoretical charge densities assuming one electron is interchanged per unit step length. We also provide the experimental values in units of electrons per unit step length.

a) *Single steps* b) *Double steps*
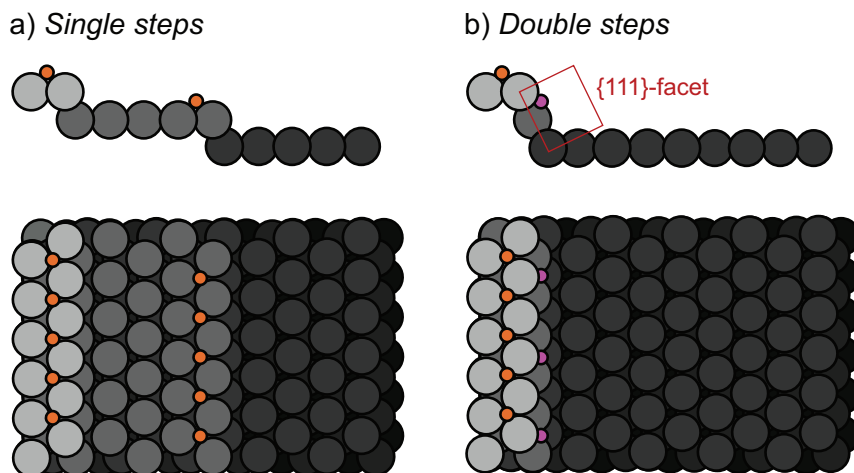
Figure 4.4: Hydrogen Adsorption at Single and Bunched Steps. (a) Hydrogen adsorption on a (111) single step and **(b)** on a double (bunched) step. For the single step site, we have drawn the hydrogen adsorbed at fcc sites at the upper step edge (in orange), although this is not clear from DFT calculations due to the similar binding energies between the fcc, hcp, and bridge sites [52, 71]. Moreover, from our quantitative analysis we can not discard that the step sites related to the H_{upd}-step peak are located, instead, at the lower step edge, as this would result in the same H_{upd}-step charge. On step bunches hydrogen adsorbs, in addition, at the {111}-facet formed (in purple), although we know from the charge density analysis that some of these sites must remain unoccupied. A triple step (not shown here) presents one row of fcc adsorption sites at the upper step edge and two rows at the {111}-facet.

4.5 Adsorption of Oxygen at Step Sites

Based on Fig. 4.1 and Refs. [30, 51], we know that step oxidation occurs between 0.85 and 1.05 V and it involves three voltammetric peaks with unknown charge density. We therefore fit these peaks with Gaussian functions, which is a decent approximation to the Frumkin isotherm [78, 79]. In order to determine the lower and upper boundaries for the fit, we plotted the Chi Squared versus the lower and upper fit potential and choose for the inflection points where the Chi Squared begins to plateau (see Figs. C2 and C.3 in Appendix C).

Figure 4.5 shows, for each of the stepped surfaces, the deconvolution with the three step oxidation Gaussians (in purple, orange, and blue) as well as an additional one for the PE_{rev}-peak (in green). The yellow and gray curves are attributed to OH adsorption and to the PE_{irr} regime, respectively, and result naturally when subtracting the Gaussian fits from the total current density.

Figure 4.6 (a-c) shows the individual step oxidation charges, $Q_{PtOx, step}$, from each of the Gaussians, plotted versus the step density, while Fig. 4.6d shows the total, combined step oxidation charge. Each trend line relates to a different number of electrons transferred per
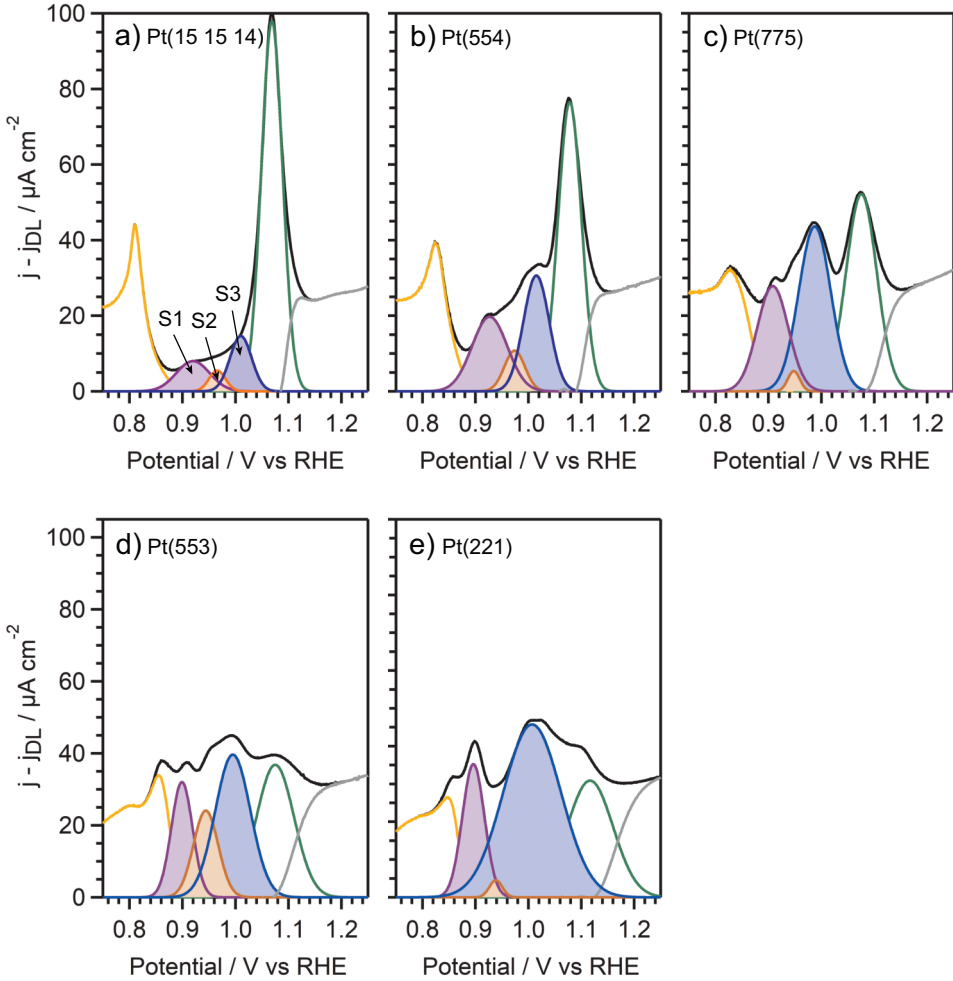
Figure 4.5: Deconvolution of the Platinum Oxidation Region: the three step oxidation peaks (S1, S2, and S3, respectively) as well as the PE$_{rev}$-peak (green curve) are obtained with Gaussian fit functions. The OH$_{ads}$ butterfly peak in yellow and the PE$_{irr}$-peak in gray are derived by subtraction of the Gaussian peaks from the measured total current density, shown in black.

unit of step length, $q_{PtOx,step}$, which we calculated with:

$$q_{PtOx,step} = \frac{\sqrt{3}\,d^2}{2e}\,b \tag{4.6}$$

where b is the slope of the given trend line. For the sake of simplicity, we have provided the values of $q_{PtOx,step}$ (and not b) next to each of the trend lines. Alternatively, we could have also calculated $q_{PtOx,step}$ for each individual data point, knowing that:

$$Q_{PtOx,step} = \frac{q_{PtOx,step}\, 2\, e}{\sqrt{3}\, d^2} \frac{1}{n - \frac{2}{3}} \tag{4.7}$$

Interestingly, Fig. 4.6a as well as Fig. 4.6d show two different trends, indicating a different degree of oxidation between single steps and bunched steps, which are in our case mainly double steps. We will discuss this in more depth at the end of this section, and will focus now on identifying the specific processes that give rise to each of the step oxidation peaks (see Fig. 4.7a) and their relation to specific atomic sites.
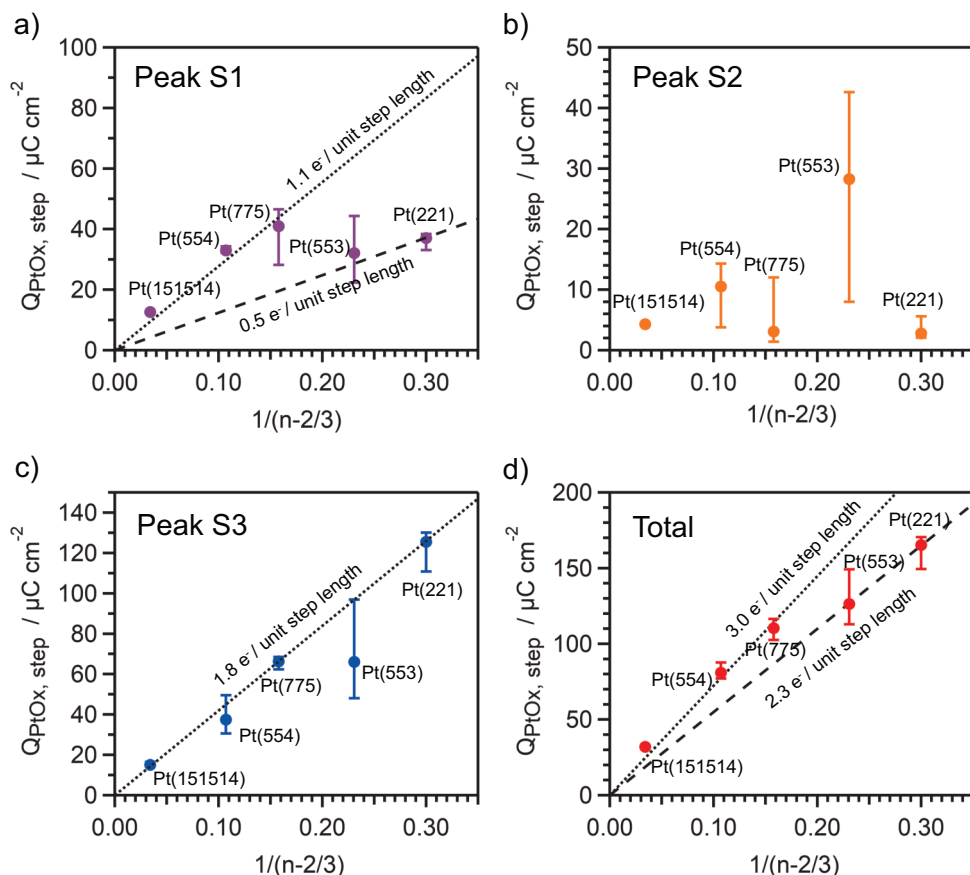
Figure 4.6: Step Oxidation Charges versus Step Density: (a-c) step oxidation charges resulting from the integral of each of the step oxidation peaks fitted in Fig. 4.5, as indicated. **(d)** shows the total step oxidation charge, which is the sum of the three peaks. We also show the resulting numbers of electrons transferred per unit step length for each peak, which we calculated from the trend lines. In **(a)** and **(d)**, two different regimes are clearly visible: one involving Pt(15 15 14), Pt(554), and Pt(775), and the other involving Pt(553) and Pt(221). The reason for the two regimes is step bunching. The error bars show the variation of the corresponding charges when taking sub-optimal fits (i.e. with a higher Chi Squared) obtained when varying slightly the upper and lower fitting boundaries.

Björling and co-workers found a step oxidation charge of around 2 electrons per unit step length for Pt(775) in 5 mM H_2SO_4 [30], and thus concluded that PtO forms, according to:

$$Pt^*_{step} + H_2O \rightleftharpoons PtOH_{step} + H^+ + e^- \tag{4.8}$$

$$PtOH_{step} \rightleftharpoons PtO_{step} + H^+ + e^- \tag{4.9}$$

In comparison with our results, Fig. 4.6d shows that step oxidation on Pt(15 15 14), Pt(554), and Pt(775) involves around 3.0 electrons per unit step length. This suggests that the oxidation proceeds further towards PtO_2:

$$PtO_{step} + H_2O \rightleftharpoons PtO_{2,step} + 2H^+ + 2e^- \tag{4.10}$$

However, the complete oxidation of the steps to PtO_2 (eq. 4.8-4.10) would require 4 electrons per unit step length, and not only 3. There are several explanations for this. Firstly, if true that 0.3 ML OH adsorbs at the steps within the H_{upd}-step peak, as discussed in the last section, the step oxidation charge expected in the platinum oxidation region must decrease by 0.3 electrons per unit step length. Moreover, we can not discard that part of the adsorption of OH at steps is convoluted with the one at the terraces, and thus the steps might be covered with 1 ML OH_{ad} before entering the step oxidation region. We would overlook this charge in our quantification.

The formation of PtO_2 at steps is supported by DFT, Force Field, and X-Ray Spectroscopy studies in vacuum, which all agree that, at high oxygen chemical potential, two oxygen atoms adsorb for each Pt step atom, resulting in a one-dimensional PtO_2 structure along the step [39–41]. Interestingly, there are indications for similar oxide chain structures on the (111) terraces [26, 27, 40, 51, 58, 62, 80, 81].

The formation of PtO_2 requires at least two geometrically different adsorption sites at the (111) step edge, as it involves adsorbing two oxygen atoms to one step platinum atom [40]. In an STM study, Feibelman and co-workers showed that, at low coverages, O adsorbs at the upper terrace on the fcc sites (see purple atoms in Fig. 4.7b) [82], which is not surprising as, at low coverages, oxygen adsorbs also on fcc sites on the terraces [83]. Upon increasing oxygen coverage, the chemical potential increases, resulting in the formation of one-dimensional PtO_2 chains along both (111) and (100) type of steps [39–41]. For (111) steps, the required second oxygen atom adsorbs at the lower step edge (partially subsurface), just on top of the lower step edge atom, as indicated in Fig. 4.7b with the blue atoms [40]. Knowing that this subsurface site is only occupied at higher oxygen coverages, the corresponding voltammetric peak must also appear at higher potentials.

Keeping the above in mind, we attribute the S1 peak in Fig. 4.7a to oxygen adsorbing at the upper part of the step, while the S3 peak must come from the lower, partial subsurface adsorption. This implies that the adsorption of OH (equation 4.8) is coupled with its oxidation to $O_{ad,\,step}$ (equation 4.9), giving rise to only one voltammetric peak, S1. Alternatively, one could think that this first peak is attributed to the OH adsorption at both the upper and the lower parts of the step, while the S3 peak would relate to the further oxidation towards $O_{ad,\,step}$. Both possibilities would result in a charge equivalent to 2.0 electrons per unit step length for both the S1 and the S3 peak. Therefore, we can not discard any of them from our quantitative analysis, which on surfaces with (predominantly) single steps deliver 1.1
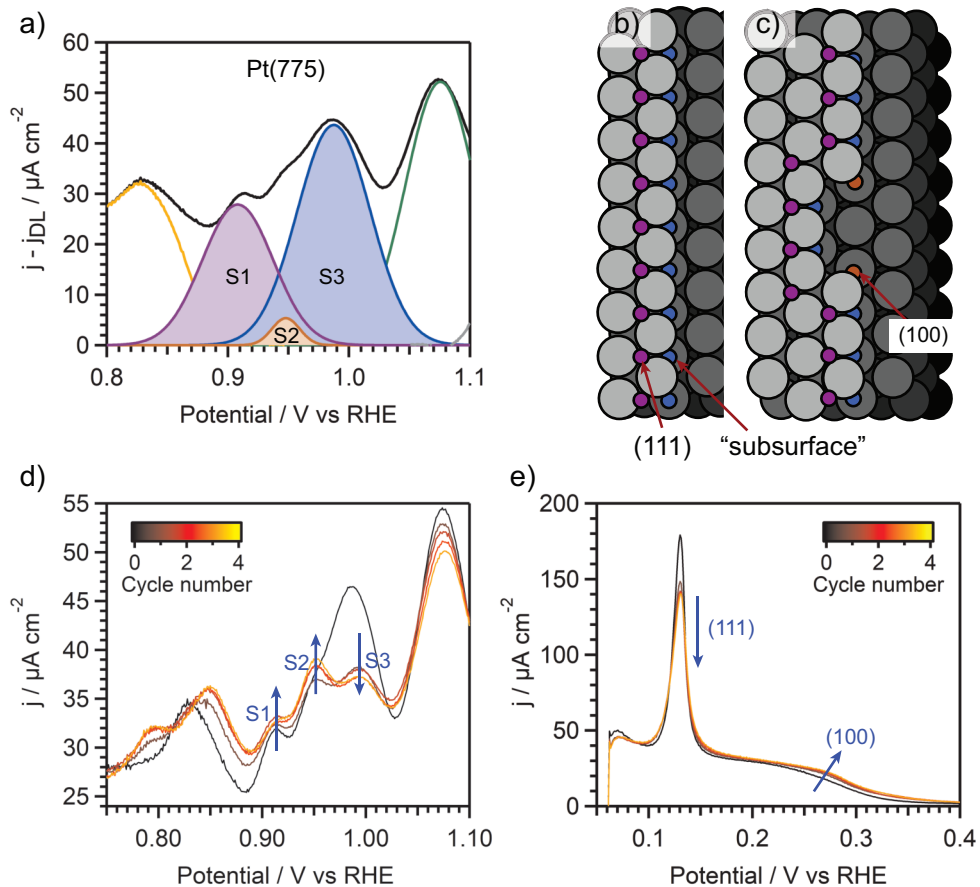
Figure 4.7: Atomic Site Identification of the Step Oxidation Peaks. **(a)** Step oxidation peaks of Pt(775). **(b)** Corresponding oxygen adsorption sites at the (111) (fcc) position at the upper step edge and the threefold subsurface position at the lower step edge. **(c)** Oxygen adsorption sites at a faceted (111) step with (100) microfacets, which present a partially subsurface site with twofold coordination at the lower step edge. **(d)** Step oxidation peaks upon oxidation-reduction cycling: S1 and S2 increase in intensity due to the increase in the number of (111) and (100) sites, respectively, while S3 decreases due to the annihilation of subsurface sites at the lower (111)-step edge. **(e)** H$_{upd}$ region upon oxidation-reduction cycling: the (100) step peak increases at the expense of the (111) step peak during the first 5 cycles.

and 1.8 electrons per unit step length, respectively (see Fig. 4.6a and 4.6c). The fact that the former value is much lower than the expected 2.0 electrons per unit step length stems from one of the explanations given above regarding the total step oxidation charge. If the steps would be already covered with hydroxide before reaching the step oxidation region, we would expect the S1 peak to exhibit a charge of 1.0 electrons per unit step length, which is close to the value we measured.

4

The S2 peak represents only a low percentage of the total step oxidation charge, except on Pt(553), where the error bar is large. Therefore, we assigned this peak to oxygen adsorption at (100) microfacets that are formed due to the presence of kinks (see Fig. 4.7c). The concentration of kinks, and thus of (100) microfacets, is naturally given by the temperature and the kink formation energy (see Appendix C) [8]. However, this concentration can increase due to the adsorption of species like hydrogen and oxygen. The former can induce the "roughening" of (111) steps into triangular microfacets composed by (100)-steps [84], while the oxidation of steps results in their decomposition into clusters with predominantly (111) microfacets [63, 64, 85–88]. This latter process is primarily driven by the buckling of the step atoms [89–91], which can even be pushed out onto the upper terrace in order to compensate for the high repulsive-interaction between the oxygen atoms as well as for the lattice mismatch between PtO_2 and platinum [58, 62, 80].

Figure 4.7d shows the evolution of the step oxidation region upon oxidation-reduction cycling between 0.06 V to 1.35 V, which leads to faceting and ultimately to the fragmentation of the (111) steps into clusters [88]. This results in an increase of the (100) step length at the expense of the (111) steps, as evident from the evolution of the respective peaks in the well-known H_{upd} region [46, 63, 64, 87], shown in Fig. 4.7e, and from the counting of the blue atoms in Fig. 4.7c. As only the S3 peak in Fig. 4.7d decreases in intensity with cycle number, it must be attributed to a surface site that disappears during this process: the partially subsurface sites at the lower (111) step edge, as we assigned earlier. We also related the S1 peak to the (111) sites at the upper terrace, which grow in number during oxidation-reduction cycling due to the increase of the total step length (note from Fig. 4.7d that both (111) and (100) microfacets present these O adsorption sites [39–41]). In each oxidation-reduction cycle the steps become more faceted, and thus have a larger fraction of (100) microfacets. Therefore, the rise of the S2 peak is attributed to the increase of the partially subsurface sites at the (100) step edges (see orange atoms in Fig. 4.7c).

Finally, we discuss how step bunching can explain the decreased step oxidation charges for Pt(553) and Pt(221), as shown in Fig. 4.6. Figure 4.8a and 4.8b represent the oxygen adsorption on a Pt(553) surface with single steps and with double steps, respectively. While single steps accommodate (at most) 2 rows of oxygen each (in purple and blue), and thus a total of 4 rows in this picture, only 3 oxygen rows can adsorb at double steps. This is a factor 1/4 less, which is the same that we find when comparing the two regimes in Fig. 4.6d: 3.0 electrons per unit step length on surfaces with single steps and 2.3 electrons per unit step length on surfaces with mainly double steps. As we know from EC-STM measurements that Pt(553) has actually 35±4 % of single steps, 51±5 % of double steps, and 14±3 % of triple steps (see Chapter 3), we can calculate more precisely the expected step oxidation charge. Assuming also that four oxygen rows adsorb on each triple step (not shown in Fig. 4.8), we obtain a value of 2.48±0.05 electrons per unit step length, which is close to the value of 2.3 electrons per unit step unit length shown in Fig. 4.6d for Pt(553). From Fig. 4.8 it is also evident that the lower step oxidation charge on surfaces with mainly step bunches originates from a decrease in the number of (111) sites at the upper step edge (purple atoms). This is also reflected in Fig. 4.6a, which shows that the oxidation of these sites on Pt(553) and Pt(221) involves about half of the number of electrons per unit step length compared to Pt(15 15 14), Pt(554), and Pt(775). From the measured fraction of step

bunches on Pt(553), we expect 0.70±0.03 electrons per unit step length on Pt(553). Lastly, the number of adsorption sites at the lower step edge (blue atoms) does not change due to step bunching, which explains that we only observe one trend in Fig. 4.6c.
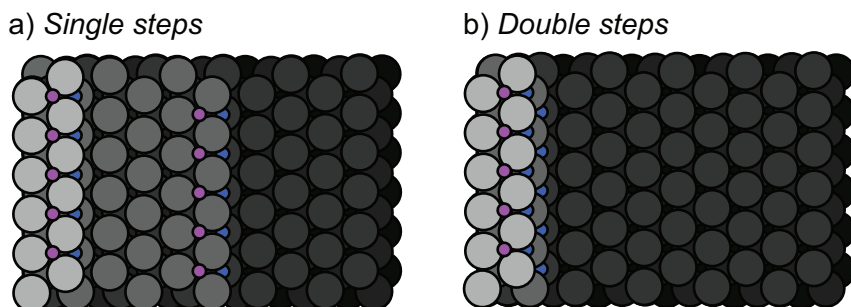
a) *Single steps*   b) *Double steps*

Figure 4.8: Oxidation of Single and Double Steps. **(a)** PtO_2 structure on single steps of Pt(553). The purple and blue oxygen circles represent oxygen atoms adsorbed at (111) (fcc) sites on the upper step edge and partially subsurface sites on the lower step edge, respectively. **(b)** PtO_2 structure on double steps of Pt(553). One row of O_{ad} at the upper step edge is missing in comparison to the single step structure.

4.6   Conclusions

In the present study, we used platinum (111)-vicinal surfaces to quantify the adsorption of H and O at step sites. For each of the stepped surfaces used, we fitted the H_{upd}-terrace peak with the Frumkin isotherm in order to deconvolute it from the H_{upd}-step peak. The subsequent charge analysis of both voltammetric peaks concludes that 0.67 electrons are transferred per terrace site on Pt(15 15 14), Pt(554), Pt(775), and Pt(553), while this charge is lower for Pt(221). We also found that 1.3 electrons are transferred per unit step length for Pt(15 15 14), Pt(554), Pt(775), which supports that the H_{upd}-step peak does not involve simple desorption of one hydrogen per step atom site, as this would imply exactly 1.0 electrons per unit step length. A possible explanation to the higher charge within this peak could be that it involves the (partial) replacement of $H_{ad, step}$ by $OH_{ad, step}$, as proposed in the most recent literature. On the other hand, we only quantified 1.21 and 1.06 electrons per unit step length for the step contribution on Pt(553) and Pt(221), respectively. This lower charge is attributed to the large fraction of step bunches on Pt(553) and Pt(221), which even give rise to an extra peak, the H_{upd} step-bunch peak, not present on stable (111)-vicinal surfaces.

At higher electrode potentials (between 0.85 V and 1.05 V), the steps oxidize, giving rise to three peaks. For Pt(15 15 14), Pt(554), and Pt(775), these three peaks imply a total (combined) charge of around 3.0 electrons per unit step length, while only 2.3 electrons per unit step length for Pt(553) and Pt(221). Although we can not discard that part of the step oxidation charge might be convoluted with the $OH_{ad, terr}$ region at around 0.7 V, our results indicate that the oxidation process results in PtO_2 chains along the steps. This agrees well

with DFT calculations and XPS measurements in vacuum, as well as with the oxide spokes observed (also in vacuum) on platinum terraces. Based on our new understanding, we identified the specific step sites where oxygen adsorbs giving rise to each of the three step oxidation peaks. From stronger to weaker oxygen binding, i.e. lower to higher peak potentials in the CV, these sites are: the (111) (fcc hollow) sites at the upper edge of the step, the (100) step sites that result from faceted (111) steps, and the partially subsurface sites at the lower step edge. Finally, we showed quantitatively that the decreased step oxidation charge that we found on Pt(553) and Pt(221) stems from the large fraction of bunched steps, which decreases the number of available (111) sites at the upper step edge where oxygen can adsorb.

References

[1] B. E. Conway, B. V. Tilak, *Electrochim. Acta*, **47**, 3571 (2002).

[2] J. K. Nørskov, T. Bligaard, A. Logadottir, J. R. Kitchin, J. G. Chen, S. Pandelov, and U. Stimming, *J. Electrochem. Soc.*, **152**, J23 (2005).

[3] G. Jerkiewicz, *Prog. Surf. Sci.*, **57**, 137 (1998).

[4] M. Luo and M. T. M. Koper, *Nat. Catal.*, **5**, 615 (2022).

[5] N. P. Lebedeva, M. T. M. Koper, E. Herrero, J. M. Feliu, and R. A. van Santen, *J. Electroanal. Chem.*, **487**, 37 (2000).

[6] A. Frumkin and B. Slygin, *Acta Physicochim. U.R.S.S*, **5**, 819 (1936).

[7] D. M. Kolb, M. Przasnyski, and H. Gerischer, *J. Electroanal. Chem.*, **54**, 25 (1974).

[8] H. Ibach, *Physics of Surfaces and Interfaces*, Springer, Amsterdam (2006).

[9] J. Clavilier, R. Faure, G. Guinet, and R. Durand, *J. Electroanal. Chem.*, **107**, 205 (1980).

[10] N. Furuya and S. Koide, *Surf. Sci.*, **220**, 18 (1989).

[11] F. Calle-Vallejo, J. Tymoczko, V. Colic, Q. Huy Vu, M. D. Pohl, K. Morgenstern, D. Loffreda, P. Sautet, W. Schuhmann, and A. S. Bandarenka, *Science*, **350**, 185 (2015).

[12] C. L. Scortichini and C. N. Reilley, *J. Electroanal. Chem.*, **139**, 233 (1982); C. L. Scortichini and C. N. Reilley, *J. Electroanal. Chem.*, **139**, 247 (1982).

[13] D. Armand and J. Clavilier, *J. Electroanal. Chem.*, **225**, 205 (1987); D. Armand and J. Clavilier, *J. Electroanal. Chem.*, **233**, 251 (1987).

[14] P. N. Ross, *Surf. Sci.*, **102**, 463 (1981).

[15] J. Clavilier, D. Armand, S. G. Sun, and M. Petit, *J. Electroanal. Chem.*, **205**, 267 (1986).

[16] S. Motoo and N. Furuya, *Ber. Bunsenges. Phys. Chem.*, **91**, 457 (1987).

[17] I. T. McCrum, X. Chen, K. A. Schwarz, M. J. Janik, and M. T. M. Koper, *J. Phys. Chem. C*, **122**, 16756 (2018).

[18] R. Rizo, J. Fernández-Vidal, L. J. Hardwick, G. A. Attard, F. J. Vidal-Iglesias, V. Climent, E. Herrero, and J. M. Feliu, *Nat. Commun.*, **13**, 2550 (2022).

[19] A. M. Gómez-Marín, J. Clavilier, and J. M. Feliu, *J. Electroanal. Chem.*, **688**, 360 (2013).

[20] H. Javed, A. Knop-Gericke, and R. V. Mom, *ACS Appl. Mater. Interfaces*, **14**, 36238 (2022).

[21] M. A. H. Lanyon and B. M. W. Trapnell, *Proc. R. Soc. A.*, **227**, 387 (1955).

[22] A. K. N. Reddy, M. A. Genshaw, and J. O. Bockris, *J. Chem. Phys.*, **48**, 671 (1968).

[23] K. J. Vetter and J. W. Schultze, *J. Electroanal. Chem.*, **34**, 141 (1972).

[24] B. V. Tilak, B. E. Conway, and H. Angerstein-Kozlowska, *J. Electroanal. Chem.*, **48**, 1 (1973).

[25] G. Jerkiewicz, G. Vatankhah, J. Lessard, M. P. Soriaga, and Y. Park, *Electrochim. Acta*, **49**, 1451 (2004).

[26] L. Jacobse, V. Vonk, I. T. McCrum, C. Seitz, M. T. M. Koper, M. J. Rost, and A. Stierle, *Electrochim. Acta*, **407**, 139881 (2022).

[27] M. J. Rost, *J. Electrochem. Soc.*, **170**, 012504 (2023).

[28] H. Angerstein-Kozlowska, B. E. Conway, and W. B. A. Sharp, *J. Electroanal. Chem.*, **43**, 9 (1973).

[29] A. Björling, E. Ahlberg, and J. M. Feliu, *Electrochem. Commun.*, **12**, 359 (2010).

[30] A. Björling, E. Herrero, and J. M. Feliu, *J. Phys. Chem.*, **115**, 15509 (2011).

[31] J. K. Nørskov, J. Rossmeisl, A. Logadottir, L. Lindqvist, J. R. Kitchin, T. Bligaard, and H. Jónsson, *J. Phys. Chem. B*, **108**, 17886 (2004).

[32] N. Hoshi, M. Nakamura, and A. Hitotsuyanagi, *Electrochim. Acta*, **112**, 899 (2013).

[33] A. S. Bandarenka, H. A. Hansen, J. Rossmeisl, and I. E. L. Stephens, *Phys. Chem. Chem. Phys.*, **16**, 13625 (2014).

[34] T. Iwasita, *Electrochim. Acta*, **47**, 3663 (2002).

[35] A. A. Topalov, S. Cherevko, A. R. Zeradjanin, J. C. Meier, I. Katsounaros, and K. J. J. Mayrhofer, *Chem. Sci.*, **5**, 631 (2014).

[36] D. J. S. Sandbeck, M. Inaba, J. Quinson, J. Bucher, A. Zana, M. Arenz, and S. Cherevko, *ACS Appl. Mater. Interfaces*, **12**, 25718 (2020).

[37] T. Michely and J. Krug, *Islands, Mounds and Atoms*, Springer, Amsterdam (2004).

[38] E. Hahn, H. Schief, V. Marsico, A. Fricke, and K. Kern, *Phys. Rev. Lett.*, **72**, 3378 (1994).

[39] J. G. Wang, W. X. Li, M. Borg, J. Gustafson, A. Mikkelsen, T. M. Pedersen, E. Lundgren, J. Weissenrieder, J. Klikovits, M. Schmid, B. Hammer, and J. N. Andersen, *Phys. Rev. Lett.*, **95**, 256102 (2005).

[40] J. Bandlow, P. Kaghazchi, and T. Jacob, *Phys. Rev. B*, **83**, 174107 (2011).

[41] D. Fantauzzi, J. Bandlow, L. Sabo, J. E. Mueller, A. C. T. van Duin, and T. Jacob, *Phys. Chem. Chem. Phys.*, **16**, 23118 (2014).

[42] A. Farkas, D. Fantauzzi, J. E. Mueller, T. Zhu, C. Papp, H. Steinrück, and T. Jacob, *J. Electron Spectrosc. Relat. Phenom.*, **221**, 44 (2017).

[43] A. M. Gómez-Marín and J. M. Feliu, *Surf. Sci.*, **646**, 269 (2016).

[44] J. Clavilier, K. El Achi, and A. Rodes, *J. Electroanal. Chem.*, **272**, 253 (1989).

[45] J. Clavilier, K. El Achi, and A. Rodes, *Chem. Phys.*, **141**, 1 (1990).

4

[46] A. Rodes, K. El Achi, M. A. Zamakhchari, and J. Clavilier, *J. Electroanal. Chem.*, **284**, 245 (1990).

[47] S. Taguchi and J. M. Feliu, *Electrochim. Acta*, **52**, 6023 (2007).

[48] M. T. M. Koper and J. J. Lukkien, *J. Electroanal. Chem.*, **485**, 161 (2000).

[49] A. M. Gómez-Marín and J. M. Feliu, *Electrochim. Acta.*, **104**, 367 (2013).

[50] T. Fuchs, V. Briega-Martos, J. O. Fehrs, C. Qiu, M. Mirolo, C. Yuan, S. Cherevko, J. Drnec, O. M. Magnussen, and D. A. Harrington, *J. Phys. Chem. Lett.*, **14**, 3589 (2023).

[51] F. Valls Mascaró, I. T. McCrum, M. T. M. Koper, and M. J. Rost, *J. Electrochem. Soc.*, **169**, 112506 (2022).

[52] M. J. Kolb, F. Calle-Vallejo, L. B. F. Juurlink, and M. T. M. Koper, *J. Chem. Phys.*, **140**, 134708 (2014).

[53] M. Wakisaka, H. Suzuki, S. Mitsui, H. Uchida, and M. Watanabe, *Langmuir*, **25**, 1897 (2009).

[54] H. You, D. J. Zurawski, Z. Nagy, and R. M. Yonco, *J. Chem. Phys.*, **100**, 4699 (1994).

[55] Y. Liu, A. Barbour, V. Komanicky, and H. You, *J. Phys. Chem. C*, **120**, 16174 (2016).

[56] J. Drnec, M. Ruge, F. Reikowski, B. Rahn, F. Carlà, R. Felici, J. Stettner, O. M. Magnussen, and D. A. Harrington, *Electrochim. Acta*, **224**, 220 (2017).

[57] M. Ruge, J. Drnec, B. Rahn, F. Reikowski, D. A. Harrington, F. Carlà, R. Felici, J. Stettner, and O. M. Magnussen, *J. Electrochem. Soc.*, **164**, H608 (2017).

[58] M. J. Rost, L. Jacobse, and M. T. M. Koper, *Angew. Chem. Int. Ed.*, **62**, e202216376 (2023).

[59] R. Smoluchowski, *Phys. Rev.*, **60**, 661 (1941).

[60] K. H. Lau and W. Kohn, *Surf. Sci.*, **65**, 607 (1977).

[61] V. I. Marchenko and A. Ya. Parshin, *Sov. Phys. JETP*, **52**, 129 (1980).

[62] S. Hanselman, I. T. McCrum, M. J. Rost, and M. T. M. Koper, *Phys. Chem. Chem. Phys.*, **22**, 10634 (2020).

[63] L. Jacobse, Y. F. Huang, M. T. M. Koper, and M. J. Rost, *Nat. Mater.*, **17**, 277 (2018).

[64] L. Jacobse, M. J. Rost, and M. T. M. Koper, *ACS Cent. Sci.*, **5**, 1920 (2019).

[65] M. J. Rost, L. Jacobse, and M. T. M. Koper, *Nat. Commun.*, **10**, 5233 (2019).

[66] B. Love, K. Seto, and J. Lipkowski, *J. Electroanal. Chem.*, **199**, 219 (1986).

[67] K. J. P. Schouten, M. J. T. C. van der Niet, and M. T. M. Koper, *Phys. Chem. Chem. Phys.*, **12**, 15217 (2010).

[68] M. T. M. Koper, J. J. Lukkien, N. P. Lebedeva, J. M. Feliu, and R. A. van Santen, *Surf. Sci.*, **478**, L339 (2001).

[69] M. J. T. C. van der Niet, N. Garcia-Araez, J. Hernández, J. M. Feliu, and M. T. M. Koper, *Catal. Today*, **202**, 105 (2013).

[70] N. García-Aráez, V. Climent, and J. M. Feliu, *Electrochim. Acta*, **54**, 966 (2009).

[71] I. T. McCrum and M. J. Janik, *ChemElectroChem*, **3**, 1609 (2016).

[72] X. Chen, I. T. McCrum, K. A. Schwarz, M. J. Janik, and M. T. M. Koper, *Angew. Chem. Int. Ed.*, **56**, 15025 (2017).

[73] I. T. McCrum and M. J. Janik, *J. Phys. Chem. C*, **121**, 6237 (2017).

[74] N. M. Marković, T. J. Schmidt, B. N. Grgur, H. A. Gasteiger, R. J. Behm, and P. N. Ross, *J. Phys. Chem.*, **103**, 8568 (1999).

[75] A. Zolfaghari, M. Chayer, and G. Jerkiewicz, *J. Electrochem. Soc.*, **144**, 3034 (1997).

[76] R. Gómez, J. M. Orts, B. Álvarez-Ruiz, and J. M. Feliu, *J. Phys. Chem. B*, **108**, 228 (2004).

[77] N. Garcia-Araez, V. Climent, and J. M. Feliu, *J. Electroanal. Chem.*, **649**, 69 (2010).

[78] E. Laviron, *J. Electroanal. Chem.*, **100**, 263 (1979).

[79] J. Solla-Gullón, P. Rodríguez, E. Herrero, A. Aldaz, and J. M. Feliu, *Phys. Chem. Chem. Phys.*, **10**, 1359 (2008).

[80] M. A. van Spronsen, J. W. M. Frenken, and I. M. N. Groot, *Nat. Commun.*, **8**, 429 (2017).

[81] D. Boden, I. M. N. Groot, and J. Meyer, *J. Phys. Chem. C*, **126**, 20020 (2022).

[82] P. J. Feibelman, S. Esch, and T. Michely, *Phys. Rev. Lett.*, **77**, 2257 (1996).

[83] K. Mortensen, C. Klink, F. Jensen, F. Besenbacher, and I. Stensgaard, *Surf. Sci.*, **220**, L701 (1989).

[84] I. T. McCrum, C. J. Bondue, and M. T. M. Koper, *J. Phys. Chem. Lett.*, **10**, 6842 (2019).

[85] Z. Zhu, F. F. Tao, F. Zheng, R. Chang, Y. Li, L. Heinke, Z. Liu, M. Salmeron, and G. A. Somorjai, *Nano Lett.*, **12**, 1491 (2012).

[86] Z. Zhu, G. Melaet, S. Axnanda, S. Alayoglu, Z. Liu, M. Salmeron, and G. A. Somorjai, *J. Am. Chem. Soc.*, **135**, 12560 (2013).

[87] A. Björling and J. M. Feliu, *J. Electroanal. Chem.*, **662**, 17 (2011).

[88] F. Valls Mascaró, M. T. M. Koper, and M. J. Rost, in preparation.

[89] S. Helveg, H. T. Lorensen, S. Horch, E. Lægsgaard, I. Stensgaard, K. W. Jacobsen, J. K. Nørskov, and F. Besenbacher, *Surf. Sci.*, **430**, L533 (1999).

[90] J. Xu, W. Xie, Y. Han, and P. Hu, *ACS Catal.*, **12**, 14812 (2022).

[91] N. Fukaya, H. Murata, M. Shibata, and R. Jinnouchi, *Electrochim. Acta*, **464**, 142867 (2023).

A Supplementary Information on Chapter 2

A.1 Chemical Potential of Adatoms

The total chemical potential of the surface μ_s is the sum of all the contributions from the different surface species: adatoms, step adatoms, kink atoms, step atoms, etc:

$$\mu_s = \mu_{ad} + \mu_{step\,adatom} + \mu_{kink} + \mu_{step} + \dots \tag{A.1}$$

In thermodynamic equilibrium, μ_s is equal to the equilibrium chemical potential, and the local chemical potentials of each of the surface entities described above pursue to balance their difference. Based on Fick's laws, this is achieved by e.g. transport of atoms from a kink site to the terrace, thereby increasing the adatom concentration.

In this work, we are interested in calculating the equilibrium adatom concentration at different electrode potentials, and comparing them to the actual adatom concentrations to know whether nucleation is thermodynamically favorable. Therefore, we are interested specifically in the term μ_{ad}.

In the Adatom Lattice Gas model, the adatoms reside in defined specific sites on the surface, thus forming a lattice gas. If we assume that the adatoms in the lattice gas do not interact between each other, then μ_{ad} can be derived from Fermi-statistics, yielding [1]:

$$\mu_{ad} = \mu_0 + k_B\,T\ln(\tfrac{\theta_{ad}}{1-\theta_{ad}}) \tag{A.2}$$

where μ_0 is the ground state energy of an adatom, which is equal to the formation energy of an adatom (E_{ad}) referenced to the energy of a kink, k_B is the Boltzmann constant, and T is the temperature. The term $k_B\ln(\tfrac{\theta_{ad}}{1-\theta_{ad}})$ describes the entropy. We could also include attractive/repulsive interactions by adding the term $W(\theta_{ad})$ to eq. A.2. However, it has been shown with STM on Cu(111) that this interaction energy is in the order of meV at low adatom concentrations, and therefore one typically neglects this term [2].

At thermodynamic equilibrium, $\mu_{ad} = \mu_{kink}$, and therefore we can solve eq. A.2 for the equilibrium adatom concentration ($\theta_{eq,ad}$):

$$\theta_{eq,ad} = \frac{exp(\frac{-E_{ad}}{k_B T})}{1 + exp(\frac{-E_{ad}}{k_B T})} \tag{A.3}$$

At low adatom coverages, the entropy term in eq. A.2 can be approximated to

$$\frac{\partial S}{\partial N_{ad}} = k_B \ln(\frac{\theta_{ad}}{1-\theta_{ad}}) \approx k_B \ln(\theta_{ad}) \tag{A.4}$$

and hence

$$\mu_{ad} \approx \mu_0 + k_B T \ln(\theta_{ad}) \tag{A.5}$$

The adatom concentration is then described by the well known Boltzmann equation:

$$\theta_{ad} = exp(\frac{-E_{ad}}{k_B T}) \tag{A.6}$$

In Fig. A.1, we evaluate the relative error made at different potentials, thus different PtO_2-adatom equilibrium concentrations ($\theta_{eq,ad}$), when taking the approximation in the entropy term. We define the error as:

$$Error = \left|\theta_{eq,ad} (eq. A.3) - \theta_{eq,ad} (eq. A.6)\right| \tag{A.7}$$

and the relative error as:

$$Relative\,Error = \frac{\left|\theta_{eq,ad} (eq. A.3) - \theta_{eq,ad} (eq. A.6)\right|}{\theta_{eq,ad} (eq. A.6)} \tag{A.8}$$

Note that this relative error is very low ($< 6 \cdot 10^{-4}$) at potentials up to 0.85 V. Therefore, the Boltzmann equation describes the equilibrium adatom concentration sufficiently correct up to 0.85 V, but we need the full entropy expression to calculate $\theta_{eq,ad}$ at higher potentials.

A.2   Adatom Latice Gas Model

As explained above, in the Adatom Lattice Gas model the adatoms are adsorbed at defined surface sites on the terrace. The entropy S is given by [3, 4]:

$$S = k_B \, ln(\Omega) \tag{A.9}$$

where Ω is the number of different configurations in which the adatoms can be placed. For N_{ad} number of adatoms on a terrace with N_s number of sites,

$$\Omega = \frac{N_s!}{N_{ad}!(N_s - N_{ad})!} \tag{A.10}$$

and by using the Stirling approximation $ln(n!) = n\,ln(n) - n$,

$$\Omega = (N_s\,ln(N_s) - N_s) - (N_{ad}\,ln(N_{ad}) - N_{ad}) - (N_s - N_{ad})\,ln(N_s - N_{ad}) + (N_s - N_{ad}) \tag{A.11}$$

Solving the partial derivative on S in eq. A.9 leads to:

$$-T\frac{\partial S}{\partial N_{ad}} = -k_B\,T\,ln(\frac{N_s - N_{ad}}{N_{ad}}) \tag{A.12}$$

Defining then the adatom coverage as $\theta_{ad} = \frac{N_{ad}}{N_s}$, we finally obtain

$$-T\frac{\partial S}{\partial N_{ad}} = -k_B\,T\,ln(\frac{\theta_{ad}}{1-\theta_{ad}}) \tag{A.13}$$
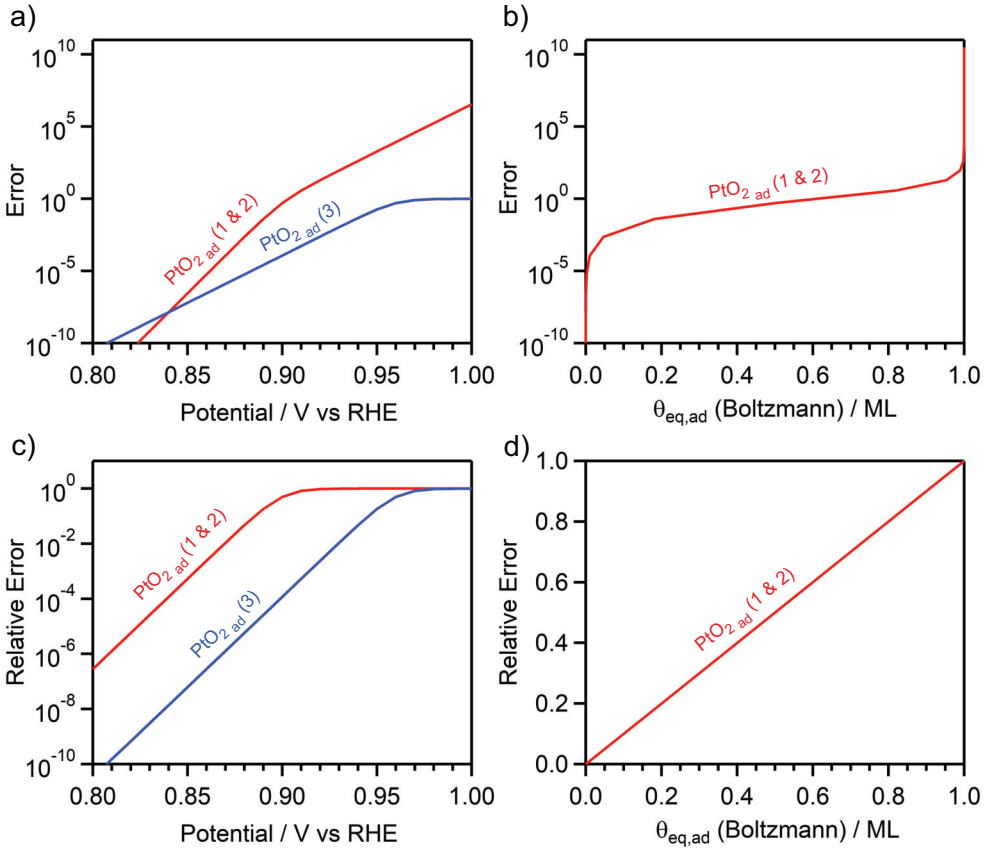
Figure A.1: Error made when calculating the PtO$_2$-adatom equilibrium concentrations with the Boltzmann approximation in the entropy term. **(a)** and **(b)** are the absolute erors, versus potential and coverage (calculated with eq. A.6), respectively, while **(c)** and **(d)** are the relative errors. In **(b)** and **(d)**, we show only the error for $\theta_{eq,PtO_2,ad}$ (1&2), as the error for $\theta_{eq,PtO_2,ad}$ (3), when represented versus coverage, is exactly the same.

Realize that this entropy term is also included in the Langmuir isotherm. However, there is one major difference between the Adatom Lattice Gas model and the Langmuir isotherm: while the isotherm considers atoms/molecules from a liquid or gas phase adsorbing on a solid phase, in the Adatom Lattice Gas model the atoms adsorbed on the surface are the adatoms, which are formed from kinks at the steps. As a kink site repeats itself after removing a kink atom (i.e. thus forming an adatom), the reservoir of kinks is infinite.

A.3   Energy of Oxygen Adsorption as Function of Coverage
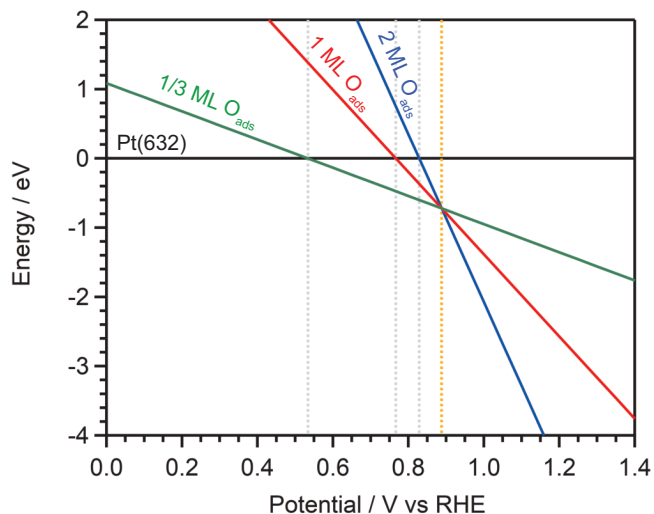
Figure A.2: Gibbs Free Energy for Oxygen Adsorption as a Function of Oxygen Coverage along the Step. The reference used is the energy of a Pt(632) surface, in black. The dotted gray lines indicate the potentials at which each of the oxygen adsorption energies considered crosses zero, while the yellow line indicates the potential at which the three adsorption energies are equal.

A.4 STM Images and Statistical Analysis of the Dendritic Islands
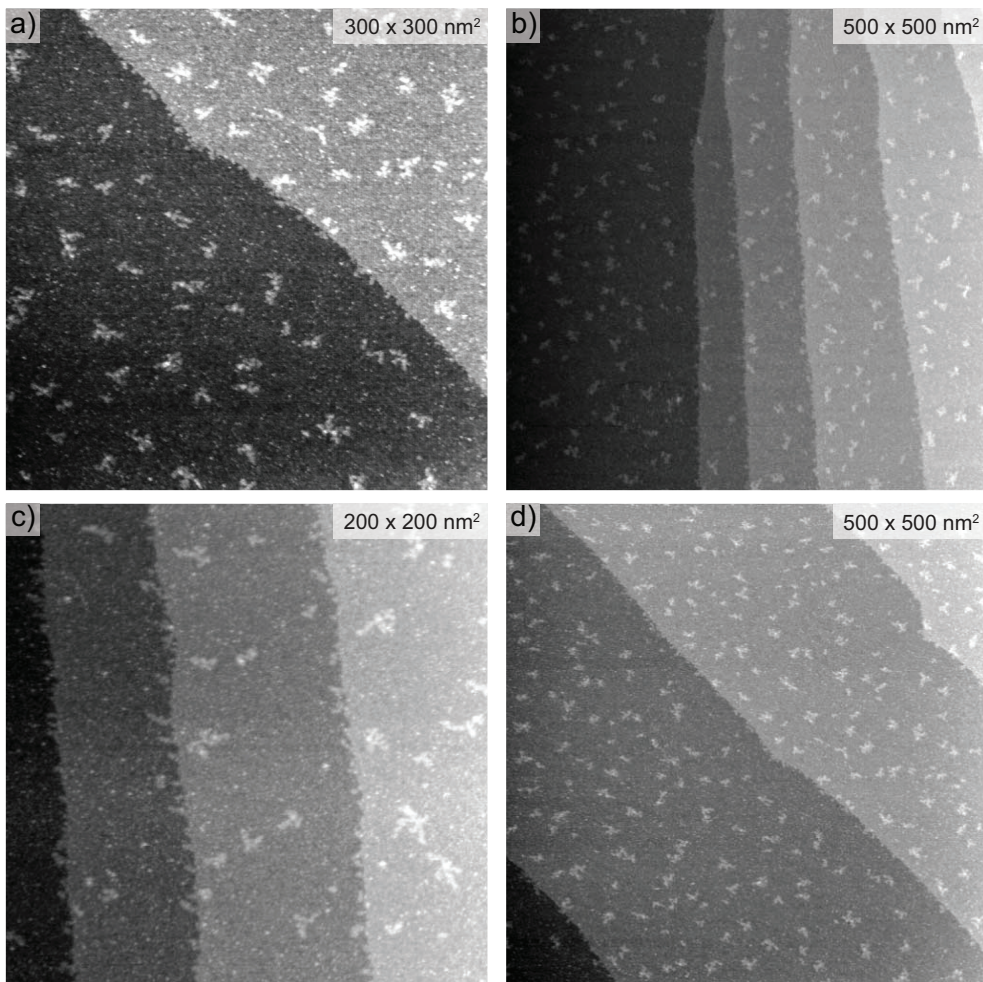
Figure A.3: Vacuum-STM Images of Dendritic Islands on Pt(111). The islands were formed after a potential step from 1.0 V to 1.3 V, where the potential was hold for 10 s, and then stepping back to 1.0 V before finally sweeping to 0.05 V at 50 mV/s. The four images were used to perform the statistical analysis of the island shape that is described in the main text for the measurement in vacuum. The images are reproduced with permission from T. Maagaard.
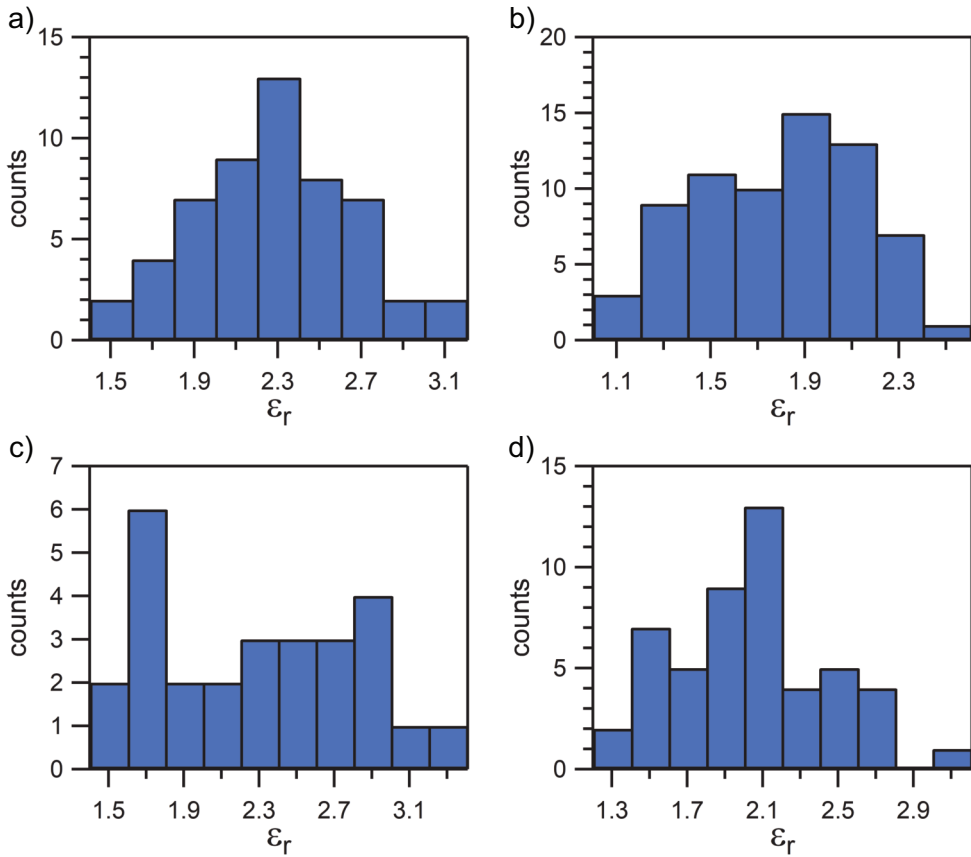
Figure A.4: Statistical Distribution of ϵ_r for the Best Estimate of the Island Shapes Measured in Vacuum. We obtained each of the histograms from analyzing the islands in the according images presented in Fig. A.3, e.g. Fig. A.4a was obtained from analyzing the islands in Fig. A.3a. Merging these four histograms into one results in the statistical distribution shown in Fig. 2.8a
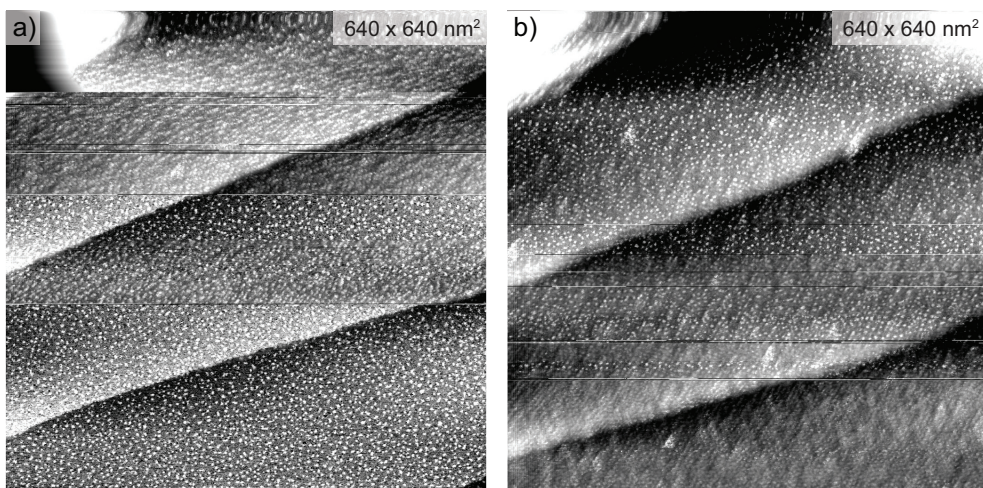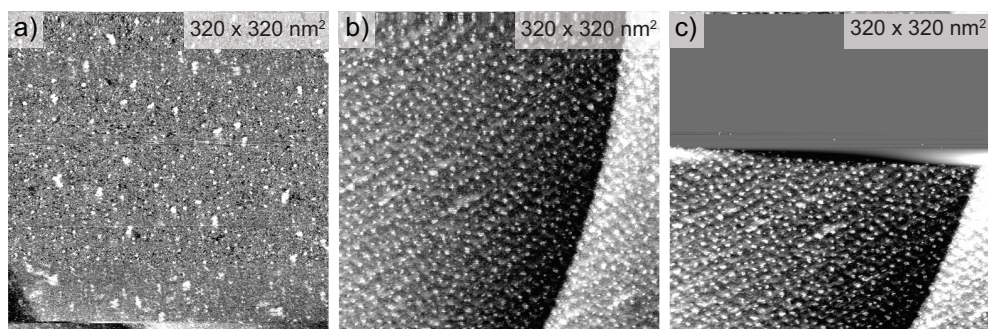
Figure A.5: EC-STM Images of Dendritic Islands on Pt(111). The islands were formed after holding the potential at 1.35 V during 200 s, and then reducing to 0.3 V with 25 mV/s. The two images were used to perform the statistical analysis of the island shape that is described in the main text for the measurement in electrolyte.
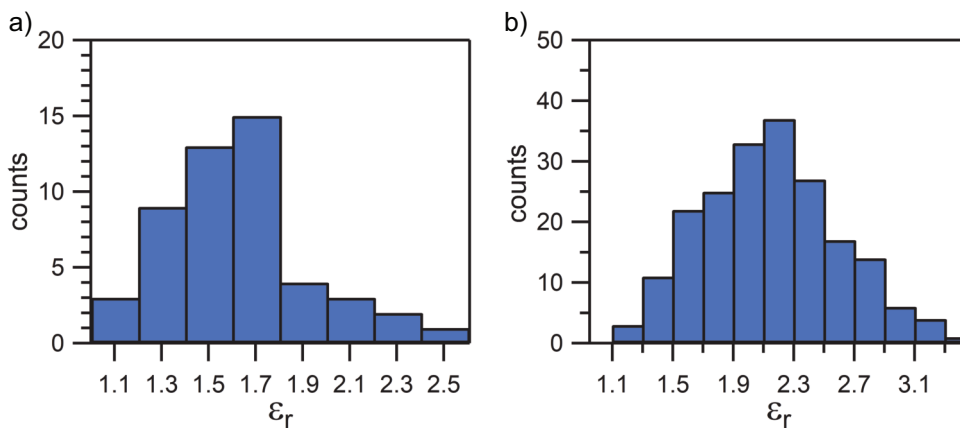
Figure A.6: Statistical Distribution of ϵ_r for the Best Estimate of the Island Shapes Measured in the Electrolyte. We obtained each of the histograms from analyzing the islands in the according images presented in Fig. A.5, e. g. Fig. A.6a was obtained from analyzing the islands in Fig. A.5a. Merging these two histograms into one results in the statistical distribution shown in Fig. 2.8b.

Figure A.7: EC-STM Images of Dendritic Islands Formed on Pt(111) upon Oxidation-Reduction Cycling. The islands were formed after 1 (**a**), 6 (**b**), and 7 (**c**) oxidation-reduction cycles from 0.06 V to 1.35 V at 50 mV/s. The three images were used to perform the statistical analysis of the island shape that results in the histograms shown in Fig. 2.10.

References

[1] H. Ibach, *Physics of Surfaces and Interfaces*, Springer, Amsterdam (2006).

[2] J. Repp, F. Moresco, G. Meyer, K. H. Rieder, P. Hyldgaard, and M. Persson, *Phys. Rev. Lett.*, **85**(14), 2981 (2000).

[3] T. Hill, *An Introduction to Statistical Thermodynamics*, Addison-Wesley Publishing Company, Reading (1960).

[4] A. Saedi, and M. J. Rost, *Nat. Commun.*, **7**, 10733 (2015).

A

B Supplementary Information on Chapter 3

B.1 EC-STM Image Processing

Figure B.1a shows a 48x48 nm^2 raw EC-STM image of a Pt(554) surface, obtained at U_s = 0.1 V and U_t = 0.15 V. Due to the tilt of the sample, which even pushes the contrast out of the color scale at the upper left and the lower right of the image, the atomic steps are barely visible. Therefore, we performed a planar background subtraction of the image, which enhances the contrast on the surface features (Fig. B.1b). However, this image is inadequate for a proper analysis, as it does not reflect the natural tilt of the stepped surface. We need to rotate the image along the axis parallel to the step direction until the steps have the expected mono-atomic step height (2.27 Å), which is similar to aligning the terraces fully in-plane without any slope. The height line (in orange) should, in this case, reveal a series of descending and flat sections, resembling a staircase. Figure B.1c shows the same height line for three different rotation angles. For each of them, we measured the average step height, which we plotted in Fig. B.1d. Finally, we determined the correct rotation angle from the linear regression shown in the graph, setting X = 2.27 Å. This delivers α = 5.68°, which is very close to the miscut angle of Pt(554) with respect to the (111) plane of 5.77°. However, this does not necessarily have to be the case for all images or height lines, as the surface can present, locally, areas with more or less tilt, i. e. step density. In general, this also depends on the mounting of the sample in the sample holder as well as the different lengths of the micrometer screws that are used for the coarse approach. To avoid an inaccurate analysis, we performed the above described procedure for all height lines, and not only for Pt(554), but also for Pt(553). However, as the latter has bunched steps with higher multiplicity, we took this into account by expecting step heights close to 2.27 Å, 4.54 Å, or 6.81 Å. Note that the steps are not vertical in Fig. B.1c, even not with correct rotation, which is due to the tip convolution with the step structure.
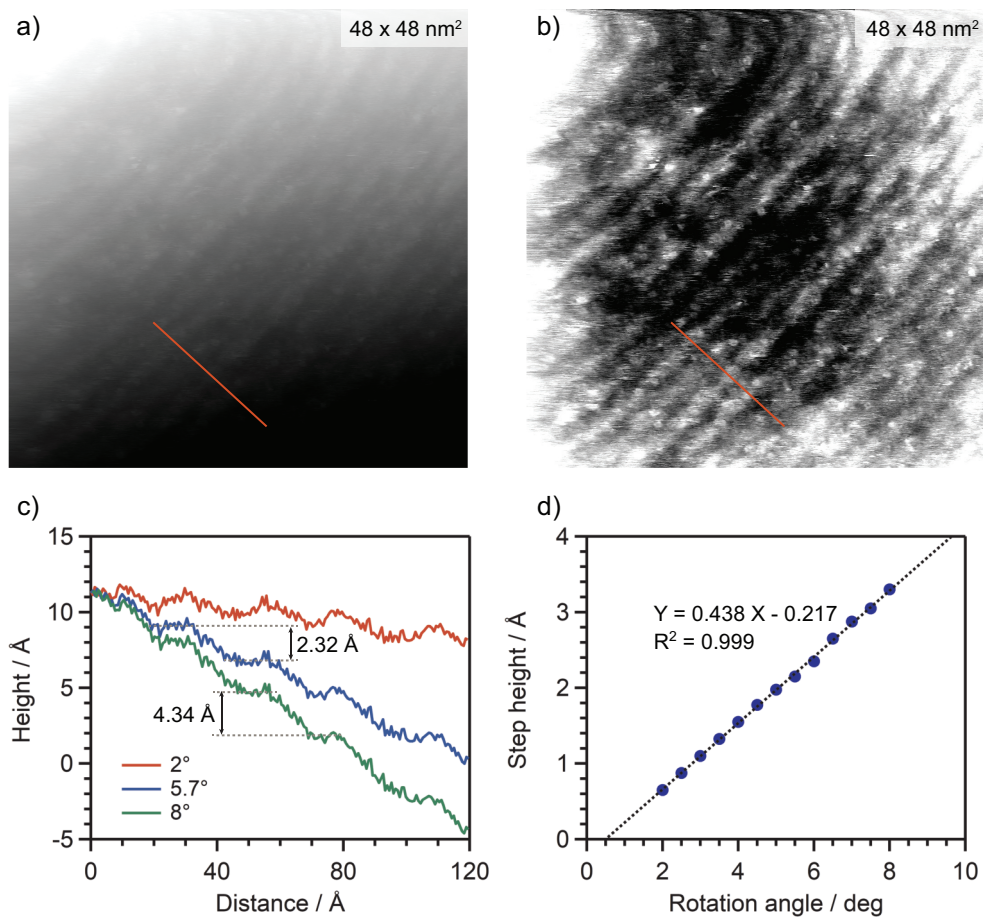
Figure B.1: EC-STM Image Processing to Extract Accurate Step Heights. **(a)** Raw EC-STM image (48x48 nm^2) of a Pt(554) surface, obtained at U_s = 0.1 V and U_t = 0.15 V. **(b)** Same image after planar background subtraction enhancing the contrast. **(c)** Height lines at the indicated position in (a) and (b) with different rotation angles: 2°, 5.7°, and 8°. **(d)** Average step height versus the rotation angle of the height line to determine the best correction angle.

B.2 EC-STM Images of Pt(554) and Pt(553)

Figures B.2 and B.3 show all the EC-STM images used for the analysis of the terrace width and step height distributions. In order to enhance the contrast of the surface features, here we show the images after applying a line-by-line background subtraction. For the actual analysis, we processed the images as explained above.

The distortion at the top and sides on (some of) the EC-STM images is due to the creep of the STM piezo-tube at the beginning of every new frame or scan line. In our analysis we avoided these distorted areas, as well as the areas that show contamination.
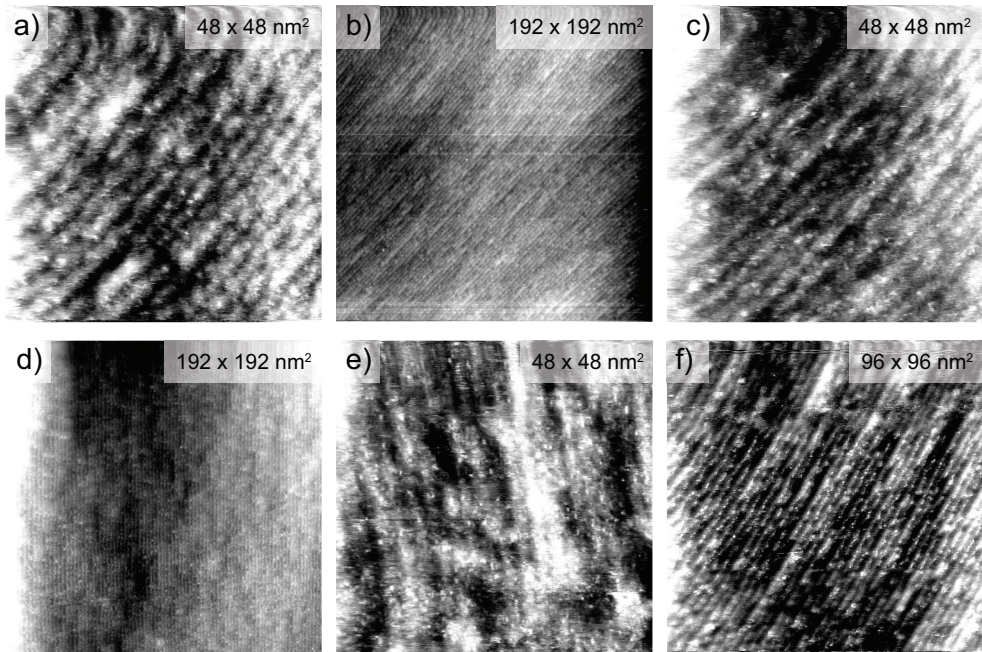
Figure B.2: **EC-STM Images of Pt(554).** We recorded all the images at $U_s = 0.1$ V and either $U_t = 0.15$ V or $U_t = 0.20$ V, with tunneling currents in the range of 300 pA. The corresponding image sizes are indicated.
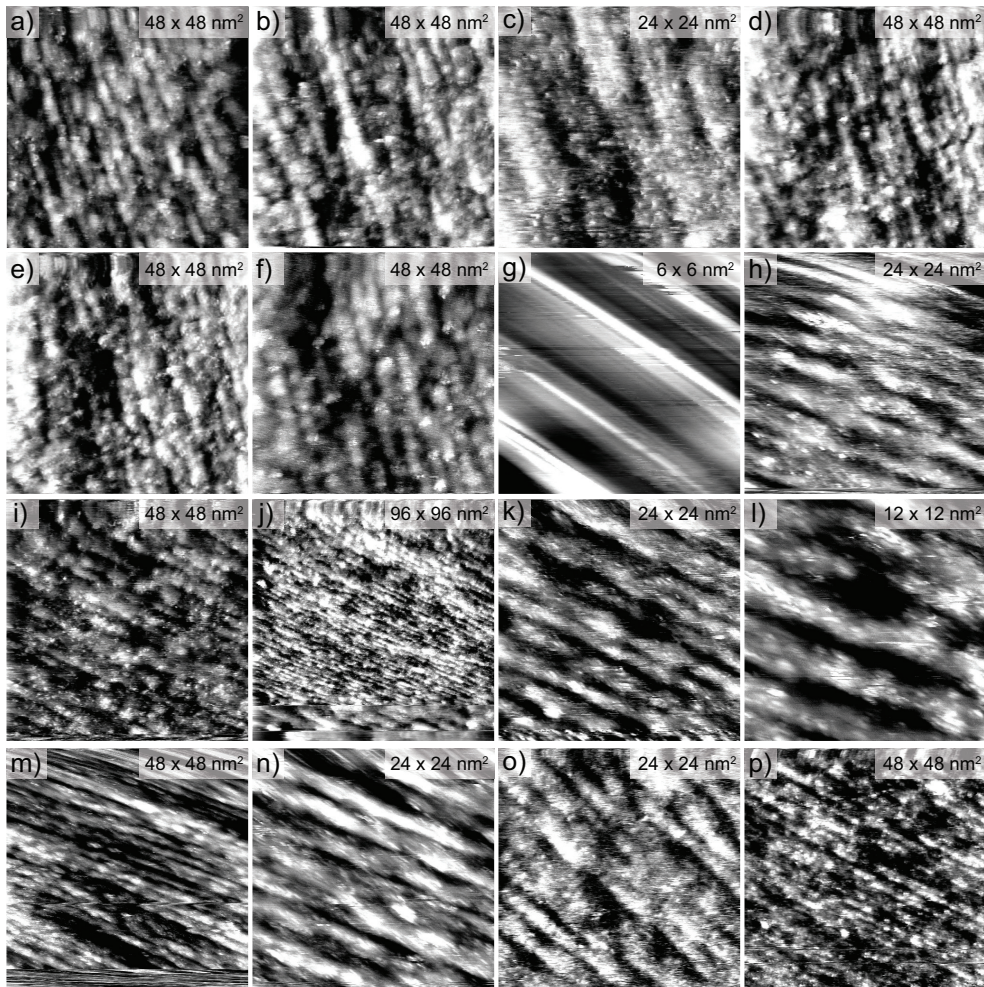
Figure B.3: EC-STM Images of Pt(553). We recorded all the images at $U_s = 0.1$ V and either $U_t = 0.15$ V or $U_t = 0.20$ V, except for **(j)** and **(l)**, which we recorded at $U_s = 0.4$ V and $U_t = 0.45$ V. The tunneling currents were in the range of 300-700 pA except for **(g)**, which was recorded at 1200 pA. The corresponding image sizes are indicated.

B.3 Terrace Width and Step Height Distributions on Pt(553)

Figures B.4 and B.5 show the terrace width and step height distributions for Pt(553) from EC-STM measurements performed on different days, and thus different sample preparation. All the histograms show mainly three different peaks, corresponding to single steps, double steps, and triple steps, as explained in the main article. This proves that the Pt(553) surface, prepared with the flame-annealing method followed by cooling in an Ar-H_2 atmosphere, is always bunched.
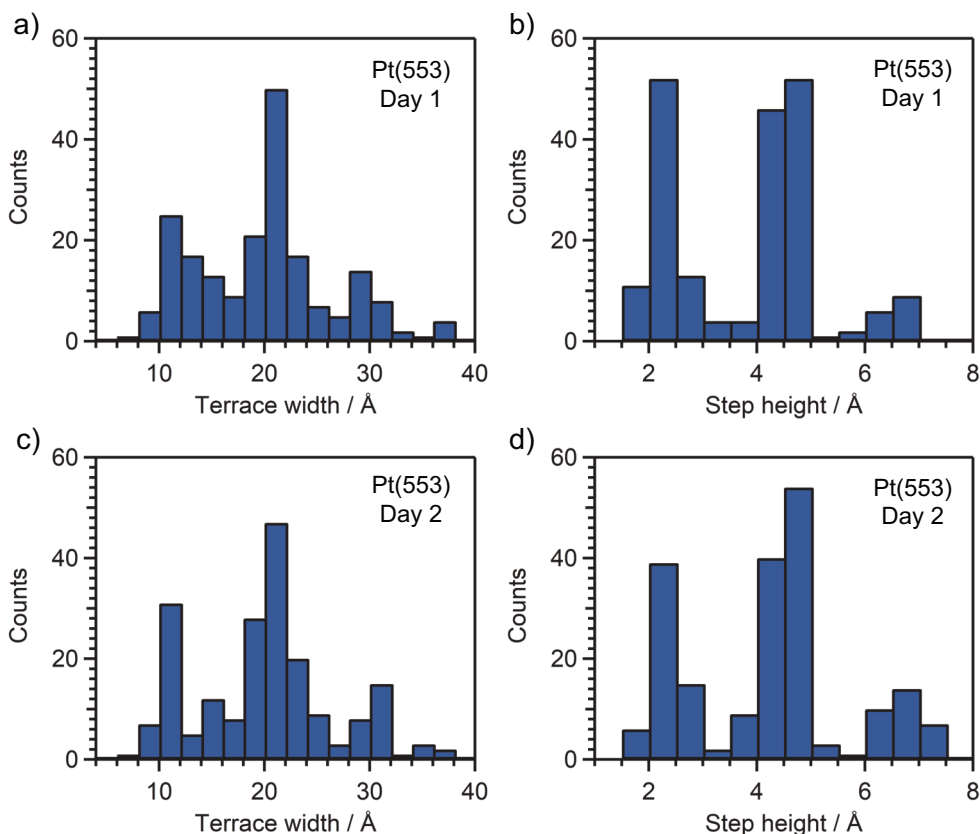
Figure B.4: Terrace Width and Step Height Distributions for Pt(553) on different days. I. Day 1 ((**a**) and (**b**)) corresponds to the EC-STM images (**a**)-(**f**) in Fig. B.3, Day 2 ((**c**) and (**d**)) to images (**h**)-(**j**).
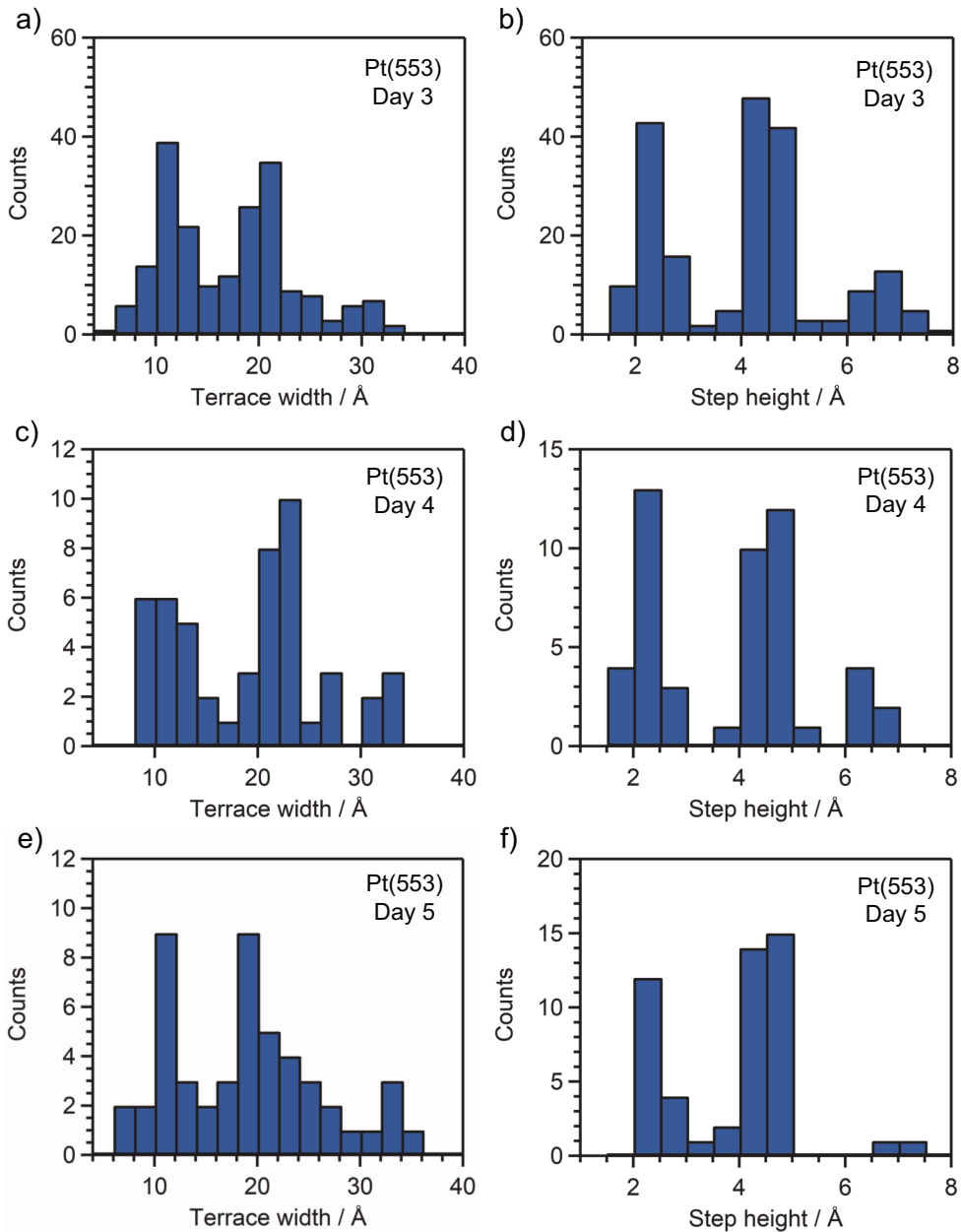
Figure B.5: Terrace Width and Step Height Distributions for Pt(553) on different days. II. Day 3 ((**a**) and (**b**)) corresponds to the EC-STM images shown in Fig. B.3 (**k**)-(**n**), Day 4 ((**c**) and (**d**)) to Fig. B.3 (**o**), and Day 5 ((**e**) and (**f**)) to the one shown in Fig. B.3 (**p**).

B.4 Effect of Potential and Hydrogen Coverage

Fig. B.6 shows one of the EC-STM images on Pt(553) recorded at a sample potential of 0.4 V after holding this potential for 60 minutes (previously it was 0.1 V). The presence of double steps is evident from the height line. As explained in the main manuscript, in the time span evaluated we did not observe a different surface structure when changing the applied potential.
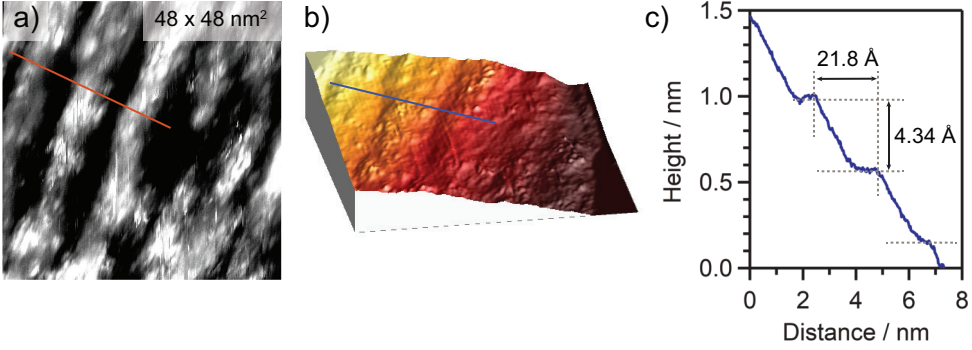
Figure B.6: **EC-STM Image of Pt(553) at 0.4 V. (a)** 2D Image after background subtraction and its corresponding 3D representation **(b)**, recorded at U_s = 0.4 V and U_t = 0.45 V, with a tunneling current in the range of 300 pA. Both images are 48x48 nm^2. **(c)** Height line showing double steps.

B.5 Calculation of the Step-Step Interaction

The step interaction coefficient B_{step} must take into account the entropic repulsion as well as the electrostatic and elastic interactions between neighboring steps. As the latter two go with $U = A/L^2$, where U is the energy per length between steps and A the magnitude of both energetic interactions, B_{step} is given by [1]:

$$B_{step}(T) = \frac{(\pi\, k_B\, T)^2\, a}{24\, \widetilde{\beta}(T)} \left[1 + \sqrt{1 + \frac{4\, A\, \widetilde{\beta}(T)}{(k_B\, T)^2}} \right]^2 \tag{B.1}$$

where $\widetilde{\beta}$ is the step stiffness, which can be calculated from [2]:

$$\widetilde{\beta}(T) = \frac{k_B\, T\, a}{b^2(T)} \tag{B.2}$$

with b being the step diffusivity, which can be obtained from an STM statistical analysis of the mean-squared displacement of an isolated step perpendicular to the step edge. Alternatively, we can calculate b from the kink formation energy f_{kink}, as [2]:

$$b^2(T) = \frac{2\, d\, e^{-f_{kink}/(k_B\, T)}}{1 + 2\, e^{-f_{kink}/(k_B\, T)}} \tag{B.3}$$

where d is the unit vector perpendicular to the step edge. Thus, with equations B.1-3 and taking $A = 2.4$ eV Å from Ref. [1], we can easily determine B_{step} at any given temperature.

In order to obtain the interaction coefficient of double steps, $B_{double\,step}$, we first need to estimate $A_{double\,step}$. As A goes, in general, with the square of the electric (or elastic) dipole moment ($A \propto p_z^2$) [3,4], we can calculate $A_{double\,step}$ from the ratio:

$$\frac{A_{double\,step}}{A_{single\,step}} = \left[\frac{p_{z,double\,step}}{p_{z,single\,step}} \right]^2 \tag{B.4}$$

As we extracted $p_{z,double\,step}$ from Fig. 3.5 in the main manuscript, $A_{double\,step}$ naturally follows, and we can finally use eq. B.1-3 to calculate $B_{double\,step}$.

B.6 Temperature Effect on Step Bunching

The variation of temperature has an effect on the step free energy as well as on the entropic term of the step-step interaction, and hence ultimately on the total free energy of the surface. Figure B.7 shows the free energy ratios between a surface with double steps and one with single steps at different temperatures. As evident from this graph, decreasing the temperature results in an earlier onset for step bunching, from $n = 8$ at $T = 1300$ K to $n = 15$ at $T = 900$ K. The main reason for this is that at lower temperature there is a reduced concentration of thermally-activated kinks that decrease the free energy of the single steps (i. e. on double steps the concentration of thermally-activated kinks is anyhow much smaller due to the higher kink formation energy). This leads to a higher step stiffness and, therefore, single steps are more prone to bunching at lower temperatures.
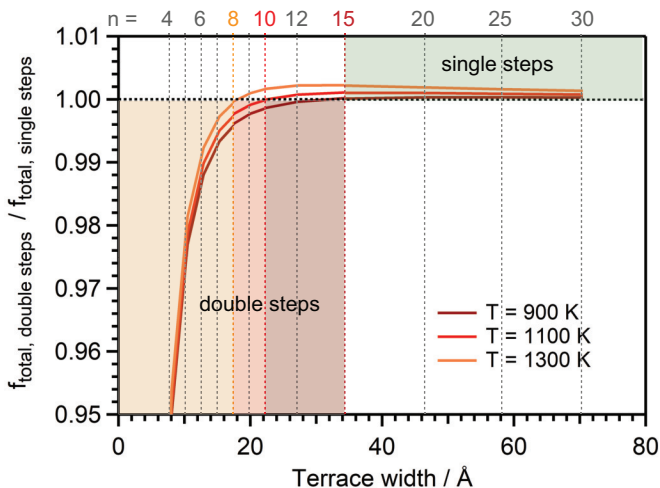

Figure B.7: Effect of Temperature on Step Bunching. Surface energy ratio between configurations with double and with single steps at different temperatures. The vertical colored lines indicate the onset of step bunching (where the curves cross the ratio equal to one) at each of the temperatures evaluated. The regions with stable single steps and stable double steps are indicated.

B.7 Effect of Step Bunching on the Hydrogen Adsorption

In Fig. 3.5 in the main text, we showed that Pt(553) and Pt(221), two stepped surfaces that have bunched steps, present an extra voltammetric peak in the hydrogen desorption region. We assigned this peak to hydrogen desorption and its (partial) replacement with hydroxide at bunched steps, as we discussed in depth in Chapter 4. However, step bunching has also a slight influence on the adsorption/desorption energetics on single steps, as it changes the step separation and thus the repulsion. Figure B.5 shows, for each surface studied, the potential value at the center of the hydrogen single-step peak (E_{H-step}), which is closely related to the adsorption/desorption energy [5]. From Pt(111), which has a very small amount of steps, to Pt(554) E_{H-step} increases, which could be caused by the raising interaction between steps as the terrace width decreases [3, 4, 6, 7]. However, Pt(775) does no longer follow the trend, and jumps back to a much a lower E_{H-step}. This suggests that Pt(775) has also step bunches, although, as we discuss in the main text, the density of single steps must be much higher.
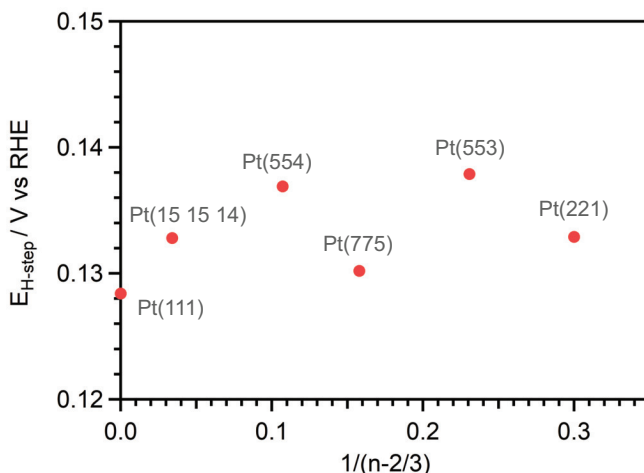

Figure B.8: Potential of the H-step Peak versus the Step Density. The data points correspond to the potential values at the the center of the respective single step peaks in the hydrogen desorption region, which we show in Fig. 3.5 in the main text.

B.8 Stability of Stepped Platinum Surfaces: Literature Study

Although we only performed EC-STM measurements on Pt(554) and Pt(553), we can deduce whether other stepped platinum surfaces are stable from their electrochemical behavior. As we discussed in the main article, stepped surfaces that undergo step bunching present an unexpected E_{pztc} and ORR activity. However, other electrochemical reactions such as CO Oxidation, the Hydrogen Oxidation Reaction (HOR), Hydrogen Peroxide Reduction, and Nitrate Reduction are also affected. Based on this, in Tables B.1-B.3 we assessed the stability of many stepped platinum surfaces in the [1 -1 0], [0 1 -1], and [0 0 1] zones, respectively, all prepared with the flame-annealing method.

(111)x(111)	n	Stable?	Measurements
(15 15 14)	30	Yes	ORR [8], CO Oxidation [9]
(10 10 9)	20	Yes	STM [10]
(554)	10	Yes	ORR [11], H_2O_2 Red. [12], NO_3^- Red. [13], CO Ox. [9], E_{pztc} [14, 15]
(997)	9	Yes	ORR [16], HOR [17]
(775)	7	No	ORR [11, 16], H_2O_2 Ox. [12], NO_3^- Red.* [13], E_{pztc} [14, 15]
(332)	6	No	ORR [11], NO_3^- Red. [13], E_{pztc} [15]
(553)	5	No	H_2O_2 Red. [18], NO_3^- Red. [13], CO Ox. [9], HOR [17], E_{pztc} [14, 15]
(221)	4	No	ORR [11, 16], H_2O_2 Red. [12], NO_3^- Red. [13], E_{pztc} [14, 15]
(331)	3	No	SXRS [19], ORR [11, 16], H_2O_2 Red. [12, 18], NO_3^- Red. [13], E_{pztc} [14, 15]
(110)x(111)	n	Stable?	Measurements
(551)	3	No	CV H_{upd} [20]
(991)	5	No	CV H_{upd} [20]
(19 19 1)	10	No	CV H_{upd} [20]

Table B.1: Stability of Stepped Platinum Surfaces in the [1 -1 0] Zone. This comprises (111) vicinal surfaces with (111) steps and (110) vicinals with (111) steps. The Nitrate Reduction measurement on Pt(775) (marked with an asterisk) suggests that this surface is stable, while the other measurements show the contrary. For all the other surfaces, there is a total agreement between different techniques.

B

(111)x(100)	n	Stable?	Measurements
(15 14 14)	29	Yes	H_2O_2 Red. [12]
(11 10 10)	21	Yes	STM [10]
(15 13 13)	14	Yes	ORR [21]
(11 9 9)	10	Yes	E_{pztc} [22]
(544)	9	Yes	ORR [21], H_2O_2 Red. [12], CV H_{upd} [23]
(755)	6	No	ORR [11, 21], H_2O_2 Red. [12, 18], E_{pztc} [22], CV H_{upd} [23]
(322)	5	No	H_2O_2 Red. [12, 18]
(533)	4	No	ORR [11, 21], E_{pztc} [22], CV H_{upd} [23]
(211)	3	No	ORR [11, 21], H_2O_2 Red. [12, 18], HOR [24], E_{pztc} [22], CV H_{upd} [23]
(311)	2	No	SXRS [19, 25], ORR [11], HOR [24], E_{pztc} [22], CV H_{upd} [23]

(100)x(111)	n	Stable?	Measurements
(511)	3	No	SXRS [19]
(771)	4	Yes	ORR [11], E_{pztc} [26]
(11 1 1)	6	Yes	E_{pztc} [26]
(15 1 1)	8	Yes	ORR [11]
(19 1 1)	10	Yes	E_{pztc} [26]
(29 1 1)	15	Yes	STM [26], E_{pztc} [26]

Table B.2: Stability of Stepped Platinum Surfaces in the [0 1 -1] Zone. This comprises (111) vicinal surfaces with (100) steps and (100) vicinals with (111) steps.

(100)x(110)	n	Stable?	Measurements
(20 1 0)	20	Yes	Co Ox. [27]
(10 1 0)	10	Yes	Co Ox. [27]
(710)	7	Yes	Co Ox. [27]
(510)	5	No	Co Ox. [27]
(310)	3	No	SXRS [28], Co Ox. [27]
(210)	2	No	Co Ox. [27]
(110)x(100)	n	Stable?	Measurements
(320)	3	No	E_{pztc} [29]
(430)	4	No	E_{pztc} [29]
(540)	5	No	E_{pztc} [29]
(760)	7	No	E_{pztc} [29]
(10 9 0)	10	No	E_{pztc} [29]

Table B.3: Stability of Stepped Platinum Surfaces in the [0 0 1] Zone. This comprises (100) vicinal surfaces with (110) steps and (110) vicinals with (100) steps.

References

[1] H. Jeong, E. D. Williams, *Surf. Sci. Rep.*, **34**, 171 (1999).

[2] H. Ibach, *Physics of Surfaces and Interfaces*, Springer, Amsterdam (2006).

[3] C. Jayaprakash, C. Rottman, and W. F. Saam, *Phys. Rev. B*, **30**, 6549 (1984).

[4] V. I. Marchenko and A. Ya. Parshin, *Sov. Phys. JETP*, **52**, 129 (1980).

[5] A. J. Bard and L. R. Faulkner, *Electrochemical Methods: Fundamentals and Applications*, 2nd ed., Wiley, New York (2001).

[6] K. H. Lau and W. Kohn, *Surf. Sci.*, **65**, 607 (1977).

[7] R. Smoluchowski, *Phys. Rev.*, **60**, 661 (1941).

[8] A. M. Gómez-Marín and J. M. Feliu, *Catal. Today*, **244**, 172 (2015).

[9] N. P. Lebedeva, M. T. M. Koper, J. M. Feliu, and R. A. van Santen, *J. Phys. Chem.*, **106**, 12938 (2002).

[10] E. Herrero, J. M. Orts, A. Aldaz, and J. M. Feliu, *Surf. Sci.*, **440**, 259 (1999).

[11] R. Rizo, E. Herrero, and J. M. Feliu, *Phys. Chem. Chem. Phys.*, **15**, 15416 (2013).

[12] R. Rizo, J. M. Feliu, and E. Herrero, *J. Catal.*, **398**, 123 (2021).

[13] S. Taguchi and J. M. Feliu, *Electrochim. Acta*, **52**, 6023 (2007).

[14] V. Climent, R. Gómez, and J. M. Feliu, *Electrochim. Acta*, **45**, 629 (1999).

[15] V. Climent, G. A. Attard, and J. M. Feliu, *J. Electroanal. Chem.*, **532**, 67 (2002).

[16] A. Kuzume, E. Herrero, and J. M. Feliu, *J. Electroanal. Chem.*, **599**, 333 (2007).

[17] N. Hoshi, Y. Asaumi, M. Nakamura, K. Mikita, and R. Kajiwara, *J. Phys. Chem. C*, **113**, 16843 (2009).

[18] E. Sitta, A. M. Gómez-Marín, A. Aldaz, and J. M. Feliu, *Electrochem. Commun.*, **33**, 39 (2013).

[19] N. Hoshi, M. Nakamura, O. Sakata, A. Nakahara, K. Naito, and H. Ogata, *Langmuir*, **27**, 4236 (2011).

[20] J. Souza-Garcia, V. Climent, and J. M. Feliu, *Electrochem. Commun.*, **11**, 1515 (2009).

[21] M. D. Maciá, J. M. Campina, E. Herrero, and J. M. Feliu, *J. Electroanal. Chem.*, **564**, 141 (2004).

[22] R. Gómez, V. Climent, J. M. Feliu, and M. J. Weaver, *J. Phys. Chem. B*, **104**, 597 (2000).

[23] N. Garcá-Aráez, V. Climent, and J. M. Feliu, *Electrochim. Acta*, **54**, 966 (2009).

[24] R. Kajiwara, Y. Asaumi, M. Nakamura, and N. Hoshi, *J. Elecroanal. Chem.*, **657**, 61 (2011).

[25] A. Nakahara, M. Nakamura, K. Sumitani, O. Sakata, and N. Hoshi, *Langmuir*, **23**, 10879 (2007).

[26] K. Domke, E. Herrero, A. Rodes, and J. M. Feliu, *J. Electroanal. Chem.*, **552**, 115 (2003).

[27] F. J. Vidal-Iglesias, J. Solla-Gullón, J. M. Campina, E. Herrero, A. Aldaz, and J. M. Feliu, *Electrochim. Acta*, **54**, 4459 (2009).

[28] N. Hoshi, A. Nakahara, M. Nakamura, K. Sumitani, and O. Sakata, *Electrochim. Acta*, **53**, 6070 (2008).

[29] J. Souza-Garcia, C. A. Angelucci, V. Climent, and J. M. Feliu, *Electrochem. Commun.*, **34**, 291 (2013).

C Supplementary Information on Chapter 4

C.1 Formation Free Energy of Steps

In vacuum, the free energy required to form one unit length of an isolated step, f_{step}, is given by the temperature independent step formation energy, f_{step}^0, and an entropic term that accounts for the thermal fluctuation of steps due to the formation of kinks [1, 2]:

$$f_{step}(T) = f_{step}^0 - \frac{2\,k_B\,T}{a}\,exp(\frac{-f_{kink}^0}{k_B\,T}) \tag{C.1}$$

where a is the unit step length, k_B is the Boltzmann constant, T is the temperature, and f_{kink}^0 is the formation energy of a kink. From this equation, it is evident that the presence of kinks decreases the free energy needed to form the step. Therefore, at any temperature greater than $T = 0$ K, the steps will never be completely straight, but they will present a certain roughness given by the concentration of kinks, which is determined by f_{kink}^0 and T. The higher T or the lower f_{kink}^0, the higher the concentration of kinks and thus the cheaper in energy it is to form a step. Actually, at a certain T, the entropic term becomes large enough to counterbalance f_{step}^0, and hence f_{step} becomes zero.

It is noteworthy to mention also that f_{step}^0 and f_{kink}^0 depend on the step geometry. This is easy to realize for f_{step}^0, as (111) and (100) steps exhibit different microfacets with the lower terrace atoms. The geometric dependence of f_{kink}^0 resides on the fact that creating a kink on a (111) step involves the formation of one unit length of a (100) step, while creating a kink on a (100) step involves the formation of one unit length of a (111) step.

In electrochemistry, however, the thermodynamic description of the step free energy becomes more complicated. Firstly because of the potential applied to the electrode, which adds a term to equation C.1. Secondly, because the species adsorbed at steps and kinks modify both $\eta(0)$ and ϵ_{kink}, and can favor one step geometry over the other (e.g. (100) steps over (111) steps) [3]. Nevertheless, the general concept is the same as in vacuum, and we can ensure that also in electrolyte the steps are not completely straight due to the presence of kinks.
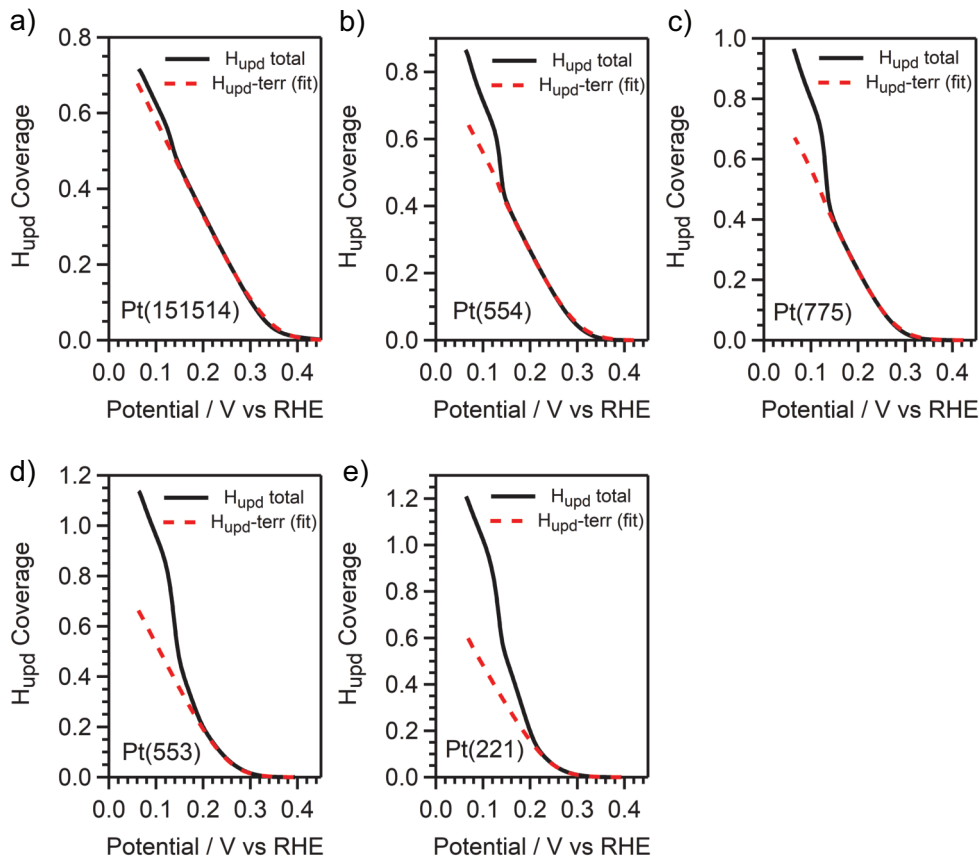
C.2 H_{upd} Coverage

Figure C.1: Comparison of Total and Terrace H_{upd} Coverages. For each of the stepped surfaces studied (**a-e**), the H_{upd}-terrace coverage (in red) results from a fit of the terrace peak with the Frumkin isotherm, as explained in the main text. In all the cases the H_{upd}-terrace coverage matches well with the total H_{upd} coverage at potentials more positive than the (111) step peak.
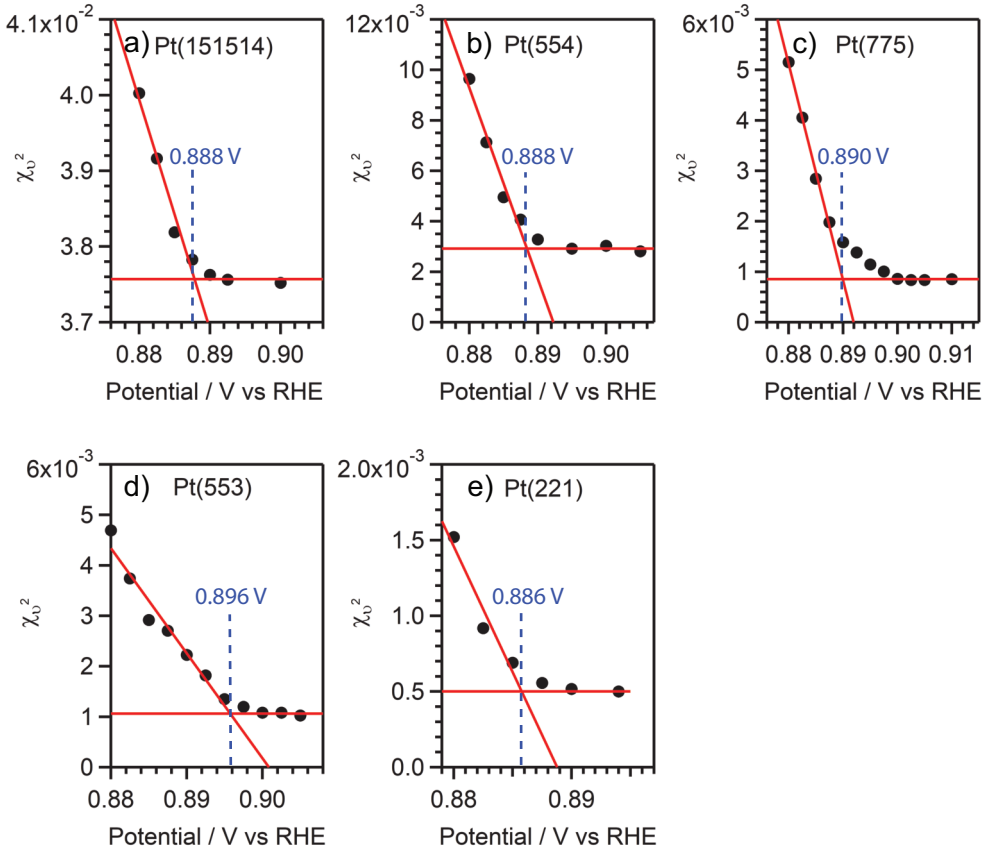
C.3 Potential Limits for the Fitting of the PtOx Region

Figure C.2: Determination of the Lower Potential for Fitting the Platinum Oxidation Region. Normalized Chi Square values obtained from fitting the platinum oxidation region starting at the potentials indicated in the x axes. The upper potential was fixed at 1.09 V. The inflection point in the Normalized Chi Square values (marked with the dashed blue line) gives the lower potential used for the final fit.
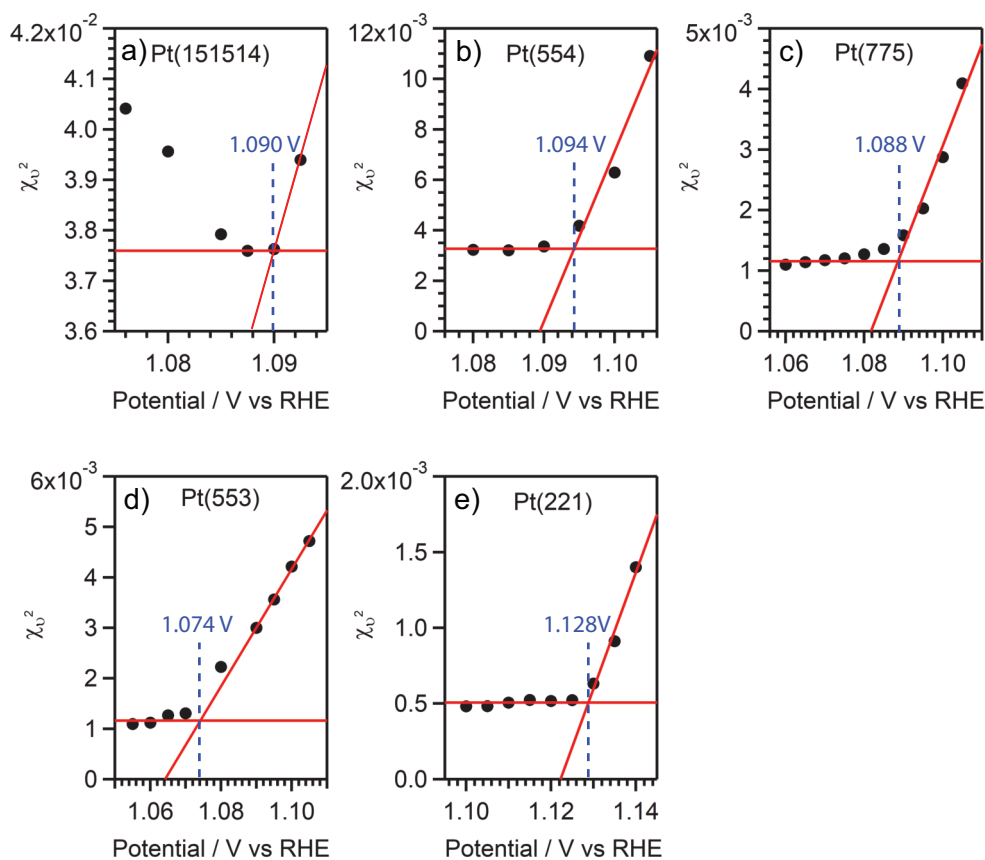
Figure C.3: Determination of the Upper Potential for Fitting the Platinum Oxidation Region. Normalized Chi Square values obtained from fitting the platinum oxidation region up to the potentials indicated in the x axes. The lower potential was fixed at 0.89 V. The inflection point in the Normalized Chi Square values (marked with the dashed blue line) gives the upper potential used for the final fit.

References

[1] H. Ibach, *Physics of Surfaces and Interfaces*, Springer, Amsterdam (2006).

[2] E. D. Williams and N. C. Bartelt, *Science*, **251**, 393 (1991).

[3] M. Kalff, G. Comsa, and T. Michely, *Phys. Rev. Lett.*, **81**, 1255 (1998).

C

Summary

The transition from fossil fuels to renewable energy sources necessitates efficient methods to store the energy generated in order to ensure its availability during periods of high demand and low production. The most effective way to do this is by converting the renewable electricity into chemical energy, which can be achieved by using electrochemical devices such as batteries, electrolysers, and fuel cells. Optimal electrocatalytic materials are key for the development of these technologies, as they enhance the efficiency of the conversion process by minimizing energy losses. However, the best catalysts known to be used in fuel cells are platinum-based, and thus scarce and expensive. Moreover, platinum catalysts degrade upon prolonged usage, which leads to a decrease of their activity and the need to replace the fuel cell. Therefore, it is crucial in electrochemistry to identify those material compositions and geometries that not only satisfy the catalytic requirements, but are also stable for prolonged device longevity. In this thesis, we used an Electrochemical Scanning Tunneling Microscope (EC-STM) to study the (in)stability of platinum electrode surfaces as well as to establish structure-activity relationships at the atomic scale.

In Chapter 2 we used Density Functional Theory (DFT) and EC-STM to expand the previous knowledge on the nucleation and growth of adatom islands on Pt(111) upon oxidation-reduction cycling, a process that mimics the real operation of hydrogen fuel cells and that is linked to the catalyst degradation. Our results showed that the surface oxidation results in the formation of PtO_2-adatoms. However, their actual concentration on the surface is far from reaching their equilibrium concentration, and therefore nucleation into adatom islands is not favored. In addition, we show that at high electrode potentials the mobility of PtO_2-adatoms is severly restricted, not only because their diffusion is inherently slow, but also because these species are trapped in between the oxide rows lifted above the surface. During the cathodic (reverse) scan, the reduction of the surface oxide is followed by the reduction of the PtO_2-adatoms into Pt-adatoms. The latter not only diffuse faster, and thereby can rapidly find each other and nucleate into islands, but also have a much lower equilibrium concentration. As then the actual Pt-adatom concentration is much higher than their equilibrium concentration, the formation of adatom islands is favored.

Moreover, we show with EC-STM that these adatom islands are dendritic, and not hexagonal, as suggested in an earlier publication [1]. The origin of the dendritic shape resides in a growth instability that is caused by the Kink Ehrlich-Schwoebel Barrier, which hinders

the diffusion of step-adatoms around kink sites that are present at island edges. As dendritic islands are less compact than hexagonal islands, they also exhibit a larger ratio of step sites to terrace sites. This has consequences for the catalyst reactivity as well as for its degradation.

In Chapter 3 we study the (in)stability of flame-annealed Pt(111)-vicinal surfaces, which are widely used in fundamental electrochemistry to investigate the reactivity at platinum step sites. Our statistical analysis on the step height and the terrace width concluded that, while Pt(554) presents a regular array of single steps that are separated by the nominal terrace width, around 51% and 14% of the steps on Pt(553), a surface with higher step density, are bunched into pairs and triplets, respectively. Moreover we show, based on surface science formalism, that the step bunching instability has its origin on the highly-repulsive interaction between closely-spaced steps, which can be lowered by forming step bunches with larger separation. This occurs during the flame-annealing and cooling down of the surface, when the sample is hot and thus the surface mobility is enhanced.

We end this chapter by showing how Pt(111)-vicinal surfaces with bunched steps present an extra peak in the Hydrogen desorption fingerprint, as well as an anomalous, non-linear trend of their potential of zero total charge (E_{pztc}) and Oxygen Reduction Reaction (ORR) activity with their step density. However, we assert that step bunching also has a significant effect on other structure-sensitive electrochemical reactions that are most active at step sites, such as the Hydrogen Oxidation Reaction, the CO Oxidation, and the Nitrate Reduction. Consequently, our findings hold significant implications on the current understanding of platinum electrochemistry at step sites.

With our new insights on the step structure of Pt(111)-vicinal surfaces, in Chapter 4 we move on to quantify the adsorption of hydrogen and oxygen at step sites. Our results show that the voltammetric peak associated to hydrogen desorption from the steps involves more than one electron per unit step length, and thus more than the simple desorption of one hydrogen atom per step site. This could point out towards an exchange mechanism between hydrogen and hydroxide, as stated in recent literature [2, 3]. On the other hand, at high potentials the adsorption of oxygen leads to the formation of PtO_2 along the steps. Additionally, we identify the oxygen adsorption sites at the step edge and we relate them to the corresponding peaks in the Cyclic Voltammogram (CV). Finally, we link this chapter to the previous one by quantitatively demonstrating that step bunching results in a decrease of the hydrogen and oxygen adsorption.

References

[1] L. Jacobse, Y. F. Huang, M. T. M. Koper, and M. J. Rost, *Nat. Mater.*, **17**, 277 (2018).

[2] I. T. McCrum, X. Chen, K. A. Schwarz, M. J. Janik, and M. T. M. Koper, *J. Phys. Chem. C*, **122**, 16756 (2018).

[3] R. Rizo, J. Fernández-Vidal, L. J. Hardwick, G. A. Attard, F. J. Vidal-Iglesias, V. Climent, E. Herrero, and J. M. Feliu, *Nat. Commun.*, **13**, 2550 (2022).

Samenvatting

De transitie van fossiele brandstoffen naar duurzame energie vereist efficiënte methoden om opgewekte energie op te slaan en de beschikbaarheid van energie te verzekeren gedurende een periode van lage productie. De meest efficiënte manier om dit te doen is door duurzame elektriciteit om te zetten in chemische energie. Dit kan worden bereikt met behulp van elektrochemische apparaten zoals batterijen, elektrolysers en brandstofcellen. Optimale elektrochemische materialen zijn de sleutel voor het ontwikkelen van deze technologieën, omdat ze de efficiëntie van de omzetting verbeteren met minimale energieverliezen. Echter, de beste katalysatoren van brandstofcellen zijn gebaseerd op platina; een schaars en duur materiaal. Bovendien degraderen platina katalysatoren bij lang gebruik, wat leidt tot vermindering van hun activiteit en de noodzaak tot vervanging van de brandstofcel. Daarom is het cruciaal om niet alleen die katalysator samenstelling en geometrie te identificeren die voldoet aan de katalytische vereisten, maar ook die stabiliteit in acht te nemen voor verlengde levensduur van het apparaat. In dit proefschrift heb ik een Electrochemical Scanning Tunneling Microscope (EC-STM) gebruikt om de (in)stabiliteit van platina elektrode oppervlakken te bestuderen en de structuur-activiteit relatie op atomaire schaal vast te stellen.

In Hoofdstuk 2 heb ik Density Functional Theory (DFT) en EC-STM gebruikt om de bekende kennis op het gebied van nucleatie en groei van adatoom eilanden op Pt(111) tijdens achtereenvolgende oxidatie-reductie cycli te bestuderen; een proces dat de echte werking van waterstofbrandstofcellen nabootst en dat is gelinkt aan de katalysator degradatie. De resultaten laten oppervlakte oxidatie zien tijdens en de formatie van PtO_2-adatomen. Echter, hun daadwerkelijke concentratie op het oppervlak is vele malen lager dan hun evenwicht concentratie, reden waarom nucleatie tot adatom eilanden niet gunstig is. Bovendien laat ik zien dat de mobiliteit van PtO_2-adatomen zeer beperkt is bij hoge elektrode potentialen, niet alleen door hun inherent trage diffusie, maar ook omdat deze adatomen opgesloten zitten tussen oxide rijen die boven het oppervlakte uitsteken.

Gedurende de kathodische scan wordt de reductie van het oppervlakte oxide gevolgd door de reductie van de PtO_2-adatomen naar Pt-adatomen. Deze laatste diffunderen niet alleen sneller, en kunnen elkaar daarbij ontmoeten en ontkiemen tot eilanden, maar ze hebben ook nog een veel lagere evenwichtsconcentratie. Omdat op dit moment de feitelijke Pt-adatomen concentratie veel hoger is dan hun evenwichtsconcentratie, heeft de

vorming van adatoom eilanden de voorkeur. Bovendien laat ik met EC-STM zien, dat deze adatoom eilanden dendritisch zijn, en niet hexagonaal zoals gesuggereerd in een eerdere publicatie. De oorsprong van de dendritische vorm ligt in een groei instabiliteit die veroorzaakt wordt door de Kink-Ehrlich-Schwoebel Barrière, welke de diffusie verhindert van stap-adatomen om de kinks die aanwezig zijn op de eiland randen. Omdat dendritische eilanden minder compact zijn dan hexagonale eilanden, hebben ze een groter aantal terras sites. Dit heeft zowel consequenties voor de katalytische activiteit als voor de degradatie.

In Hoofdstuk 3 bestudeer ik de (in)stabiliteit van met een vlam gegloeide Pt(111)-vicinale oppervlakken, welke veelvuldig worden gebruikt in fundamentele elektrochemie studies voor het onderzoeken van de reactiviteit van platina stap sites. De statistische analyse van de stap hoogte en de terras lengte laat zien dat, terwijl Pt(554) de regelmatige rangschikking van enkele stappen gescheiden door terrassen met nominale lengte vertoont, ongeveer 51% en 14% van de stappen op Pt(553), een oppervlak met hogere stap dichtheid, gebundeld zijn in paren of tripletten. Bovendien laat ik zien dat de stap bundeling instabiliteit zijn oorsprong heeft in de repulsieve interactie tussen dichtgepakte stappen, welke kan worden verlaagd door de vorming van bundelingen en terrassen met grotere afstanden. Dit vindt plaats gedurende het vlam gloeien en koelen van het oppervlak, wanneer het oppervlak heet is en de oppervlakte mobiliteit nog hoog.

Ik eindig dit hoofdstuk door te laten zien hoe Pt(111)-vicinale oppervlakken met gebundelde stappen leiden tot een extra piek in de waterstof desorptie vingerafdruk, en in een afwijkende, niet-lineaire trend van de Potential of Zero Total Charge en de Zuurstof Reductie Reactie (ORR) activiteit met stapdichtheid. Verder beargumenteer ik ook, dat stap bundeling significante effecten heeft op andere structuur-gevoelige elektrochemische reacties die het meest actief zijn op de stap sites, zoals de Waterstof Oxidatie Reactie, de CO oxidatie en de Stikstof Reductie. Deze bevindingen hebben significante implicaties in het huidige begrip van platina elektrochemie aan stap sites.

Met deze nieuwe inzichten omtrent de stap structuur van Pt(111)-vicinale oppervlakken kwantificeer ik in Hoofdstuk 4 de adsorptie van waterstof en zuurstof op de stap sites. Deze resultaten laten zien dat de voltammetrische piek, die geassocieerd wordt met de waterstof desorptie van de stappen, meer behelst dan een elektron per stap eenheidslengte, en dus complexer moet zijn dan de simpele desorptie van een waterstofatoom per stap site. Dit kan wijzen op een uitwisselingsmechanisme tussen waterstof en hydroxide, zoals eerder voorgesteld in de literatuur. Bij hoge potentialen leidt de adsorptie van zuurstof tot de vorming van PtO_2 langs de stappen. Daarnaast identificeer ik de zuurstof adsorptie plekken aan de stapranden en relateer ik deze tot de corresponderende pieken in de Cyclische Voltammogram (CV). Tot slot koppel ik dit hoofdstuk aan het voorgaande hoofdstuk via een kwantitatieve demonstratie, dat stap bundeling resulteert in een vermindering van de waterstof en zuurstof adsorptie.

Outlook

The work presented in this thesis addresses the (in)stability of platinum electrode surfaces at the atomic-scale with the help of EC-STM. Our findings not only contribute to improve the current understanding on the degradation of platinum catalysts, but also challenge the established assumption that stepped surfaces are composed by an array of homogeneously distributed steps. Moreover, in Chapters 3 and 4 we show how the step bunching instability has significant effects on the electrochemistry of platinum stepped surfaces, and can explain the non-linear step density-dependent trends reported in the literature. The next sections present suggestions for future studies that I collected during my PhD time, as well as measurements and insights that I performed, but could not finish within the framework of this thesis. The latter will be part of future work and publications.

O.1 Platinum Oxide Structure

In Chapter 2 we discuss that platinum surface degradation is closely related to its oxidation, which results firstly in the reversible place exchange (PE_{rev}) between platinum surface atoms and the oxygen atoms adsorbed, and ultimately in the formation of adatom and vacancy islands. Therefore, identifying the surface oxide structure is key to gain insight on the degradation mechanism, which would allow for the design of more stable catalysts.

In Chapter 4 we show that the oxidation process results in PtO_2 along the steps. However, the oxide structure on terraces remains under discussion. Surface X-Ray Diffraction (SXRD) measurements in electrochemical environment suggest that the PE_{rev} takes place randomly, similar to a 2D adatom gas, although they can not discard the formation of semi-ordered structures such as one-dimensional rows [1, 2]. These oxide rows have been observed on Pt(111) with STM at 1 bar of oxygen pressure and high temperature [3]. Moreover, their stability at high electrochemical potential is supported by DFT [4].

EC-STM measurements on Pt(111) at high oxidative potentials could be useful to capture, *operando*, the real surface oxide structure. In addition, it should be possible to follow the terrace oxidation with EC-STM while the electrode potential is increased, and then decreased, similar to the measurements performed by Wakisaka et al. [5]. A more detailed study, zooming-in on the platinum terrace, with a very sharp STM-tip, and at the optimal

tunneling conditions (e.g. high tunneling current), could provide an answer on weather the oxide rows exist, or contrary the terrace oxidation proceeds randomly.

O.2   Nucleation and Growth of Vacancy Islands

The roughening of a Pt(111) surface upon oxidation-reduction cycling was followed in detail with EC-STM [6–8]. However, while it was possible to fully characterize the adatom islands, the individual vacancies as well as small vacancy islands formed during the first cycles were most of the times not visible. The reason for this is tip convolution (i.e. any STM image results from the convolution of the tip shape and the surface morphology), which leads to the vacancies appearing smaller (both narrower and less deep) than they actually are in reality. Nevertheless, these small vacancies are known to be very active towards the ORR [9], and therefore it is important to gain insight on their nucleation, growth, and coalescence. This could be achieved using SXRD [10].

O.3   Stability of Platinum Stepped Surfaces during Oxidation-Reduction Cycling

Although there is extensive research on the roughening of Pt(111) upon oxidation-reduction cycling, there is not yet any study addressing the same cycles also on stepped platinum surfaces. However, we know that steps have a crucial role on the roughening process, as the late growth of 3D islands is dominated by the step oxidation, which results in the formation of adatoms from step atoms. In an ongoing project, we use EC-STM to study the stability of Pt(111)-vicinal surfaces upon oxidation-reduction cycling.

Figure O.1(a-e) shows 80 oxidation-reduction cycles (ORCs) on Pt(111) as well as on four Pt(111)-vicinal surfaces: Pt(15 15 14), Pt(554), Pt(553), and Pt(533), with nominal terrace widths of 30, 10, 5, and 4 atomic rows, respectively. We do know in the meantime (Chapter 3) that Pt(553) undergoes step bunching, and hence exhibits mostly terraces with double of the nominal width. Pt(15 15 14), Pt(554), and Pt(553) (as-prepared) surfaces present steps with (111) microfacets. This is evident from their initial Cyclic Voltammograms (CVs), which show a (111) step-related peak at around 0.128 V, within the Hydrogen underpotential deposition (H_{upd}) region. Contrary, the nominal structure of Pt(533) presents steps with (100) microfacets, which contribute to the (100) step-related peak at around 0.280 V. However, the first CV on Pt(533) also shows a feature at around 0.128 V, which indicates that the (100) steps on this surface are partially faceted, resulting in regions with (111) steps.

On Pt(15 15 14), oxidation-reduction cycling leads to significant changes in the electrochemical fingerprint, similarly to Pt(111). The (111) step peak in the H_{upd} region (H1 peak in Fig. O.1b) grows in intensity and becomes broader, indicating an increase of (111) step length. Moreover, three more peaks (H2-H4) appear, which were previously attributed to hydrogen desorption from single vacancies, narrow facets with (100) steps, and narrow facets with (111) steps [11]. In addition, peaks appear between 0.85 V and 1.05 V that are attributed to the oxidation of platinum step sites, as discussed in Chapter 4. Finally, the

feature related to the PE_{rev} at around 1.1 V diminishes in height, indicating a decrease of terrace sites at the expense of the newly formed step sites.

On Pt(554), the CV changes much less upon oxidation-reduction cycling. The H1 peak does not increase in height, it only becomes broader. Moreover, the H2 and H3 peaks are barely visible, while the H4 peak does not appear at all. This suggests that the Pt(554) surface roughens less (or slower) than Pt(111) and Pt(15 15 14), which have wider terraces. This effect is even more notable on Pt(553), which CV barely changes during cycling. Therefore, from the ORCs one would expect that Pt(553) is stable and does not roughen at all.

Pt(533) is a special case, as it initially presents (100) steps. During oxidation-reduction cycling, (111) steps form at the expense of the (100) steps, which leads to a decrease of the H2 peak and an increase of the H1 peak [6, 12]. Apart from this, the rest of the CV barely changes during cycling, which could indicate that the terraces do not roughen.

Following the work by Jacobse et al. [6], we then quantified for all surfaces the total H_{upd} charge, $Q_{H_{upd}}$, at each ORC, see Fig. O.1f. Focusing first on Pt(111), in black, the rise of $Q_{H_{upd}}$ is indicative for an increase of the surface roughness. A change on the slope of the $Q_{H_{upd}}$ curve points out towards a change of the growth speed, and thus of the roughening mechanism. Therefore, the roughening process was divided in two different regimes: the initial nucleation and early lateral (2D) growth of islands and, after around 20 cycles, the late growth that occurs predominantly in height (3D). The plateau observed in between ORCs 8-14 is related to the transition from the 2D growth into the 3D growth.

Moving now to the Pt(111)-vicinal surfaces, Pt(15 15 14) exhibits a lower slope of the $Q_{H_{upd}}$ curve than Pt(111), both in the 2D and the 3D regime, which indicates that the roughening on Pt(15 15 14) is slower. The growth speed decreases even more for Pt(554), which has a smaller terrace width, of 10 atomic rows. For Pt(553), with a nominal terrace width of 5 atomic rows (although we know from Chapter 4 that more than half of the terraces are double this value), $Q_{H_{upd}}$ increases only during the 2D regime, and not during the 3D regime. This suggests that, if islands are formed on this surface, they only grow laterally and not in height. Moreover, it shows that the narrower the terrace width, the slower the growth speed. Finally, although the ORCs of Pt(533) (with (100) steps) show remarkable changes due to the faceting of (100) steps into (111) steps, $Q_{H_{upd}}$ remains almost constant, suggesting that this surface does not roughen at all.

Figure O.2 shows EC-STM images obtained on Pt(554), Pt(553), and Pt(533) before any ORC (a-c), after 20 ORCs (d-f), and after 80 ORCs (g-i). Starting with Pt(554), the initial parallel steps on the pristine surface meander upon oxidation-reduction cycling, becoming highly rough already on cycle 20. Moreover, islands form due to the *pinching off* of the step meanders, which is driven by the attractive step-step interaction of opposite type of steps [13–15]. These islands acquire a height spanning multiple atomic layers during cycling, see Fig. O.2g. Consequently, the total step length increases, which explains the increase of $Q_{H_{upd}}$ upon cycling shown in blue in Fig. O.1f.

As elaborated in Chapter 3, more than half of the steps on the pristine Pt(553) surface, shown in Fig. O.2b, are bunched. Oxidation-reduction cycling results once again in step meandering and the subsequent breaking down of the step meanders into small islands,

as evident from Fig. O.2e. In this case, however, the roughening of this surface is less pronounced than on Pt(554) and the islands do not seem to increase in height even after 80 ORCs. This would explain that $Q_{H_{upd}}$ only rises during the 2D regime, and not in the 3D regime.

Finally, Pt(533), which should consist of (100) steps and terraces with a width of 4 atomic rows, does not present the nominal surface structure (see Fig. O.2c). Instead, this surface exhibits step meanders, which must form not only (100) but also (111) microfacets, explaining the (111) step peak in the initial CV shown in Fig. O.1e. Moreover, the terraces are visibly wider than 4 atomic rows, suggesting that the steps are bunched. Mild oxidation-reduction cycling (20 ORCs) results into the breaking down of the steps into zig-zag structures with two different orientations (Fig. O.2f). This process results in a decrease of the (100) step length and an increase of the (111) step length, which matches the observations from the ORCs in Fig. O.1e. After 80 ORCs, the initial direction of the steps is completely lost, see Fig. O.2i. Instead, the surface exhibits lines orthogonal to the initial step direction shown in Fig. O.2c. This is surprising, given the fact that the terrace atoms on Pt(533), like on any other (111)-vicinal surface, present an hexagonal arrangement with a 60 degree symmetry. Moreover, such morphological surface changes are not reflected on the $Q_{H_{upd}}$ curve shown in purple in Fig. O.1f, which remains almost constant. This suggests that the adsorption/desorption of hydrogen per total step length (i.e. sum of (100) and (111) step length) does not change during cycling, although this seems very unlikely. In order to obtain more insight, in the near future we will perform a detailed analysis on the step structure as well as on the surface roughness evolution.
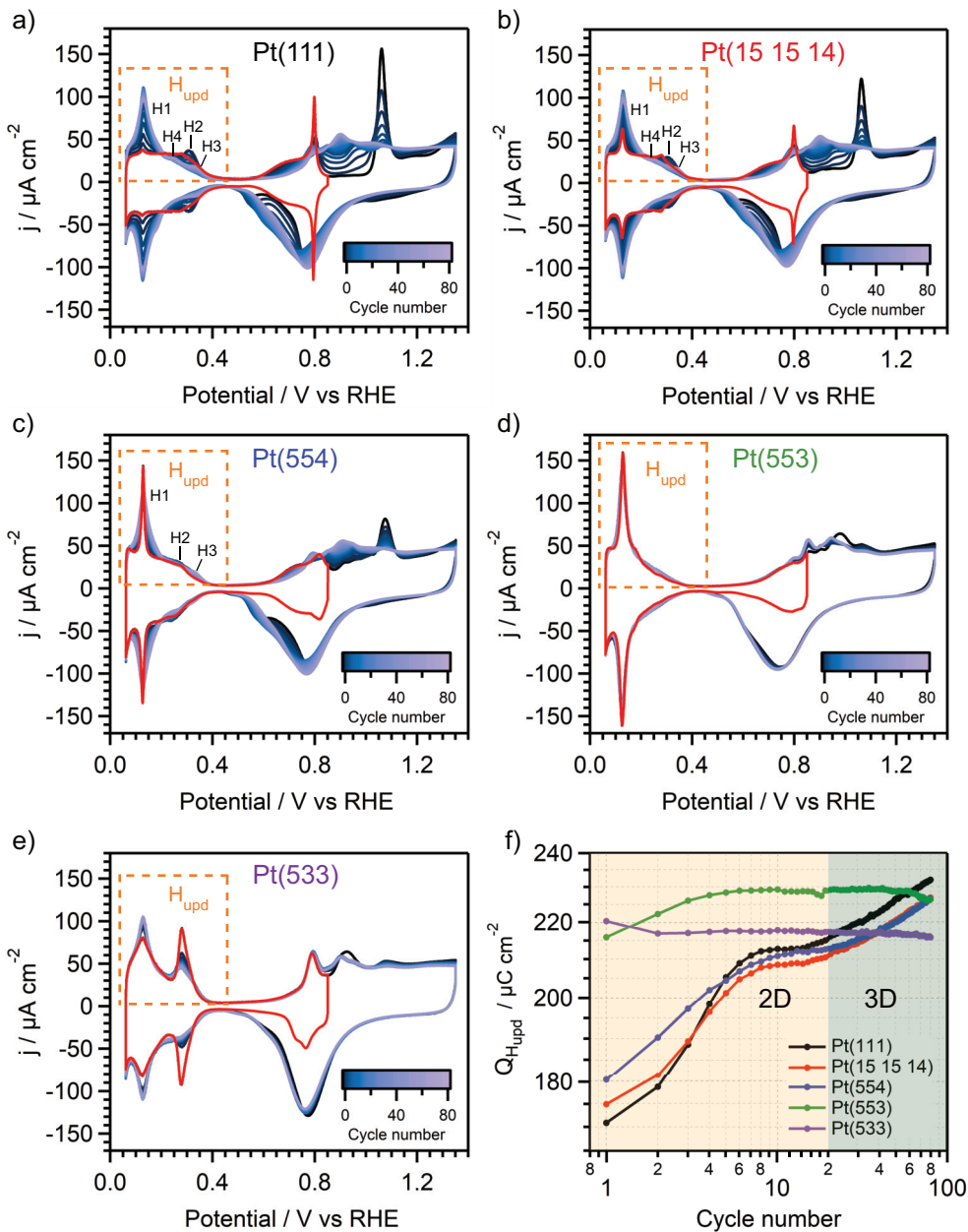
Figure O.4: Oxidation-Reduction Cycles on Pt(111) and its Vicinal Surfaces. (a-e) Oxidation-reduction cycles on Pt(111), Pt(15 15 14), Pt(554), Pt(553), and Pt(533). The H_{upd} region is highlighted with an orange rectangle, while the step-related peaks within are indicated as H1-H4. **(f)** The H_{upd} charge versus the cycle number (for each of the surfaces studied) is a good electrochemical measure for the roughness [6]. The two roughening regimes, in 2D and in 3D, are indicated in yellow and green, respectively.
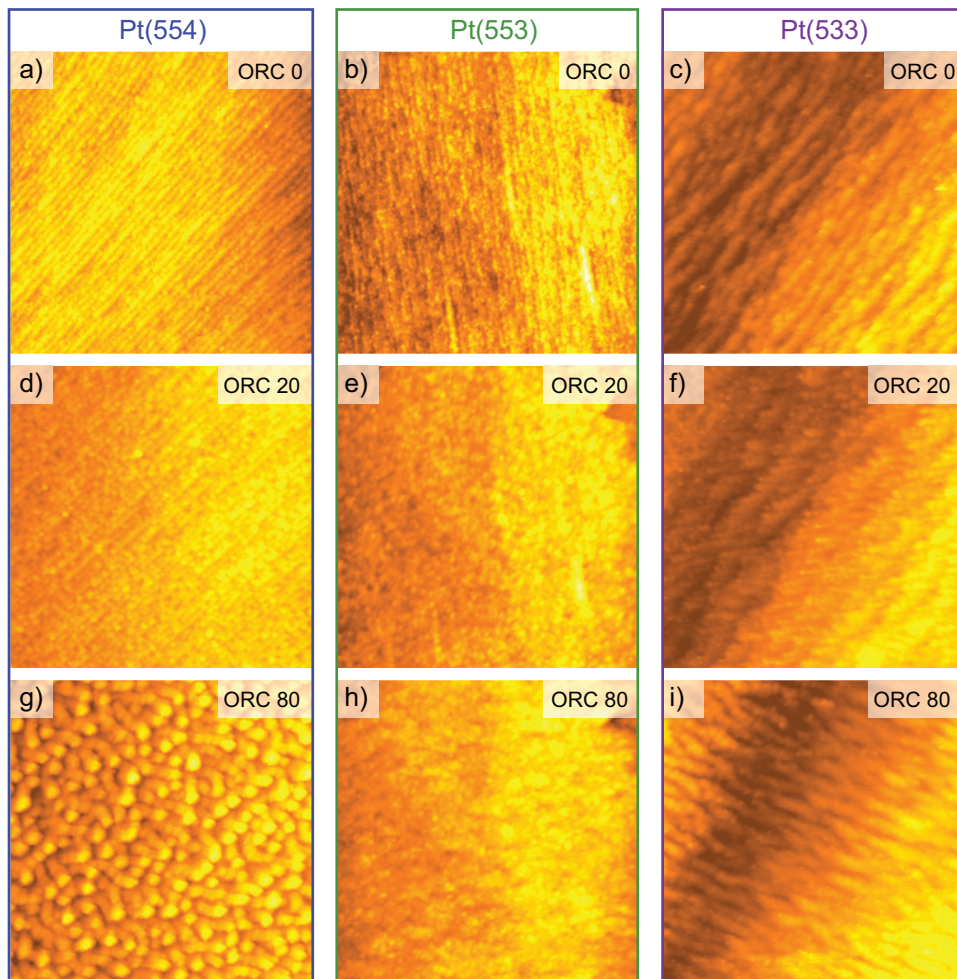
Figure O.5: EC-STM Images of Pt(111)-Vicinal Surfaces after Oxidation-Reduction Cycles. (a), (b), and (c) show the as-prepared Pt(554), Pt(553), and Pt(533) electrodes, respectively. (d), (e), and (f) show the same samples on the same place after 20 ORCs. Finally, (d), (e), and (f) show again the same place on the surfaces after 80 ORCs. All images are 100 x 100 nm^2, and were recorded in 0.1 M HClO$_4$ at sample and tip potentials of 0.1 V and 0.15 V, respectively.

References

[1] L. Jacobse, V. Vonk, I. T. McCrum, C. Seitz, M. T. M. Koper, M. J. Rost, and A. Stierle, *Electrochim. Acta*, **407**, 139881 (2022).

[2] J. Drnec, M. Ruge, F. Reikowski, B. Rahn, F. Carlà, R. Felici, J. Stettner, O. M. Magnussen, and D. A. Harrington, *Electrochim. Acta*, **224**, 220 (2017).

[3] M. A. van Spronsen, J. W. M. Frenken, and I. M. N. Groot, *Nat. Commun.*, **8**, 429 (2017).

[4] S. Hanselman, I. T. McCrum, M. J. Rost, and M. T. M. Koper, *Phys. Chem. Chem. Phys.*, **22**, 10634 (2020).

[5] M. Wakisaka, S. Asizawa, H. Uchida, and M. Watanabe, *Phys. Chem. Chem. Phys.*, **12**, 4184 (2010).

[6] L. Jacobse, Y. F. Huang, M. T. M. Koper, and M. J. Rost, *Nat. Mater.*, **17**, 277 (2018).

[7] M. J. Rost, L. Jacobse, and M. T. M. Koper, *Nat. Commun.*, **10**, 5233 (2019).

[8] F. Valls Mascaró, I. T. McCrum, M. T. M. Koper, and M. J. Rost, *J. Electrochem. Soc.*, **169**, 112506 (2022).

[9] F. Calle-Vallejo, J. Tymoczko, V. Colic, Q. Huy Vu, M. D. Pohl, K. Morgenstern, D. Loffreda, P. Sautet, W. Schuhmann, and A. S. Bandarenka, *Science*, **350**, 185 (2015).

[10] K. Iizuka, T. Kumeda, K. Suzuki, H. Tajiri, O. Sakata, N. Hoshi, and M. Nakamura, *Commun. Chem.*, **5**, 126 (2022).

[11] L. Jacobse, M. J. Rost, and M. T. M. Koper, *ACS Cent. Sci.*, **5**, 1920 (2019).

[12] A. Björling and J. M. Feliu, *J. Electroanal. Chem.*, **662**, 17 (2011).

[13] T. Michely and J. Krug, *Islands, Mounds and Atoms*, Springer, Amsterdam (2004).

[14] M. Rost, P. Smilauer, and J. Krug, *Surf. Sci.*, **369**, 393 (1996).

[15] J. Kallunki and J. Krug, *Europhys. Lett.*, **66**, 749 (2004).

List of Publications

Chapter 2

F. Valls Mascaró, I. McCrum, M. T. M. Koper, and M. J. Rost, J. Electrochem. Soc., **169**, 112506 (2022), *Nucleation and Growth of Dendritic Islands during Platinum Oxidation-Reduction Cycling.*

Chapter 3

F. Valls Mascaró, M. T. M. Koper, and M. J. Rost, *Step Bunching Instability and its Effects in Electrochemistry: Pt(111) and its Vicinal Surfaces.* Submitted.

Chapter 4

F. Valls Mascaró, M. T. M. Koper, and M. J. Rost, *Quantitative Study of Electrochemical Adsorption and Oxidation on Pt(111) and its Vicinal Surfaces.* Submitted.

Outlook

F. Valls Mascaró, M. T. M. Koper, and M. J. Rost, *Roughening of Pt(111) Vicinal Surfaces during Oxidation-Reduction Cycling.* In preparation.

Other publications

N. Fröhlich, J. Fernández-Vidal, F. Valls Mascaró, A. J. Shih, M. Luo, and M. T. M. Koper, Electrochim. Acta, **466**, 143035 (2023), *Effect of Trace Impurities in Perchloric Acid on Blank Voltammetry of Pt(111).*

J. B. V. Mygind, F. Valls Mascaró, and M. J. Rost, *Arrhenius follows Frumkin to describe Atomic Diffusion Involved Peaks in Cyclic Voltammograms: the Reversible Place-Exchange Peak during the Electrochemical Oxidation on Pt(111).* To be submitted.

Curriculum Vitae

Francesc Valls Mascaó was born on February 20th in Pollensa, Mallorca, Spain. There, he attended high school between 2007 and 2012, where he soon developed an interest for natural sciences. During this period, he also performed different extra-curricular activities, including playing basketball and performing as a percussionist in a band.

After graduating high school with "cum laude", Francesc left the island of Mallorca and moved to Barcelona to start a bachelor in Chemistry at the University of Barcelona. However, this was a difficult choice, as he also had a high interest in physics and mathematics. During the summer holidays of 2016, he worked as a research assistant in the Soft Matter group from Prof. Dr. Francesc Sagués, where he had the first contact with scientific research whilst experimenting with microfluidics and colloidal systems. This led to developing his passion for physical chemistry, and hence the next academic year he undertook Computational Chemistry, Surface Science, and Electrochemistry as optional courses. Francesc found the later subject especially compelling, and upon receiving advise from Dr. Elisa Vallés, he decided to leave Spain with the ultimate goal of pursuing a scientific career.

Consequently, in 2017 Francesc joined a Master's program in Electrochemistry at the University of Southampton (United Kingdom), which consisted of 9 months of intensive courses in electrochemistry, surface science, and engineering followed by a 3-month final project in a research laboratory of choice. Given his interest on fundamental studies for fuel cell technology, he decided to join the electroanalytical chemistry group of Dr. Guy Denuault, where he studied the Oxygen Reduction Reaction on Pt microelectrodes at the millisecond timescale under the daily supervision of Dr. Oliver Rodriguez. Upon completing this project in September 2018, he graduated with "Cum Laude" from the University of Southampton.

Just a few weeks later, Francesc moved to The Netherlands to pursue a PhD in electrochemistry and surface science under the supervision of Prof. Dr. Marc Koper and Dr. Marcel Rost at Leiden University. The project focused on studying the (in)stability of single-crystalline platinum electrodes under electrochemical conditions as well as the impact of surface structural changes on electrocatalysis. For this he used a home-build Electrochemical Scanning Tunneling Microscope, which allowed for the electrode surface characterization at the nanoscale. The interdisciplinary nature of the project provided him the opportunity to not only expand his knowledge in electrochemistry but also to develop a strong

background in nucleation and growth theory, fundamental thermodynamics, and dynamics of surface processes. He also learned Python programming, which is now part of his skillset to analyze both electrochemical data and topographic STM images.

In addition to this, Francesc had a side project in which he collaborated with other members from the Catalysis and Surface Chemistry (CASC) group to assess the effect of nitrate and sulphate trace impurities in perchloric acid on blank voltammetry of Pt(111). Moreover, he supervised a Master student in his final (one-year-long) project and two bachelor students for short term internships, on top of teaching practical courses of basic chemistry to first year students. Finally, he gave oral presentations on his research at numerous (inter)national conferences, including two invited talks (2021 and 2022) at the Annual meetings from the Dutch Association for Crystal Growth, an invited talk at the Annual meeting from The Electrochemical Society (2022), two contributed talks (2022 and 2023) at the Spring meeting from the German Physical Society, and one at the Annual meeting from the International Society of Electrochemistry (2023).

Acknowledgements

my doctorate journey, and since then, we have grown together. Your infectious cheerfulness (especially after coffee) enlightened my days. You supported me at all times, particularly during the toughest moments, and inspired me to become a better person day after day. Not to forget your invaluable help in proofreading this thesis as well as listening to my practice talks on "platinum and steps". Without you by my side, I would not have made it this far with some sanity and health still intact. Thank you for everything.

Last but not least, I am profoundly grateful for the unconditional support of my family. To my parents, Tomeu and Joana, who raised two very ambitious sons soon to graduate as doctorates - these accomplishments speak to the values that you imprinted in us. To my "little" brother Esteve, thank you for your help in programming and for our countless discussions related to our PhD journeys. To my grandpa, whose vitality and joy at 90 years of age is truly a source of inspiration. And to my cousins, aunts, uncles, and friends back home, thank you for all the enjoyable moments that allowed me to completely disconnect from work while in Mallorca.